UNIVERSIDADE ESTADUAL DE CAMPINAS
FACULDADE DE ENGENHARIA ELÉTRICA E DE COMPUTAÇÃO

Ruth Esther Rubio Noriega

Aspects of Interconnectivity in Polymer Modulators

Aspectos de Interconectividade dos Moduladores de Polímero

Campinas
2017

Ruth Esther Rubio Noriega

Aspects of Interconnectivity in Polymer Modulators

Aspectos de Interconectividade dos Moduladores de Polímero

Tese apresentada à Faculdade de Engenharia Elétrica e de Computação da Universidade Estadual de Campinas como parte dos requisitos exigidos para a obtenção do título de Doutora em Engenharia Elétrica, na Àrea de Telecomunicações e Telemática.

Thesis presented to the Electric and Computing Engineering of the University of Campinas in partial fulfillment of the requirements for the degree of Doctor, in the area of Telecommunications and Telematic.

Supervisor/Orientador: Hugo Enrique Hernández Figueroa

Este exemplar corresponde à versão final da tese defendida pelo aluno Ruth Esther Rubio Noriega, e orientada pelo Prof. Dr. Hugo Enrique Hernández Figueroa.

Campinas
2017

Agência(s) de fomento e nº(s) de processo(s): CAPES, 07/2014-36
ORCID: http://orcid.org/http://orcid.org/ht

Ficha catalográfica
Universidade Estadual de Campinas
Biblioteca da Área de Engenharia e Arquitetura
Luciana Pietrosanto Milla - CRB 8/8129

R825a

Rubio Noriega, Ruth Esther, 1987-
Aspects of interconnectivity in polymer modulators / Ruth Esther Rubio Noriega. – Campinas, SP : [s.n.], 2017.

Orientador: Hugo Enrique Hernández-Figueroa.
Tese (doutorado) – Universidade Estadual de Campinas, Faculdade de Engenharia Elétrica e de Computação.

1. Guias de onda óticos. 2. Moduladores de luz. 3. Linhas de transmissão de microondas. I. Hernández-Figueroa, Hugo Enrique,1959-. II. Universidade Estadual de Campinas. Faculdade de Engenharia Elétrica e de Computação. III. Título.

Informações para Biblioteca Digital

Título em outro idioma: Aspectos de interconectividade dos moduladores de polímero
Palavras-chave em inglês:
Optical waveguides
Light modulators
Microwave transmission lines
Área de concentração: Telecomunicações e Telemática
Titulação: Doutora em Engenharia Elétrica
Banca examinadora:
Hugo Enrique Hernández-Figueroa [Orientador]
Giovanni Beninca de Farias
Julio Cesar Rodrigues Fernandes de Oliveira
Lucas Heitzmann Gabrielli
Luciano Prado de Oliveira
Data de defesa: 05-06-2017
Programa de Pós-Graduação: Engenharia Elétrica

COMISSÃO JULGADORA - TESE DE DOUTORADO

Candidato: Ruth Esther Rubio Noriega RA: 100316
Data da Defesa: 05 de Junho de 2017
Título da Tese: Aspects of Interconnectivity in Polymer Modulators (Aspectos de Interconectividade dos moduladores de polímero)

Prof. Dr. Hugo Enrique Hernández Figueroa
Dr. Giovanni Beninca de Farias
Dr. Julio Cesar Rodrigues Fernandes de Oliveira
Prof. Dr. Lucas Heitzmann Gabrielli
Prof. Dr. Luciano Prado de Oliveira

A ata de defesa, com as respectivas assinaturas dos membros da Comissão Julgadora, encontra-se no processo de vida acadêmica do aluno.

To my parents Ruth & Obidio - They had faith in me even when times were difficult.

Acknowledgment

To my Lord and savior Jesus Christ.

To my best friend, my parter and love, Jorge González.

I am grateful to my parents Obidio and Ruth for their never-ending emotional support and my siblings Rosa Linda and Junior for always believing in me.

A very special gratitude to my professors: Hugo Hernández, Luciano Prado and Lucas Gabrielli.

I am also grateful to my dearest friends: María, Robert, Roger, Chrisnael, Suéllen, Banny for their company throughout these years.

To everyone in the Applied and Computational Electromagnetics Group (GEMAC)... it was great sharing laboratory with you.

To the CAPES foundation for their financial support.

Abstract

Electrical and optical interconnects are of great interest for photonic integrated circuits with hybrid platforms. Low loss and wide band are essential for the development of new technologies in this area. In this thesis, we present the following original contributions: a methodology for modeling electrical ceramic interconnects inside an electrooptic polymer packaging, and a compact low-loss optical interconnect for the silicon-on-insulator platform to the thin-film polymer on silicon platform.

Key-words: Waveguides, optical interconnects, photonic system packaging, photonic integrated circuit, integrated photonics.

Resumo

As interconexões ópticas e elétricas são de grande interese na area de encapsulamento de circuitos integrados híbridos fotônicos. Baixas perdas e banda larga são necessárias para o desenvolvimento de novas tecnologías na área. Nesta tese apresentan-se as seguintes contribuições originais: uma metodologia do modelamento de interconexões elétricas em encapsulamento de moduladores de polímero eletro-óptico, um dispositivo óptico compacto de banda larga para interconectar a plataforma de silício sobre isolante com a plataforma de filmes finos de polímero sobre silício.

Palavras-chave: Guias de onda, interconectividade óptica, empacotamento de sistemas fotônicos, circuitos integrados fotônicos, fotônica integrada.

List of Figures

1.1 Illustrative representation of a transmitter optical sub-assembly showing light source, passive silicon-on-insulator optical circuitry, the electrooptic polymer chip. High speed radio frequency interconnects are also represented as Feeding Ceramic and Termination Ceramic. 21
1.2 Electrical Interconnects in a transmitter optical subassembly packaging. . . 22
1.3 Bias circuit of an electrooptic polymer Mach-Zhender modulator. 22
1.4 Optical interconnects in a transmitter optical subassembly packaging. . . . 22

2.1 General block diagram of a communications system. 24
2.2 Polymer modulator schematic. 27
2.3 Longitudinal cut representation of a single high speed interconnection electric path on a transmitter optical sub-assembly. The printed circuit board meets the function of a TOSA carrier. Chip indicates an arbitrary placement of the the EO polymer or TFPS chip. 28
2.4 Electric signal path of the whole system. Including TOSA carrier, TOSA and Modulator electrode. 28
2.5 Optical signal path on a transmitter optical subassmbly. Red arrow represents signal path. Optical interconnects between platforms are indicated by dark arrows. 29
2.6 A Mach-Zhender electroooptical modulator showing potentials V_1 and V_2. Blue represents optical path while electric potentials are yellow. 31
2.7 Sinusoidal MZM response indicating V_π. 31
2.8 Push-pull applied voltage configuration versus single drive. 31
2.9 Poling process of the chromophore molecules inside a polymer host. 34
2.10 Anatomy of an EO polymer MZM. 35

3.1 LX8242 DP-QPSK TFPS modulator by Gigoptix/BrPhotonics schematic. Upper gold trace is shown in yellow, while bottom plane metalization is orange. Optical waveguide trench is shown in blue. 37
3.2 Cross section of the active section of the TFPS Mach-Zehnder modulator. . 39
3.3 Modal analysis of the TFPS modulator transversal section. TM mode at $\lambda_0 = 1.55\mu m$ 41
3.4 Modal dispersion of the TFPS waveguide. Inlay figures show electric field distribution and and (Ex, Ey) distribution (gray arrows). 41
3.5 Dispersion of the polymer materials from 0.04 GHz to 65 GHz. 43
3.6 Single MZ device diagram showing light and electric signal paths in a TFPS modulator. 43
3.7 Electric signal path of the whole system. Including TOSA carrier, TOSA and Modulator electrode. 44

3.8 Modal analysis of the Microstrip line in one of the active arms of the TFPS modulator. 44
3.9 Modal analysis results of the polymer microstrip QTEM mode. 45
3.10 S-parameters of the active region on a TFPS modulator. Length varies from $L_{active} = 500\mu$m to $L_{active} = 9$ mm. 46
3.11 Microstrip bending simulation model of the TFPS modulator. Trace width is $12\mu m$. 46
3.12 S-parameters of the bending microstrip in the TFPS modulator technology. 47
3.13 Electrical signal input ports of the TFPS modulator. Each electrode over a Mach-Zehnder modulator arm is fed by a port (1, 2, 3 or 4). Dashed box encloses our simulation domain. Gold layers are shown. 48
3.14 Fabrication layers of the CPW to microstrip converter structure (CPW launch). Velocity matching layer is deposited only on top of the microstrip. 48
3.15 Electrical field distribution and Power flow of the input converter of the LX8242 modulator. 49
3.16 S-parameters of the input CPW to microstrip mode transformer. LX8242 polymer modulator. 49
3.17 Electrooptic response of the 9mm MZ polymer modulator. 51
3.18 Bias circuit (heater) on a MZ polymer modulator. 52
3.19 Simulation environment of the thermo-optical effect. The polymer stack is represented as a thermal unit with the same Thermal coefficient. 53
3.20 Heat distribution of T(surface) and first TM mode's electric field distribution of the non poled polymer waveguide (contour). Axis units are meters. . . . 53
3.21 Heat distribution of T(surface) and first TM mode;s electric field distribution of the opposite MZ arm polymer waveguide (contour). Axis units are meters. 54
3.22 Accumulated phase shift induced by the thermo-optical effect in the polymer modulator chip. $\Delta\phi_c$ corresponds to the set up in Figure 3.20 and $\Delta\phi_i$ to Figure 3.21. $\Delta\phi_h = \Delta\phi_c - \Delta\phi_i$ is the real phase shift between MZ arms. . 55
3.23 Numerical simulation results of the polymer modulator heater to maintain a πphase between MZ arms. 56
3.24 Thermo-optic simulation result of an LX8901 Eo polymer modulator. Phase Shift on each MZ arm ($\Delta\phi_c$ and $\Delta\phi_i$) as a function of the heater temperature. 57
3.25 Electro-optic simulation result. Current sweep applied to the bias heater circuit length cases the electrode temperature to vary when compared with room temperature (ΔT_0). Triangle marker represents the current needed to achieve $\Delta T_0 = 8.51$K. 57
3.26 Heater bias measurement setup. 58
3.27 Optical power measured versus injected current (I_0) to the bias heater circuit of an LX8901 EO polymer modulator. 58

4.1 Schematic of the design process for the RF paths. Input blocks are colored orange, while active process blocks are violet. 61
4.2 Longitudinal cut of the electrical signal path representation of a transmitter optical subassembly package including electrooptic polymer thin-film on silicon (TFPS) chip. Yellow represents metalization. 65
4.3 High speed electric signal path of the whole system specifying the ceramic package line (Z_{con} is impedance due to connectorization, TL_{in} is the transmission line eq. impedance, $Z_{s1,s2}$ is due to bonding losses.) 65

4.4 Single wire bond test. Distance between pads (d) and wire height (h) were sweeped. 67
4.5 Double wire bond on signal pad test. Distance between pads (d) and wire height (h). 67
4.6 Ribbon interconnection pad test. 68
4.7 Comparison between the electric field distribution at 40 GHz at the center ($d/2$) of all bonding test platforms and the coplanar waveguide set of pads mode used. 68
4.8 Female W1 connector schematic as shown in Anritsu catalog. 69
4.9 GPPO connector and differential input TFPS modulator pads Electric field distribution comparison. 69
4.10 Single ended MZ TFPS modulator schematic. Yellow represents the electrical path's trace. Ground metalization is represented in orange. 70
4.11 W1 connector attached to a single-ended MZ TFPS modulator input. . . . 70
4.12 W1 connector/single-ended modulator transmission and reflection parameters. 71
4.13 Ceramic taper for packaging with G3pO connector using LX8901 single-ended TFPS modulator. 72
4.14 S-Parameters of tapered and taper-less G3PO connection to an LX8901 by Gigoptix/BrPhotonics. Dimensions in μm. 73
4.15 Differential feed-though interface with 0.8mm pitch, according to OIF agreement. 73
4.16 Electrical feed pads of an LX8242 DP-QPSK TFPS modulator by Gigoptix/BrPhotonics. Only two sets of electrical pads corresponding to two Mach-Zehnder modulators are shown. Yellow represents top metalization. Bottom lamination is orange. Optical trench is represented in blue. Dimensions in micrometers. 74
4.17 Interconnection ceramic. Top metal is represented in yellow while Alumina 99.6% is pink. Dimensions in micrometers. 74
4.18 Feeding transmission line with feedthrough pins layout and wire bonds towards the modulator pads. S-Parameters of the whole feeding transmission line including losses caused by wire bonding. 75
4.19 Termination Circuit for a TFPS MZ modulator. 76
4.20 LX8242 coplanar waveguide RF output pads. 76
4.21 Common dimensions examples of wide band elements. Dimensions are in millimeters. Tolerances are ranging from ±0.02 to ±0.05 mm. 77
4.22 Termination transmission line with capacitor correction and characteristic impedance matching resistor. 77
4.23 Reflection coefficient of the designed termination transmission line with capacitor correction and matching resistor. 78
4.24 Reflection coefficient of the termination transmission line considering wire bonding. wo/wire bonding describes the behavior of the ceramic transmission line by itself, while w/wire bonding shows the behavior of the TL plus wire bonding set and the modulator's input pads. 78
4.25 TOSA electrical path of the single-ended modulator with W1 connector. . 79
4.26 Measured and simulated results of the TOSA electrical path for LX8901 BrPhotonics modulator with W1 connector. 79
4.27 Single-ended modulator TOSA electrical path with G3PO connector. . . . 80
4.28 G3PO wire soldered to an LX8901 TFPS modulator. 80

4.29 Return loss of the G3PO connector TOSA with mode converter taper when compared to OIF recommendations. . . . 81
4.30 Feed through pins interconnection with LX8242 modulator by BrPhotonics electric path diagram. . . . 81
4.31 Return loss of Fig. 4.30 configuration. . . . 82
4.32 Electrooptic response of the LX8242 chip compared to proposed RF feed plus chip response. . . . 82

5.1 Typical core dimensions of the different technologies on a hybrid Transmitter Optical Subassembly. Not to scale. . . . 84
5.2 Flux blocks diagram showing the design methodology used for our optical interconnect. . . . 85
5.3 Cross section of the active region of the polymer Mach-Zehnder modulator. 88
5.4 Longitudinal cut of the proposed silicon-on-Insulator platform interconnection at the input and output of an EO polymer modulator die. Red arrow indicates path of light. SOI platform, taper transition and polymer-on-silicon platform stages are shown. At the transition, spot size is converted through an adiabatic taper. Geometries are not to scale. . . . 89
5.5 Transition between the EO polymer modulator waveguide and SOI taper. . . 90
5.6 First unperturbed problem: Polymer waveguide with glass cladding. . . . 90
5.7 Second unperturbed problem geometry: Silicon waveguide with polymer cladding. . . . 91
5.8 Silicon waveguide modal analysis as a function of its width (w_{si}) at $\lambda =$ 1550nm. Inset shows a detail of the region of intersection between effective indexes. . . . 92
5.9 Perturbed problem: Silicon and polymer waveguides in close proximity.d_1 is the distance between the bottom metalization and the polymer core. . . 92
5.10 Antisymmetric supermode magnetic field distribution. Quasi-TM mode of SOI and polymer waveguides when brought into close proximity. $\lambda = 1550$ nm and $\Delta n_{eff} \approx 0$. . . . 93
5.11 Hybrid Silicon Taper geometry showing port identification. Port 1 refers to polymer TM mode and Port 2 is silicon core waveguide TM mode. . . . 94
5.12 Normalized Output power as a function of the linear variation of the taper length in micrometers. Presence of 1 μm gold thin film is evaluated by varying polymer waveguide height (h_c) and distance to the core d_1. . . . 95
5.13 Normalized output power as a function of the linear variation of the taper length in micrometers. Silicon taper offset along the x axis from 1 μm to 1.8 μm is considered. TM mode. . . . 96
5.14 Sectioning of the silicon taper over a polymer slab. . . . 96
5.15 Length variation of each 10 sections of the SOI taper. . . . 97
5.16 Alignment shift effect comparison between linear and non-linear silicon tapers. 98
5.17 Alignment shift effect due to wavelength in the C-band. Taper 1 is 179.5μm long and Taper 2 is 277.5μm long. . . . 98
5.18 X-normal cut of the electric field distribution at 1550 nm for (a) linear and (b) non-linear tapers. Both are 179.5μm long. White lines contour the waveguide polymer (0 to 1μm) and SOI (3.5 to 3.72μm) cores, while dotted line indicates the approximate beginning of the power transition. Dashed arrow shows the direction of propagation. . . . 99

6.1 Geometry of a simple directional coupler. 118

List of Tables

2.1 Operating characteristics according to Gigoptix. 26
2.2 Commercial requirements for electro-optic polymers. 36

3.1 Optical properties of the TFPS modulator materials. 39
3.2 Variations of h_{uv}, h_{lp}, h_c $\lambda_0 = 1.55$ μm. 42
3.3 Material characteristics of the TFPS modulator. 43
3.4 Accumulated phase shift over L_h in one of the arms of the MZ polymer modulator. ($\lambda = 1550$ nm). 54

4.1 P802.3bs IEEE standard recommendations for 400Gbit/s over 2km and 10km on SMF. 63
4.2 OIF transmitter package implementations agreement. 64

5.1 10 Segment Maximum values and taper widths. 94
5.2 Optimized non-linear tapers details. 97

Notation and Acronyms

SOI	Silicon-on-insulator
TL	Transmission line
TE	Quasi-Transversal Electric
TM	Quasi-Transversal Magnetic Mode
PCB	Printed Circuit Board
PIC	Photonic Integrated Circuit
DSP	Digital Signal Processing
RF	Radio Frequency
TFPS	Thin-Film Polymer over Silicon
TOSA	Transmitter Optical Subassembly
PSK	Phase-shift keying
QPSK	Quadrature phase-shift keying
PAM	Pulse Amplitude Modulation
CMT	Coupled Mode Theory

X, Y, Z	Cartesian variables
ϵ	permittivity
μ	permeability
k	wave number
$C_{AB,BA}$	coupling coefficients
n_{eff}	effective refractive index
n	refractive index
λ	wavelength
c_0	light-speed in vacuum
β	propagation constant
Z	line impedance
σ	conductivity
α	loss
R	resistor
C	capacitor
L	inductor

Contents

1 Introduction **18**
1.1 Scope of this Thesis . . . 20
1.2 Original Contribution . . . 21
1.3 Outline of this Thesis . . . 22

2 Background **24**
2.1 Optical Communication System . . . 24
2.2 Transmitter optical sub-assembly . . . 25
2.2.1 Electrical Interconnects . . . 25
2.2.2 Optical interconnects . . . 28
2.3 Optical modulators . . . 30
2.3.1 Pockels effect . . . 32
2.3.2 RF electrode . . . 32
2.3.3 Silicon modulator . . . 33
2.3.4 TFPS modulator . . . 33

3 Polymer Electro-optic Modulators **37**
3.1 Optical waveguide design . . . 38
3.1.1 Materials . . . 38
3.1.2 Modal analysis . . . 40
3.2 Electrode design . . . 42
3.3 Electrooptical properties . . . 50
3.3.1 Half-wave Voltage (V_π) . . . 50
3.3.2 Electrooptic bandwidth . . . 50
3.4 Bias circuits . . . 51
3.4.1 Thermo-optic effect . . . 52
3.4.2 Electro-thermal effect . . . 55
3.4.3 Measurements . . . 56
3.5 Summary . . . 58

4 Transmitter optical sub-assemblies: Electrical Interconnects **60**
4.1 Design Methodology . . . 60
4.2 Industry standards for optical telecommunication networks . . . 62
4.3 Electrical Interconnects . . . 64
4.3.1 Materials . . . 64
4.3.2 Wire bonding . . . 66
4.3.3 Electrical Feed by Connectors . . . 69
4.3.4 Electrical Feed by Multipin RF Layouts . . . 71
4.3.5 Termination circuit . . . 76

4.4 Electrical Path . . . 79
4.4.1 Single-ended Modulator . . . 79
4.4.2 Quadrature Modulators . . . 80
4.5 Electrooptic bandwidth . . . 81
4.6 Summary . . . 83

5 Optical Interconnects **84**
5.1 Design Methodology . . . 85
5.2 State of the Art for Optical Interconnects . . . 86
5.2.1 Lens Array . . . 86
5.2.2 III-V to SOI . . . 86
5.2.3 Fiber to SOI and vice versa . . . 87
5.3 EO polymer modulator and SOI interface . . . 88
5.4 Coupling analysis . . . 89
5.5 Optimized Silicon Taper . . . 91
5.5.1 Linear Taper Design . . . 92
5.5.2 Non-linear Taper Design . . . 94
5.6 Summary . . . 97

6 Conclusion **100**

References **117**

Appendix 1 **118**

Chapter 1

Introduction

It is undeniable that there is an increasing demand for high data rates not only for human consumption but, more recently, the high demand for machine-to-machine traffic has arisen from data-centric applications, sensor networks and the growing penetration of Internet-of-Things. Fiber optical communications are to enable a cost-effective network scaling from ultra-long-distance networks, such as submarine, to metro and user networks. By using wavelength division multiplexing, the optical transport systems are capable of carrying around 100 optical signals at 200 Gbit/s each, on a 50 GHz optical frequency grid, for an overall capacity of about 20 Tbit/s on a single optical fiber [1]. To achieve such rates optical parallelism was introduced. Given that the signal is complex, the field's real and imaginary parts can be modulated independently. Another way to further expand data rates is by modulating different polarizations with individual signal streams, which is called polarization division multiplexing.

Most of the functioning 100 Gbit/s optical communications systems modulate four parallel electrical signals at around 30 Gbit/s (25 Gbit/s, plus overhead for forward error correction) [2]. To enable parallel optical systems it is necessary to extract the full optical field information at the receiver. Hence, the receiver needed to change from direct detection of the pulse intensity to coherent detection [2–4] of the optical field to achieve large distances. However, including coherent detection to a transceiver adds to the implementation costs, which can be overlooked when working in long-haul, which encompasses distances between 400 km and 3000 km, and even metropolitan networks from 40 to 400 km [5], but raises concern when working in near-to-client distances or data centers applications [6–8], that is, according to the literature, around 100 km on a single-mode fiber at 1550 nm.

According to Liga *et al.*, next-generation long-haul transceivers will use powerful forward error correction and high-spectral-efficiency modulation formats (combination better known as coded modulation). One of the advantages of coded modulation is that coding gain can be achieved without bandwidth expansion or reduction of data rate [9]. Nonetheless, it affects the overall cost considerably. Moreover, with wavelength-division

multiplexing and advanced modulation formats, transmission network cost for long-haul and metropolitan distances is dominated by the transceivers. The rising costs for these complex transceivers are a fundamental concern for network operators as they are expected to provide more bandwidth without affecting the final price. For this reason, carriers have to reduce their price per bit per second while installing more equipment to achieve even more complex network architectures. When approaching the client side of the network or working with data center interconnects [10–12], it gets more convenient to increase the bit rate per lane to deliver newly standardized 100G and 400G applications [13, 14] in order to use direct detection and rescind the need for coherent detection reducing the overall cost of the transceiver module. Furthermore, optical parallelism in the form of high-order modulation formats, such as pulse amplitude modulation or quadrature amplitude modulation [12, 15, 16], is enough to achieve such rates efficiently if the integrated active device responsible for modulating the optical signal has wide band and an a small drive voltage. A direct solution to these essentials is the improvement of photonic integrated technology.

Photonic integrated circuits or planar lightwave circuits are devices with several optical and electrical components [17]. Integrated optics can be defined as the technology that enables such devices to be manufactured on a wafer/chip scale. Although photonic monolithic integration complexity has clearly improved in the last few years for instance, in 2013 up to 256 photonic devices were integrated into a single chip for an 8×8 wavelength switch, they are still more expensive than their microelectronic counterparts by several orders of magnitude [18]. As many laboratories seek to solve this issue by trying to increase the on-chip integration capacity, the industry of today choses multi-platform integration systems for complex photonics systems and hybrid combinations of multiple platforms to create complex photonic integrated circuit assemblies [19]. These platforms, which are conformed by different materials, provide the hybrid system with specific and specialized functions such as modulation with III-V materials and electrooptic polymers [20, 21], amplification, which uses III-V materials [22], lasing [23–25], passive optical devices fabricated in silicon-on-insulator [26–28], among many others.

Organic electrooptic materials have been recently used for a variety of devices ranging from hybrid silicon platforms [29–31] to polymer on silicon thin-film platforms [32, 33]. The latter device configuration allows for low-contrast high-performance electrooptic modulators which have demonstrated to be very reliable. Reliability studies of the electrooptic polymers in photostability [34], thermostability [32, 35, 36], environmental stress [37], high control of molecule mobility and steric hindrance [38]. These studies point towards the trustworthiness of electrooptic polymer modulators for high-speed wide-band applications in data-centers covering distances greater than 100 km with above 100G speeds as demonstrated in [12, 39–41]. Furthermore, electrooptic polymer modulators have very low voltage driving when compared with III-V modulators, such as lithium niobate,

for high-speed applications with 40GHz [42] and up to 100 Gbps at chip level as seen in [33, 43] which reduces the operating energy of the transmitter even more. Commercial packaging for electrooptic polymer modulators has been developed and has proven to work adequately for long-reach data center applications with a 50 GHz bandwidth which is suitable for 100 G-per-wavelength in pulse amplitude modulation at 56 Gb achieving a transmission over 140 km [12].

As the complexity of hybrid photonic systems increases, the need for standardization of the packaging assembly becomes very relevant prompting international institutions such as the IEEE (Institute of Electrical and Electronics Engineers) and the OIF (Optical Inter-networking Forum) to release documentation on assembly recommendations and general requirements for the industry. Every packaging design as a system has to fulfill these recommendations as an expected minimum.

Photonic integrated circuits packaging general needs are driven by three pillars according to (OFC-2017-SC450-PIC) [44]:

- The status of the product development: Practicability, fabrication capacity, prototyping and series production.
- High-performance interfaces: Optical interfaces or interconnections, electrical interfaces or interconnections, mechanical interfaces.
- Field of application: Telecommunications, Datacom, Microwave Photonics, Biological Science, Metrology.

According to the recommendations above, hybrid-platform photonic integrated circuits need to have personalized packaging design methodology before stepping into mass production. Since no standardization is found in the literature for electrooptic polymer modulator based transmitters packaging, this work proposes a methodology to design interfaces for transmitter modules which integrate light source and passive circuitry besides the electrooptic polymer modulator chip, namely widely used silicon-on-insulator, III-V material platform for active light source devices and single mode fiber interfaces.

1.1 Scope of this Thesis

This work's scope includes the electrical and optical interfaces for the packaging design of a polymer modulator based transmitter hybrid integrated circuit device. The status of the product development that will be addressed in chapters 3 to 5 is that of feasibility, practicability and personalization of the interfaces which leads us to mass production-ready designs.

The high-performance interfaces addressed in this work are optical interfaces, referring to optical interconnection devices in the 1550 nm window, and electrical interfaces,

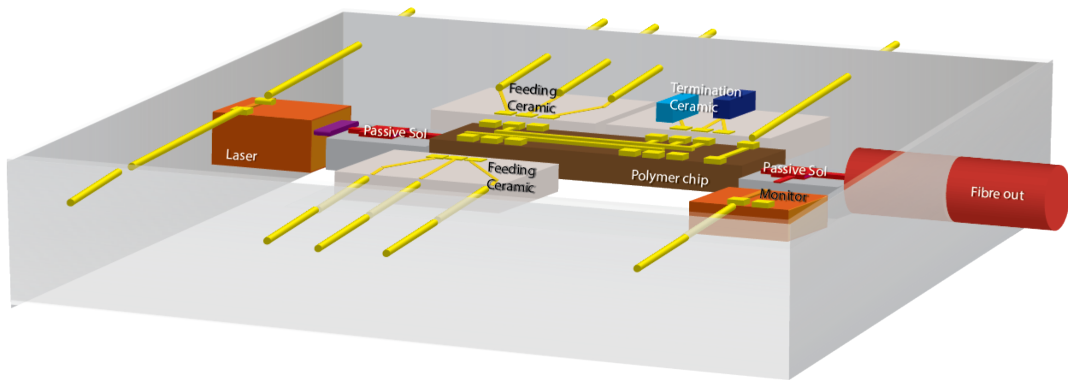

Figure 1.1: Illustrative representation of a transmitter optical sub-assembly showing light source, passive silicon-on-insulator optical circuitry, the electrooptic polymer chip. High speed radio frequency interconnects are also represented as Feeding Ceramic and Termination Ceramic.

which refers to high-speed and wide-band radio frequency (RF) interconnection devices. This work's field of application is high-speed optical networks for short metro distances or long-reach data center interconnects, which require high speed, wide band and low drive voltage without relying on coherent receivers.

This thesis will discuss aspects of optical and electrical interconnections for packaging design to meet the ever increasing telecommunication demands. By using thin-film polymer on silicon modulator we can attend high speed demands at chip level, which is very well described by Kaminow *et al.* in [45]. However, when implementing more complex hybrid integrated photonic circuits such as a transmitter optical sub-assemblies or transceiver modules (see Fig. 1.1), specific interfaces for these modulators have not been extensively discussed which leads us to propose compact and efficient interfaces for the electrooptic polymer modulator in order to preserve such good behavior at packaging level. Each individual design requirements, goals and comparison with the state of the art are better described in the introductions of chapters four and five.

1.2 Original Contribution

This thesis has the following original contributions in the field of radio frequency and optical interconnects for non-coherent telecommunication systems for long-reach data centers or near-to-user metropolitan networks:

The design of two kinds of electrooptic polymer modulator ceramic high-speed RF transmission lines (TL) interconnects for feeding and termination as depicted in Fig. 1.2.

An electro-thermal and subsequent thermo-optical simulation methodology of heaters on an electrooptical polymer modulator (see Fig. 1.3). Temperature interference

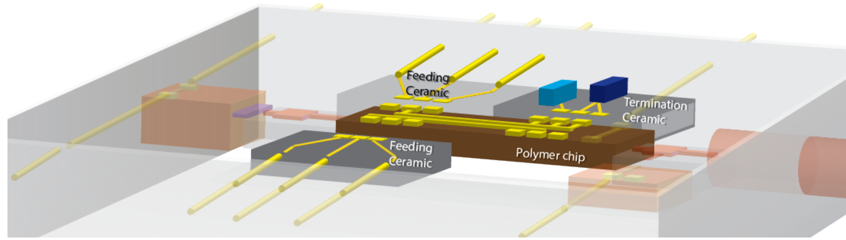

Figure 1.2: Electrical Interconnects in a transmitter optical subassembly packaging.

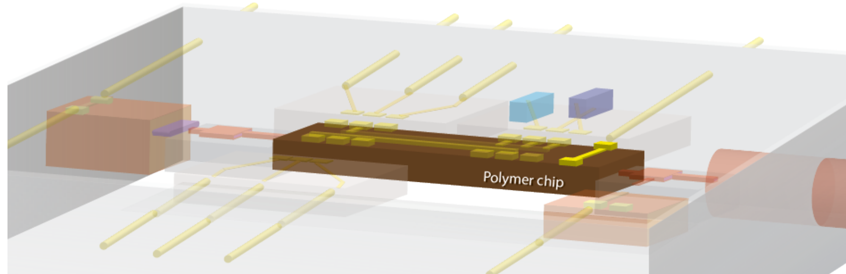

Figure 1.3: Bias circuit of an electrooptic polymer Mach-Zhender modulator.

between the two arms of the polymer waveguide Mach-Zehnder was considered.

A compact high-performance wide-band spot size converter to interconnect light from a silicon-on-insulator platform to the polymer chip as highlighted in the transmitter optical sub-assembly packaging representation shown in Figure 1.4. The design methodology includes the application of the coupled-mode theory for vertical light coupling.

1.3 Outline of this Thesis

Chapter 2 consists of a brief revision of the bibliography and several basic concepts that will be further developed in the following chapters.

Chaper 3 presents the improvements achieved in the electro-optic modulator front. Discussion of the materials, optical waveguide and electrode design. The results will be presented and compared with those of the characterization using GigOptix/BrPhotonics [46] modulators.

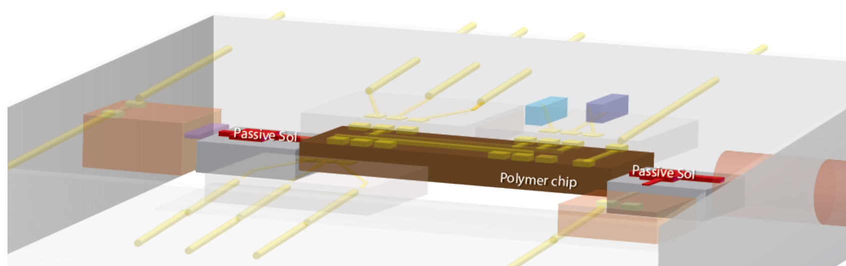

Figure 1.4: Optical interconnects in a transmitter optical subassembly packaging.

Chapter 4 shows the simulation criteria and characterization of wide-band and low-loss transmission lines interconnects for a thin-film polymer on silicon transmitter optical sub-assembly.

Chapter 5 proposes an optical interconnect for packaging applications. An inter-platform mode converter taper. This device will effectively transport light from silicon-on-insulator platform into a polymer or platform.

Finally, chapter 6 summarizes the achievements and contributions of this thesis.

Chapter 2

Background

In this chapter we will discuss some theoretical background to support and further understand the following chapters.

A brief revision of an optical communications system is presented, which will address of this thesis. Some background in radio frequency (RF) and optical frequencies interconnects in a transmitter packaging for electrooptical polymer modulators is also presented. The principle of functioning, electrooptic band and drive voltage of an electrooptic polymer modulator are also described.

2.1 Optical Communication System

A high-level architecture of a simple communication system consists roughly of a transmitter, which codes the message and sends it through a medium or channel, and a receiver, which decodes the message, as depicted in Figure 2.1. The message is converted to symbols and they travel through the medium in the form of electromagnetic waves. At the final end, in the receiver, electromagnetic symbols are demodulated and the message is decoded.

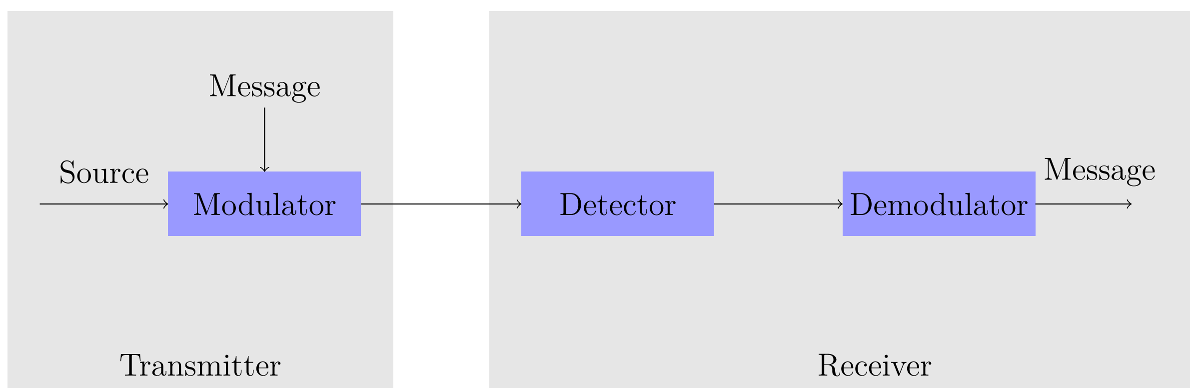

Figure 2.1: General block diagram of a communications system.

Optical communication systems are the backbone in telecommunications due to

their great channel capacity and the efforts that are put into increasing that asset [15,47–50]. Transmitter and receiver subsystems are commonly packaged into compact modules that are called transmitter or receiver optical sub-assemblies.

2.2 Transmitter optical sub-assembly

A Transmitter Optical Sub-Assembly (TOSA) most basically consists of the electrooptic (EO) modulator, interconnection circuitry, laser diode, optical interface, monitor photodiode. These devices could also include the appropriate electrical termination of modulator. The assemblies are all packed into a metallic or plastic housing for mechanical support. Its main function is to convert electrical signal to optical signal [51].

The demand for this high throughputs, very low cost and low power data transmission for short-reach metro networks and inter-data center interconnects, which are around a single hundred of kilometers distance, raises new challenges to the optical communication technology, specifically to the physical layer. Although some works justify the use of digital signal processing (DSP) for such short-reach with the fact that wide-band components beyond 35 GHz are still under development and therefore are expensive. In [52], Sadot *et al.* used a simple DSP to achieve 112 Gb/s on a single channel using pulse amplitude modulation (PAM4) at 56 Gbaud for short-reach (500 m to 10 km) data center intra-connection and long-reach (80 km) data center interconnection. The experiment included various commercial TOSA which incorporate electroabsorption and Mach-Zhender modulators with an approximate analog bandwidth (measured at 10 GHz) of 15 GHz. Nonetheless, electrooptic polymer technology [38] offers a reliable alternative for wide-band Mach-Zhender modulators (MZM). Long-reach data center applications of these modulators were presented in [12] with 100 G PAM4 at 56 GBd over up to 140 km with a bit error rate of 3.8×10^{-3} in the C-band (40×100-GHz). For this purpose the authors used a thin-film-polymer-on-silicon (TFPS) MZM with an electrooptical bandwidth of 50 GHz with a commercial packaging which only includes the TFPS die which will be the only channel that was put into test. In this regard, the integration of more passive and active elements inside the TOSA packaging could enable us to perform multi-channel tests and subsequently prototypes and products for high speed demands.

Let us divide the study of the interconnections required inside a TOSA into electrical and optical sub-assemblies as introduced in section 1.1.

2.2.1 Electrical Interconnects

The tiny dimensions that a TOSA aims to reach make wire bonding an acceptable way for the electrical interfaces to interconnect [51] in a modular way and could potentially make it possible to interchange pieces of ceramic for personalized dies with low

loss.

Also, for application purposes, flex circuitry could be added to interconnect the electrical path inside a TOSA to a PCB circuitry that includes the driving currents, carries the RF signal and could also have its own standalone controller for common applications such as data links [19].

One of the goals of this work is to present a TOSA assembly complete with RF and laser-to-chip interconnections. This project was realized in the scope of a BrPhoronics/CPqD/Gigoptix coalition to massively produce the TFPS polymer modulator TOSAs working at 100gb/s [53]. Several improvements were developed, in particular, the proposal of a new version of the modulation device, including major bandwidth improvement, even smaller footprint, better RF design for minimal losses that we will attack in two fronts: the MZM electrode and the TOSA package.

Figure 2.2(a) shows the Gigoptix DP-QPSK die used in the previous TOSA design. The cross section (see section 2.2(b)) of one arm of the MZM shows the EO polymer waveguide core surrounded by low refractive index contrast cladding. The RF contacts and bond pads are fabricated in gold, maximizing the conductivity and minimizing the RF loss. This thin film structure is seated on a silicon substrate for better mechanical resistance. Further characteristics of this device are shown in Table 2.1.

Parameters	Typical Values	Units	Conditions
Data input voltage	+/-3	Vpp	25 Gbps
DC Bias Current	0 - 90	mA	
Optical input power	20	mW	
RF	AC coupled		
Wavelength	1528 - 1590	nm	
Optical Insertion Loss	9.0	dB	
Chrip	-0.2 - +0.2	dB	
Electro-optical bandwidth	28	GHz	-3 dB
Electrical return loss	-10	dB	below 25 GHz
Drive voltage (V_π)	2.2	V	
ΔV_π	0.2	V	
Chip area	3.2×25.7	mm^2	

Table 2.1: Operating characteristics according to Gigoptix.

It is important to note that the polymers used in Fig. 2.2(b) can be easily deposited over almost any surface, and they are highly compatible with common CMOS process etching, allowing for an easy waveguide fabrication. Also its large dimensions make it possible to fabricate in up to $4\mu m$ transistor channel technology.

Transmitter and receiver optical sub-assemblies modules are the core elements to transform electrical signal into optical and vice-versa, respectively. Many works seek to minimize their size and improve their performance, which is currently measured by electro-optical band and total energy used in the system. Advances towards mass production

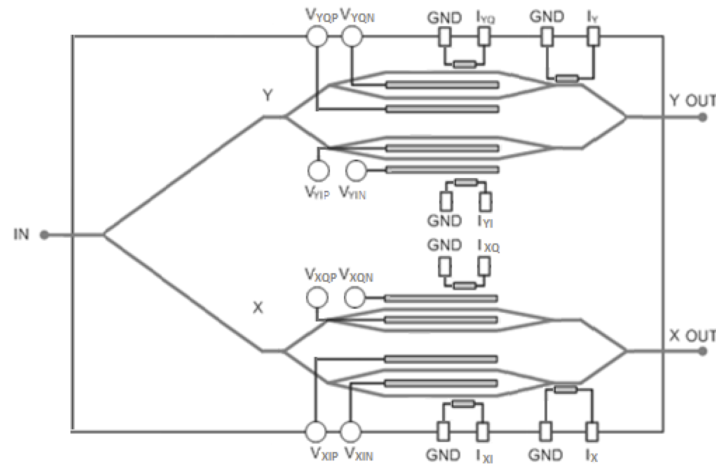

(a) Device diagram of a 100 Gb/s DP-QPSK modulator chip by Gigoptix.

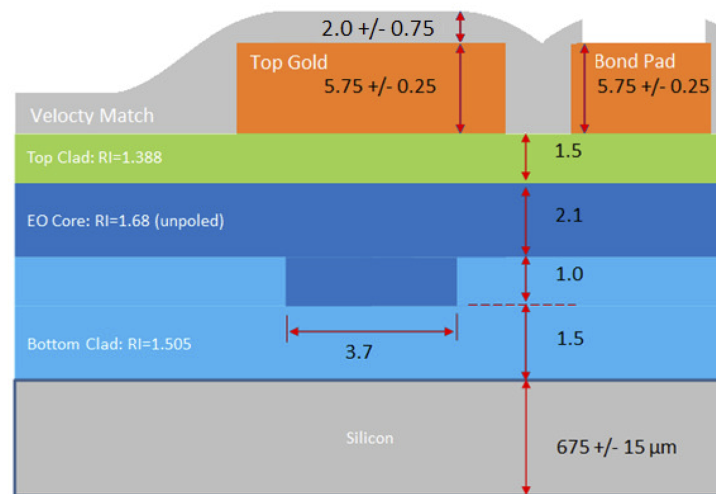

(b) Cross section of the MZM modulator (in microns).

Figure 2.2: Polymer modulator schematic from [45].

readiness were already made [54].

Let us define a TOSA carrier platform as a test bed for the TOSA as depicted in Fig. 2.3. This electrical platform function is to interconnect the TOSA carrier terminals to the Electrical test source (V_{in}). The importance of this carrier is to protect the TOSA. Connecting and disconnecting several times could cause misalignment and early damage to the TOSA as a product.

A generic single signal path circuit is presented in Figure 2.4 and represented in Fig. 2.3. There are three stages of transmission lines, the $TL_{carrier}$ represents the transmission line of the TOSA carrier circuit, TL_{TOSA} is the transmission line of the TOSA itself and TL_{mod} is the modulator electrode. Interconnections between these TLs are represented by single impedances in series. First, the interposer, as a platform to interconnect the TOSA carrier and TOSA, and lastly the impedance due to the interconnection of two pads via wire bonding ($Z_{bonding}$).

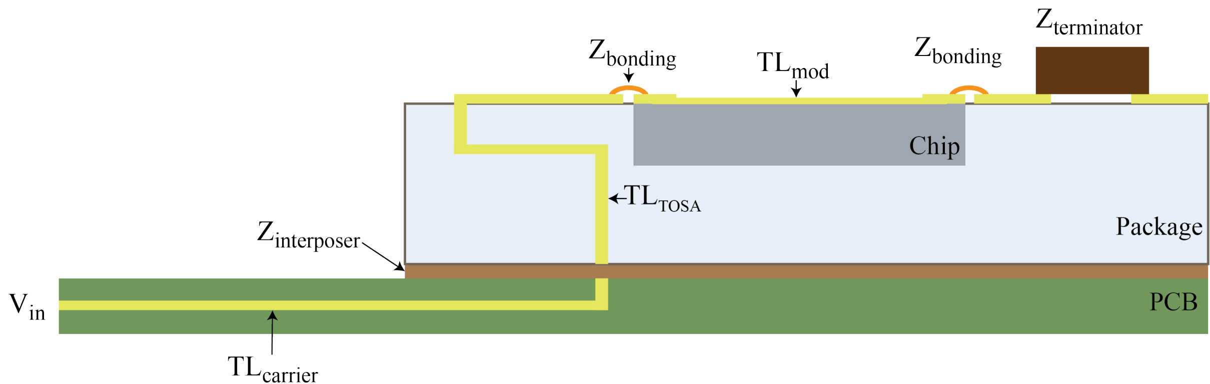

Figure 2.3: Longitudinal cut representation of a single high speed interconnection electric path on a transmitter optical sub-assembly. The printed circuit board meets the function of a TOSA carrier. Chip indicates an arbitrary placement of the the EO polymer or TFPS chip.

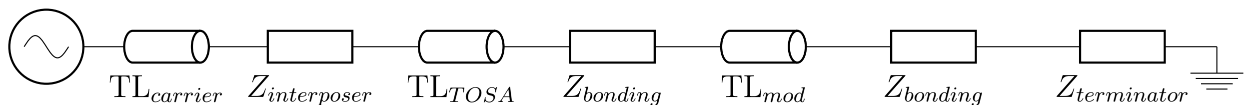

Figure 2.4: Electric signal path of the whole system. Including TOSA carrier, TOSA and Modulator electrode.

All of the Z elements in the series circuit (see Fig. 2.4) represent complex impedances which are frequency dependent and can only be considered as lumped elements when their length $l/\lambda \leq 0.01$ according to [55]. Wire bonding could potentially see challenges in this sense, which will be further discussed in Chapter 4.

2.2.2 Optical interconnects

An early full implementation of a mode-field matched laser transmitter optical sub-assembly was made by the patent [56] in 1997. Here a surface emitting laser diode was mechanically aligned to an annulus where the fiber optic is inserted and direct coupling without lenses can be achieved.

Considering the channel capacity requirements of the last years, in 2004, [57] claimed that at least one electrooptic device could be embeded into their ceramic capsule and introduced the common use of lenses for better alignment between the transmitter sub-assemblies. This design also included several interconnections between the ceramic capsule and the electrooptic device and laser.

As the channel capacity demands continue to grow, more complex modulation schemes were used in TOSAs which require interconnection between chips such as [58] which achieved 100 Gb/s with a passive optical network scheme using 4PAM.

Alignment tolerance of hybrid platforms in optical sub-assemblies is very important. To solve coupling misalignment, efforts for monolithically integrated light sources

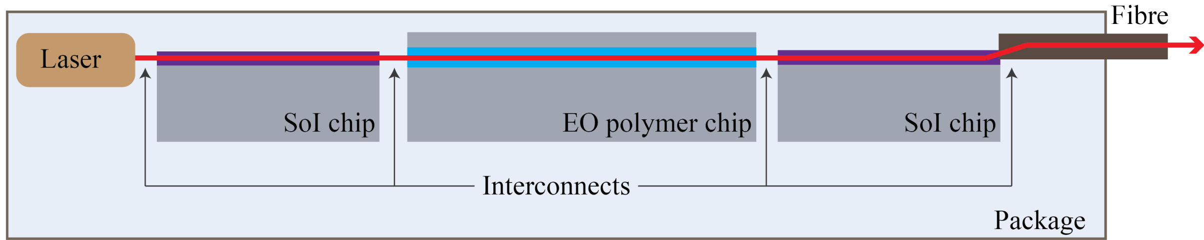

Figure 2.5: Optical signal path on a transmitter optical subassmbly. Red arrow represents signal path. Optical interconnects between platforms are indicated by dark arrows.

were made in [59]. This work uses integrated DFB (distributed feedback laser) and electroabsroption modulators (EAM) in a 40Gbit × 4 configuration, and it introduces the three-dimensional circuit board configuration in a TOSA. The laser diode, monitoring photodiode, electroabsorption modulator and a 4x1 optical mux are monolithically integrated. Only the electric lines, DC and high frequency, are mounted in a three-dimensional configuration.

The last advances in coupling without lenses were made by using DFB lasers that are attached directly to the input waveguide en face of a silica-based AWG (arrayed waveguide grating) multiplexer [60] reaching up to 100Gb/s with a 4 lane array. The total optical coupling loss was measured around 2 dB using only butt-coupling configuration.

Another famous approach to solve the alignment problem between optical platforms is to use vertical cavity emitting lasers (VCSELs) [61–67]. In these works the vertical cavity was directly coupled to the optical circuitry for each architecture. For this purpose an special adhesive can be used [68].

Another technology to couple different optical platforms is the flip-chip optical bonding. In [69] a hybrid III-V and Silicon laser is used for a transmitter. The hybrid laser consists of a SOA (semiconductor optical amplificator) and a silicon waveguide which has a mirror that complements the lasing effect. The coupling between SOA and silicon waveguide is estimated to be between 1.5 and 6.0 dB. Evidently, the lasing power is directly affected by this coupling loss.

Flip-chip approaches also employ tapers, which can be scalable depending on the project demands. In [27], SOI technology and polymer waveguides are used. An SOI core taper under a thick polymer waveguide core allows for misalignment tolerances higher than 1 μm with 1 dB and a band of 30 nm. The device total length is around 700 μm.

There is also a recent alternative approach using optical wire bonding [70] but the coupling losses of the system go up to 4.2 dB.

Contributing to this state of the art, let us assume a general looking packaging proposal for the optical interconnect path of an electrooptic polymer modulator as depicted in Fig. 2.5. Signal path is shown as a red arrow through the entire package. From the laser to the output fiber. SOI platform devices are widely known and developed to improve

passive circuitry [71–74] to manipulate light in the infrared, for instance C band (1530 - 1565 nm), as silicon is transparent in this wavelength range and its high refractive index (3.476@1550 nm) is high enough to allow an small footprint. However, when working with electrooptic polymer modulators a large mismatch of waveguide dimensions occurs. In this scenario, optical interconnects become fundamental. More specifically, the interconnection between the electrooptical polymer chip and the SoI platform will be further developed in Chapter 4.

2.3 Optical modulators

The first idea of optical modulation was based in controlling the laser drive current to change the intensity of the emitted optical wave. This kind was named direct modulation. Due to the envision of a crescent demand of higher bit rates, in the 1980s researchers migrated from direct modulation to external modulation in hopes of suppressing the effects that the latter technique caused; among them, the relaxation oscillation and frequency chirping as a result of the direct ignition and quenching of the laser. The wide bandwidth and low chirp that can be achieved with external modulation made it an attractive option [20].

External modulation can be achieved successfully by two main methods: modulation by absorption and modulation by interference. EAM stands for Electroabsorption modulator [75] and MZM for Mach-Zehnder Modulator.

A Mach-Zehnder modulator is based on the electro optical phase modulation principle. Electro optical phase modulation is based on different electro-optic materials that permit the modulated optical phase to be a linear function of the electrical drive excitation (voltage or current). An important parameter that characterizes this kind of modulators is the V_π, that is the required drive voltage to generate a π phase shift [76]. In addition to that effect, MZMs also use optical interference as the name suggests. Splitting the light into two arms, and using the phase modulation principle in one or two of their branches, it adds the amplitude modulation to the phase modulation if the two arms are recombined by another interference generating structure [5]. The output signal is as follows [20]:

$$E_o(t) = E_i \frac{1}{2}\{e^{j\pi V_1(t)/V_\pi} + e^{j\pi V_2(t)/V_\pi}\} = E_i e^{j\pi[V_1(t)+V_2(t)]/(2V_\pi)} cos\left[\pi\left(\frac{V_1(t)-V_2(t)}{2V_\pi}\right)\right] \tag{2.1}$$

where E_i is the electric field at the input , E_o is the electric field at the output and the two potentials $V_{1,2}$ are placed as depicted in Fig. 2.6. Assuming that the phase modulation depends on the drive voltage linearly. It can be noticed that the modulated output signal has two characteristics: first the amplitude is a sinusoidal function of $\Delta V(t) = V_1(t)-V_2(t)$,

second, the phase depends linearly on the sum of the two drive voltages. All drive voltages are normalized by V_π.

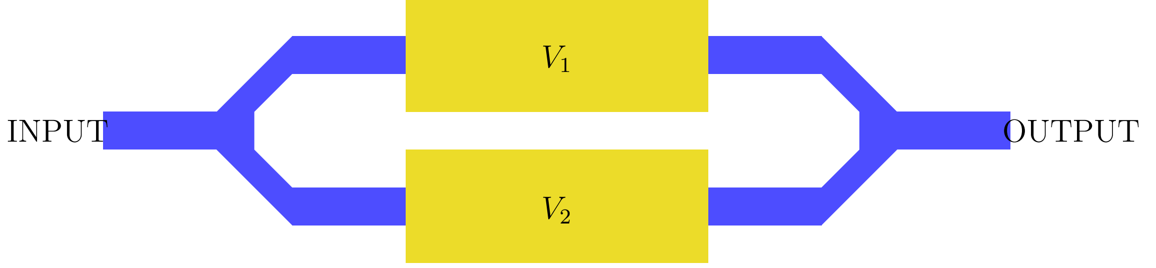

Figure 2.6: A Mach-Zhender electroooptical modulator showing potentials V_1 and V_2. Blue represents optical path while electric potentials are yellow.

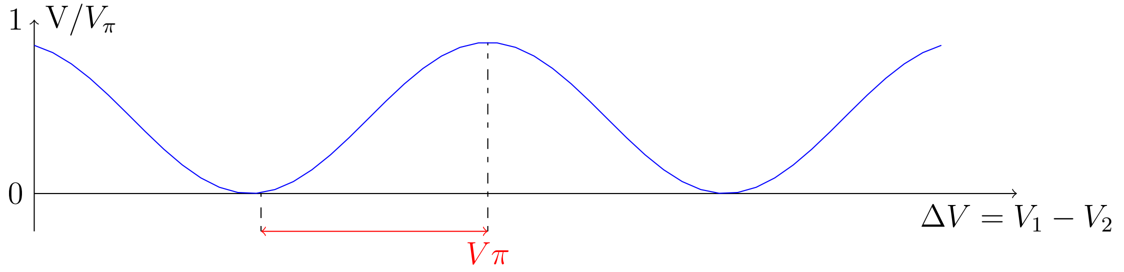

Figure 2.7: Sinusoidal MZM response indicating V_π.

Let a single drive Mach-Zehnder phase modulator have the data shown in Fig. 2.8(a), where the signal V is normalized to V_π and is only applied to one waveguide path. A "push-pull" or dual drive structure modulates the phase of both paths (with one electrode each) with the opposite phase shift. From (2.1), each arm has the opposite phase $\pm\pi\Delta V(t)/2V_\pi$, where V_π is π phase voltage for the two phase modulators. The output field is as follows:

$$E_o = \frac{E_i}{2}\left[e^{-j\pi\Delta V(t)/2V_\pi} + e^{j\pi\Delta V(t)/2V_\pi}\right]$$

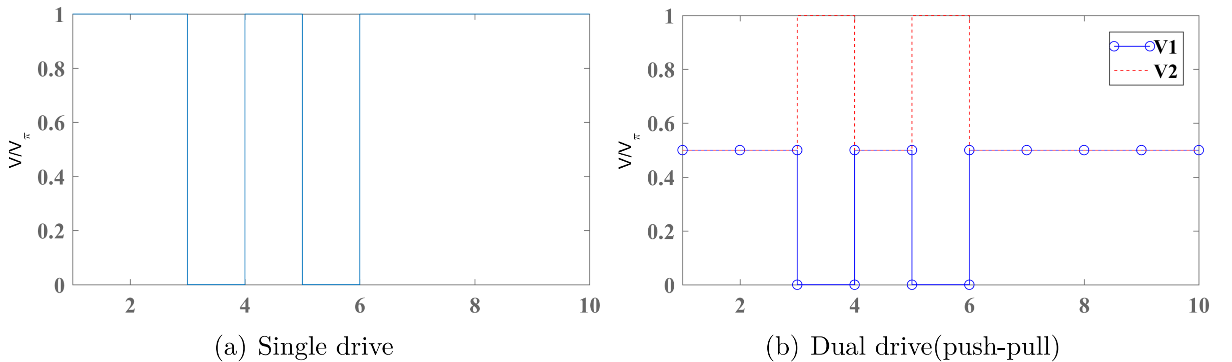

(a) Single drive

(b) Dual drive(push-pull)

Figure 2.8: Push-pull applied voltage configuration versus single drive.

which leads us to

$$E_o = E_i \cos\left[\frac{\pi}{2}\frac{\Delta V(t)}{V_\pi}\right] \quad (2.2)$$

Hence, when applying data and inverted data (see Fig. 2.8(b)), the optical output will be chirp free, if we change the amplitudes of the driving signals the chirp can be adjusted. The benefit of a push-pull modulator when compared to a single electrode modulator is that it enables lower driving voltages in each arm. The drawback resides in the fact that fine matching is needed and it gets challenging to quantify the chirp of such a configuration [77].

To achieve phase modulation of light with an RF signal on a single optical waveguide, the material has to present electrooptic properties. The most common of them is the linear electrooptic effect, which is also known as the Pockels effect.

2.3.1 Pockels effect

The electro-optic materials that make possible an EO modulation exhibit the Pockels effect, which is a linear electrooptic effect. The refractive index variation depends linearly according to: $\Delta n = \frac{1}{2} r n^3 E$, where r is the linear electrooptic constant, n is the refractive index. Lithium niobate exhibits a natural Pockels effect, while crystals like Silicon do not, but it can be induced by stress [78]. Recently developed poled chromophore polymers also exhibit high electrooptic Pockels constants (r) [79].

The linear variation of the refractive index with the electric field allows for a better control of MZM. The Pockels effect strongly depends on crystal orientation and, in the case of the chromophore polymers it depends on the polarization of molecules called chromophore [34].

2.3.2 RF electrode

The driving RF signal has to be correctly applied to the MZ structure. One way to accurately calculate the effects by RF in the MZM is to use the traveling wave electrode (TWE) design to model the electrode. As discussed above the modulation results from the interaction between electrical and optical signals. In order to achieve higher bandwidth, the signals in the electrode and the optical waveguide have to travel in the same direction.

If we take the modulated signal described in eq 2.1 and rewrite it so that it propagates along the Z direction with a pulse shape for we have;

$$E_o(t,z) = E_i \frac{1}{2} e^{j(\omega_1+\omega_2)t - j\beta z} + e^{j[(\omega_1-\omega_2)t-\beta z]}$$

where β is the propagation constant, $\omega_{1,2}$ are the angular frequency. But the propagation constant is actually dependent on frequency. It is not the same for both ω_1 and ω_2.

The variation of the propagation constant with the angular frequency is known as group velocity $v_e = \partial\beta/\partial\omega$, where v_e is the velocity of the envelope (RF signal). On the other hand, the group velocity of the waveguide v_o is material and wavelength dependent. The group velocity and the RF velocity have to be matched $v_o = v_e$ to avoid phase mismatch, especially when operating in pure phase modulation. The quality of the modulated signal depends on the modulation depth, which is also strongly dependent of the matching velocities.

It is important to consider the impedance matching to avoid counterpropagant waves in the RF lines. The source impedance is usually set at 50Ω, the Z_L line impedance and the device's impedance are to be considered for the impedance matching.

2.3.3 Silicon modulator

Up until now we can conclude that Mach-Zehnder modulators fabrication limits us to the use of high EO linear coeficient materials. Today, industry widely uses $LiNbO_3$ MZM for 40Gb/s modulation, but bit rates up to 100Gb/s have been demonstrated [80]. LiNbO3 technology produces a highly linear electro-optic constant and thus low V_π (up to 2V). However the large footprint that this technology produces makes it inviable for future technology roadmaps. This made researchers focus also in III-V, that already showed bit rates up to 80Gb/s [81]. Additionally, III-V modulators can be integrated monolithically with a laser.

Silicon is an abundant material, it has high mechanical strength and a high quality oxide (SiO_2). The oxide along with a silicon core makes a high contrast refractive index waveguide. Such tiny dimensions cannot be achieved by III-V materials.

In terms of electro-optical modulators, Si is a weak electro-optic material. Its crystal nature makes it impossible to exhibit any linear electrooptic effect, like the Pockels effect [20] in $LiNbO_3$. Some efforts in changing the refraction index by introducing strain in Si by Si_3N_4 made possible a Pockels effect, but for small cross sections dimensions the strained Silicon offers high nonlinearities [78].

On the other hand the silicon waveguide allows the carrier depletion or plasma effect (movement of carriers along the cross section of the waveguide). Free carriers alter the real and imaginary parts of the Silicon dielectric constant, thus we have the electrooptic effect required. Although this method exhibit additional nonlinearities due to the carrier-depletion effect in Si, which is not found in lithium niobate modulators, there are significant efforts to compensate this undesired effect [21].

2.3.4 TFPS modulator

Silicon modulators are the most attractive solution for monolithic integration purposes. Although many breakthroughs and advances have been developed [82] such

as: different silicon-doping methodologies using self-aligning processes [83], 26 GHz of electrooptic band with $V_\pi L_\pi = 26$ V.mm was demonstrated [84] and more recently, there has been development on silicon-SiO_2-ITO hybrid modulators based on tunable plasmonic directional couplers [85, 86] which could provide transmitter optical sub-assembly ultra-wide band and very small footprint The most challenging problems with hybrid-silicon modulators are the high capacity of the slot waveguides [87]; the ultra-high refractive index contrast allows for small footprint but it could potentially be partly responsible for velocity mismatching.

Lithium niobate, the current most commonly used electrooptic material, has an electrooptic coefficient of 35 pm/V which permits V_π voltages on the order of 5 V to be reasonably achieved [88]. For organic materials to compete with lithium niobate for use in low V_π devices, the electrooptic coefficients must equal or exceed that of lithium niobate. The advantages of polymer waveguides used in the design of electrooptic modulators are ultra fast response, low drive voltage and ease of scalability based on the polymer material. It is also very important to note that these devices are designed with a low cost manufacturing.

The electrooptic polymer is defined as an electrical field sensible particle inside a polymer guest. The name of this molecule is chromophore [89] (see Fig. 2.9). This molecule has to be synthesized considering two main characteristics, hyperpolarizability and low optical absorption at the intended operational wavelength. Furthermore, chromophores must be capable of being incorporated into their host polymer substrate and show suitable chemical and thermal robustness to endure subsequent processing and device operating conditions.

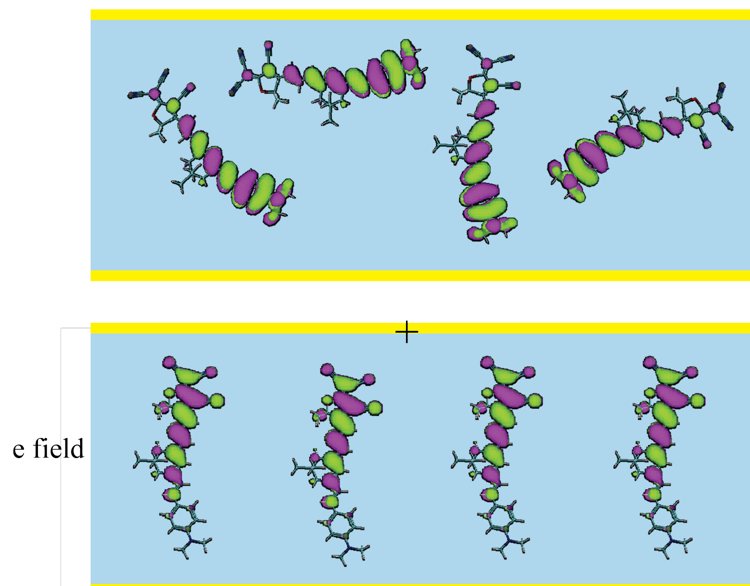

Figure 2.9: Poling process of the chromophore molecules inside a polymer host. [45].

When a very strong electric field is applied for a period of time over the

compound (host polymer and guest chromophores), as seen in Figure 2.9, the polymer characteristics are altered and the molecules that have high polarizability align in the direction of the electric field, changing the characteristics of the compound and making its electrooptic constant boost in the polarization direction [89]. This process is called poling of the electrooptic polymer.

One of the main advantages of EO polymer modulators is that the optical refractive index is close to the microwave index, thus allowing for better velocity matching, helping to achieve low drive voltage and broad bandwidth [90].

The typical requirements for the use of electrooptic (EO) polymers in commercial electrooptic modulators are cited in Table 2.2 according to [45]. The anatomy of this modulator is shown in Fig 2.10 [46]. It is important to note that for the waveguide formation, the requirements of the OE polymer process include photolithography and plasma etching.

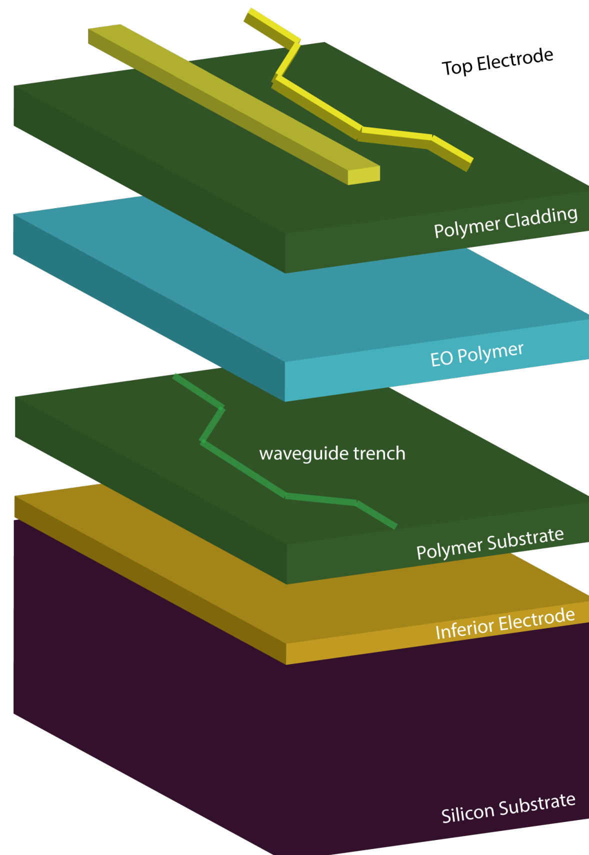

Figure 2.10: Anatomy of an EO polymer MZM from [45].

The first notice of a commercial EO polymer modulator [91] already achieved 100Gb/s. Early single EO polymer MZM achieved 40 Gb/s [92]. Currently the typical bandwidth of a single MZ EO modulator is more than 100 GHz [93] [94].

Parameter	Requirement	Notes
EO coefficient	$r_{33} > 80pm/V$	For low V_{π} modulators
Optical loss	$<$ 3dBm/cm	at 1300-1550nm
Refractive index	similar to the RF freq.	low enough to ensure low coupling loss
Operating temperature	-5 °C to 75 °C	
Process	photolithography and plasma etch	
Cost	relatively low	
Repeteability	high	

Table 2.2: Commercial requirements for electro-optic polymers.

Chapter 3

Polymer Electro-optic Modulators

This chapter will study a systematic general modeling of an electrooptic polymer modulator for interconnection study purposes which will be discussed in the following chapters. TFPS modulators data were provided through partnership with BrPhotonics-Gygoptix. Figure 3.1 shows a general schematic of their LX8242 TFPS modulator high speed RF path and waveguide core.

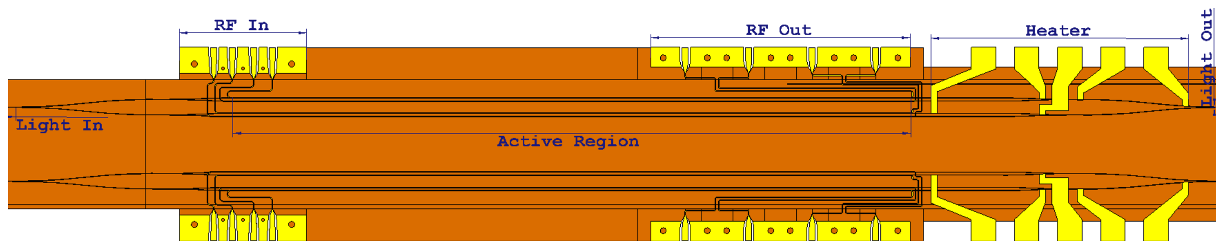

Figure 3.1: LX8242 DP-QPSK TFPS modulator by Gigoptix/BrPhotonics schematic. Upper gold trace is shown in yellow, while bottom plane metalization is orange. Optical waveguide trench is shown in blue.

For better understanding we are dividing this study into four parts. Optical waveguide design, electrode design, heater design and electrooptical performance. Optical waveguide design will consider the polymer and semiconductor materials working at an optical communications wavelength (1550nm). Electrode design will use effective methods to a low loss electrical path and will also address the velocity matching problem ($v_o = v_e$). Heater design will apply the joule effect to obtain the desired pi phase to ensure the correct functioning of the Mach-Zehnder structure of our polymer modulator. Electro-optical performance will address V_π simulation and system bandwidth.

3.1 Optical waveguide design

3.1.1 Materials

Silicon is one of the most abundant elements in planet Earth and the Silicon-on-insulator platform is widely used as high confinement and integration platform. However, there are still challenges to overcome the low modulation efficiency achieved in Mach-Zehnder modulator devices. Nonetheless, these problems don't make it less attractive for future monolithic integration of optical transceivers for inter and intra chip networks as many passive transmitter optical circuits are very efficient and well characterized in SoI platform. On the other hand, III-V semiconductors are, in today's electrooptic industry, the most important materials. Lasers, modulators, photo-detectors and many other devices are massively produced because of the availability of indium and gallium arsenide and indium gallium arsenide phosphide are grown as epitaxial layers on top of wafer surfaces.

Polymeric materials are frequently used in optical communications based on the fact that it is possible to transform them into adequate electrooptic materials to achieve high modulation efficiency and they can be compatible with a vast number of other transparent polymeric materials in the near-infrared. Although, there are some integration problems with the TFPS platform when interconnecting with other platforms such as SoI and III-V inside a transmitter subassembly environment, they can be overcome if we design adequate out-of-chip interconnection. More details in this matter will be discussed in chapter 5.

The polymers that were used to fabricate a polymer electrooptic modulator are detailed in Table 3.1. Let us define the active material of the TFPS platform the guest chromophore in an amorphous polycarbonate host. The response of the B74-APC to reactive-ion etching is poor compared with that of a fully cured substance, such as that used in the claddings [95]. The solution adopted for this problem is to invert the rib (see Fig. 3.2) and pattern the lower cladding, obviating the need to process the active core layer.

UV15LV is a commercial polymer with very good adherence to many metals and great for its insulating properties. It provides good stability when cured with UV light and additional heat curing can be added to stabilize even more the structure [96].

LP33ND is chosen to confine the TM mode inside the B74-APC poled region, because of its low refractive index and low loss.

Electrooptic polymer

The electrooptic effect can be induced into a polymer is material using polarization sensitive molecules called chromophores. They are prepared in liquid format and then spun into a substrate like silicon, glass or other polymers, then cured to form

Material	Refractive Index (n)	Loss [dB/m]	Layer
LP33Nd	1.388	2	Upper cladding
B74-APC poled	1.734	1.2	Waveguide core (Active Region)
B74-APC unpoled	1.67	1.2	Waveguide core
UV15LV	1.505	3	Lower cladding

Table 3.1: Optical properties of the TFPS modulator materials from [97]. Properties measured at 1550 nm.

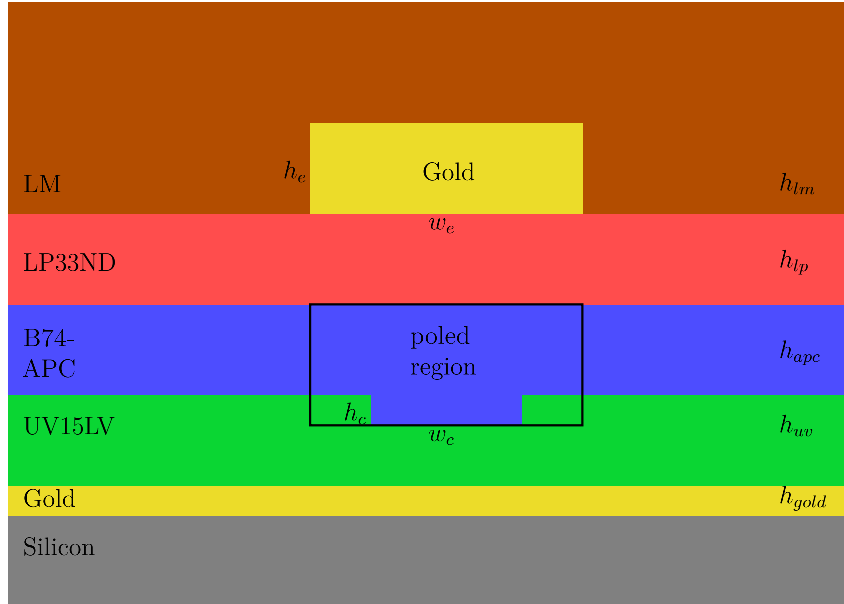

Figure 3.2: Cross section of the active section of the TFPS Mach-Zehnder modulator.

firm thin films [20]. There are three kind of Chromophore-polymer systems: guest-host, side-chain, cross-linkable. They are different in the relation between the chromophore and the host polymer matrix. Side-chain and cross-linkable EO polymer chromophores have direct bonds to the host polymer, while the guest-host system has free chromophore molecules inside a polymer substrate, which increases the poling efficiency. As our aim is to increase the performance of our modulator, it is important that we maximize the efficiency of the poling process to achieve a high EO constant (r_{33}). However, the other two systems offer better thermal stability [96, 97].

Thermal stability

Amorphous polycarbonate (APC) was chosen as the host material because of its low optical loss and high glass transition temperature (T_g), at which it's physical properties go from glass to a rubbery-like [98]. Thermal stability is strongly linked to the final T_g of the material.

First studies in thermal stability [89] show that after poling process, high EO constant (r_{33}) values were achieved (up to 263 pm/V at 1.33 μm) and thermal stability of

500 h at 85°C. New studies make us hope for better chromophore and compound materials with higher thermal stabilities and EO constants, as shown in [99], with $T_g = 120$°C and r_{33} up to 283 pm/V.

Loss

Materials of the TFPS modulator are distributed as seen in Figure 3.2. Note the poled region. The only material affected by the poling process is the B74-APC. After this process, chromophore guests are aligned inside the APC host, which causes optical properties to change according to Table 3.1. Based on this table we can define the insertion loss as:

$$IL_{tfps} = 2 \cdot \alpha_{sp} + \alpha_{\omega g} \cdot L \tag{3.1}$$

where L is the active modulation length, α_{sp} is the splitter loss, $\alpha_{\omega g}$ is the passive waveguide loss.

3.1.2 Modal analysis

Waveguide structure consists of an EO polymer inverted rib core with passive polymer upper and lower cladding.

To define the core's inverted rib geometry in Figure 3.2 an etching process in the UV15LV polymer deep enough to confine the mode horizontally was performed and the electrooptic polymer (blue) is spin-coated on top. Cladding material is LP33ND. Furthermore, a layer can be added for microstrip transmission line velocity matching purposes. Core dimensions (w_c and h_c) impact a trade-off between v_π and insertion loss.

Let us consider first the following values of the geometry variables in Fig. 3.2: $h_{apc} = 2.5\mu m$, $h_c = 1\mu m$, $w_c = 3.8\mu m$, $h_{lp} = 1.5\mu m$, $h_{uv} = 2.5\mu m$, $h_e = 5.75\mu m$, $w_e = 12\mu m$, $h_{lm} = 30\mu m$. We can get the imaginary part from the refractive index equation ($\dot{n} = n + ik$) by taking the information in table 3.1 and using:

$$k = \frac{OL \cdot \lambda_0}{20\,(2\pi)\log e} \tag{3.2}$$

where OL is the optical loss in dB/m, λ_0 is the wavelength in the vacuum. With this information we calculated the effective index of the first TM mode: $n_{eff} = 1.7179$ with 1.33dB/cm loss (see Fig. 3.3). Using Comsol Multiphysics 5.2 [100] finite-element solver on a 32 μm × 21 μm computational domain and 35120 mesh cells, modal analysis was performed. The modal dispersion in Figure 3.4 shows that TE and TM modes are close together. TM modes are chosen for better interaction with the electric field of the RF signal, which is a microstrip transmission line and will be further discussed in section 3.2.

Sweeping of h_{uv}, h_{lp}, h_c values were performed to improve the waveguide losses

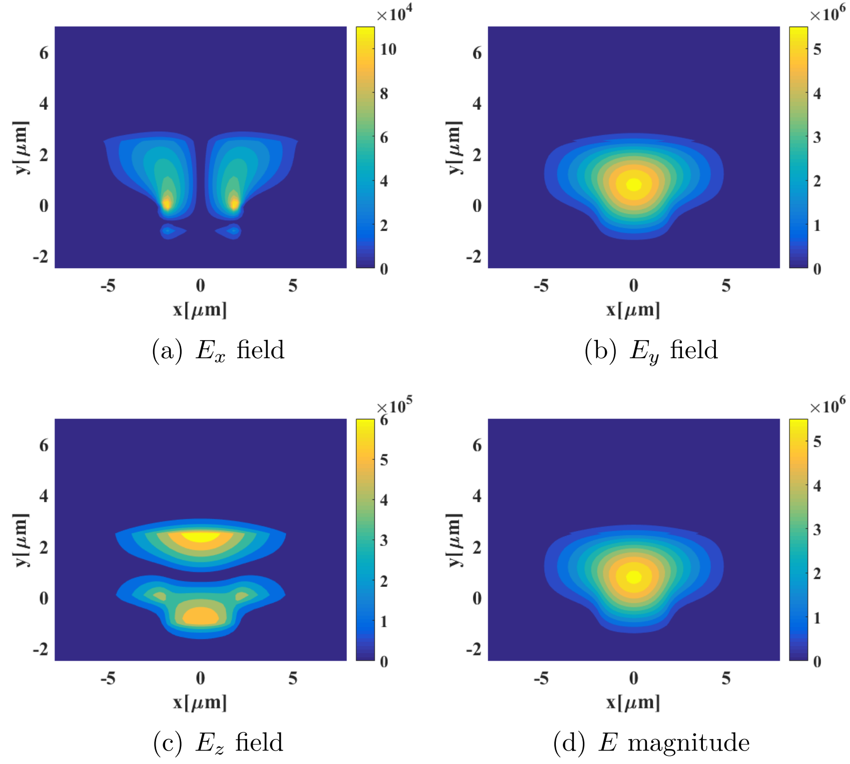

(a) E_x field (b) E_y field

(c) E_z field (d) E magnitude

Figure 3.3: Modal analysis of the TFPS modulator transversal section. TM mode at $\lambda_0 = 1.55\mu m$

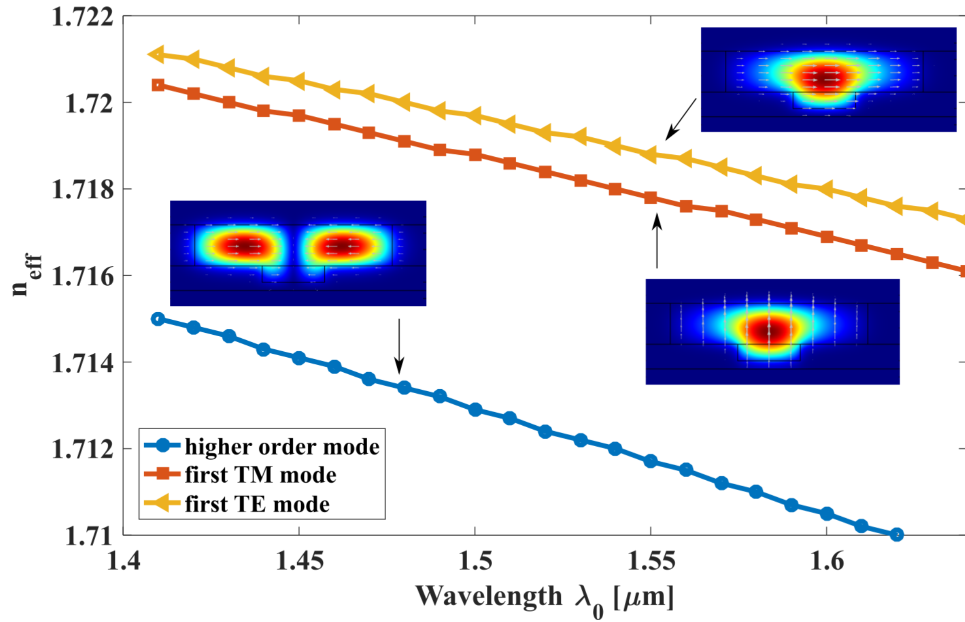

Figure 3.4: Modal dispersion of the TFPS waveguide. Inlay figures show electric field distribution and and (Ex, Ey) distribution (gray arrows).

(α_{wg}). In Table 3.2 we can infer that proximity to the gold laminate causes optical loss: the closest simulation is represented by the seventh row (waveguide core is 1.2 μm above the gold laminate and α_{wg} = 1.3611 dB/cm). h_{lp} does not contribute significantly to waveguide losses.

h_{uv} [μm]	h_{lp} [μm]	h_c [μm]	α_{wg} [dB/cm]
2.4	1.2, 1.3, 1.4	1	1.3364
2.5	1.2, 1.3, 1.4	1	1.3306
2.6	1.2, 1.3, 1.4	1	1.3278
2.4	1.2, 1.3, 1.4	1.1	1.3449
2.5	1.2, 1.3, 1.4	1.1	1.3346
2.6	1.2, 1.3, 1.4	1.1	1.3294
2.4	1.2, 1.3, 1.4	1.2	1.3611
2.5	1.2, 1.3, 1.4	1.2	1.3424
2.6	1.2, 1.3, 1.4	1.2	1.333

Table 3.2: Variations of h_{uv}, h_{lp}, h_c $\lambda_0 = 1.55$ μm.

Waveguide loss

Losses are linked to the total length of the device. As the EO polymer modulator has a Mach-Zehnder architecture, to achieve a π phase shifting a 9 mm active length is needed and the waveguide is designed to be 14.5 mm long. Optical insertion loss is around 3.1 dB.

3.2 Electrode design

While commercial semiconductor modulators use coplanar transmission line to feed the PN junction and waveguide, EO polymer modulator uses microstrip transmission line for better interaction with the TM mode of the polymer waveguide.

Electrode losses greatly impact on the EO response of the modulator. As a higher electrooptic constant contributes to smaller modulator footprint (smaller L_π), smaller dimensions also contribute to control the electrode loss.

Material characterization in the frequency range between 0.04 GHz and 65 GHz is presented in figure 3.5. If we consider an electric field of the form $\vec{E} = E_0 e^{j\omega t}$, permittivity is defined as the complex value

$$\hat{\epsilon}(\omega) = \epsilon\prime(\omega) + j\epsilon\prime\prime(\omega) \tag{3.3}$$

$$\hat{\epsilon}(\omega) = \epsilon\prime_r(\omega)\epsilon_0 + j\frac{\sigma(\omega)}{\omega} \tag{3.4}$$

where ϵ_0 is the permittivity in the vacuum in eq. 3.4. Electrical conductivity (σ) of metals are listed in Table 3.3. In case of bottom (Au film) or top (Au trace) electrodes, we set and electrical conductivity of 4×10^7 S/m or 3.3×10^7 S/m, respectively.

The entire electric path, as modeled in Figure 3.6, is shown in Figure 3.7.

Let us divide the TFPS modulator electrode design section into three basic steps according to Figure 3.6, where one can identify the electrical input and output

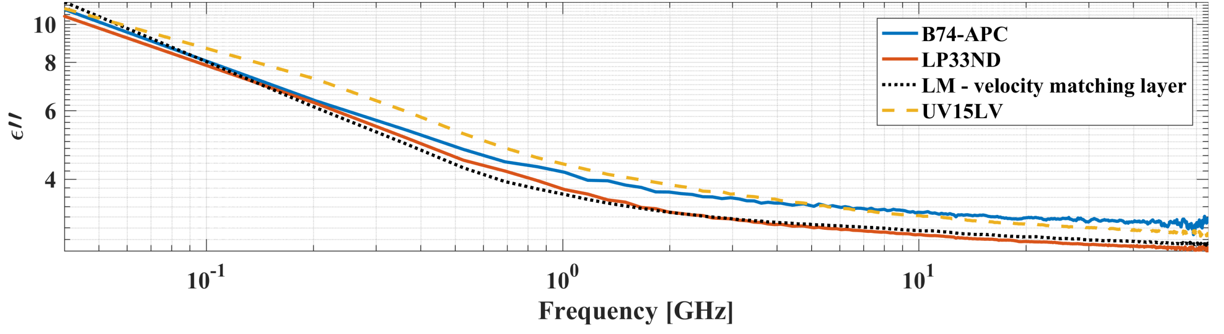

(a) Real part of complex relative permittivity.

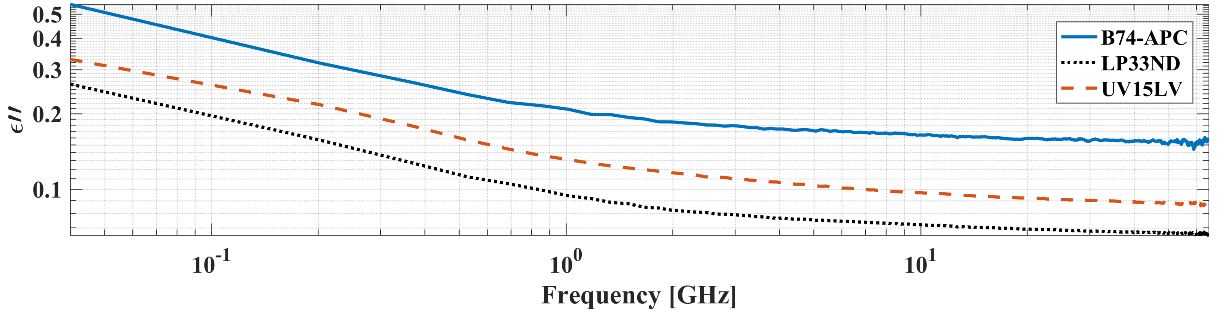

(b) imaginary part of complex permittivity.

Figure 3.5: Dispersion of the polymer materials from 0.04 GHz to 65 GHz.

Component	Parameter	Value[μm]	$\epsilon\prime_r$	σ [S/m]	$\epsilon\prime\prime$
Si	Thickness	20	11.9	-	-
Au Film	Thickness	1	-	4×10^7	-
UV15LV	Thickness	2.5	Fig. 3.5(a)	-	Fig. 3.5(b)
B74-APC slab	Thickness	2.1	Fig. 3.5(a)		Fig. 3.5(b)
LP33ND	Thickness	1.5	Fig. 3.5(a)	-	Fig. 3.5(b)
LM	Thickness	7.75	Fig. 3.5(a)	-	-
Au Trace	Width/ Thickness	12 / 5.75	-	3×10^7	-
Wg.Core	Width / Thickness	3.8 / 1	Fig. 3.5(a)		-

Table 3.3: Material characteristics of the TFPS modulator.

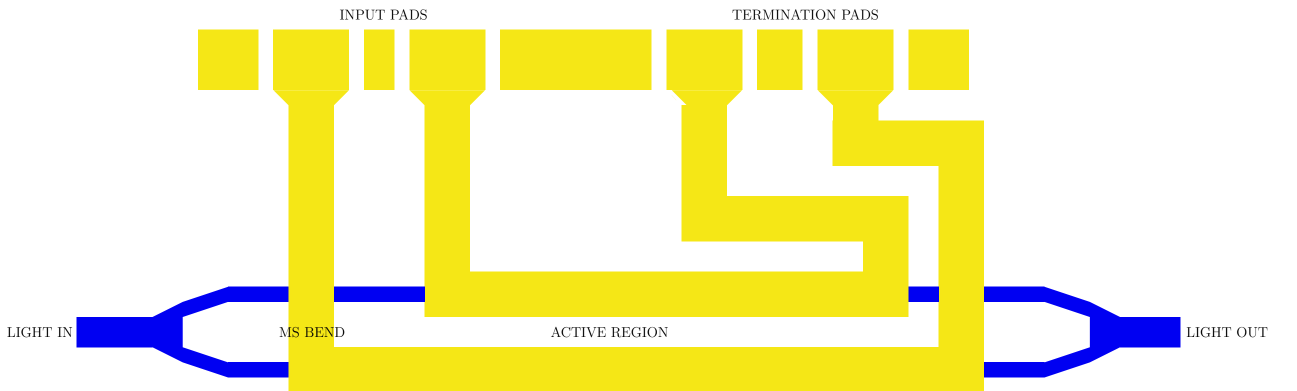

Figure 3.6: Single MZ device diagram showing light and electric signal paths in a TFPS modulator.

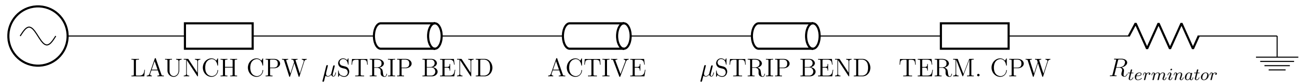

Figure 3.7: Electric signal path of the whole system. Including TOSA carrier, TOSA and Modulator electrode.

coplanar waveguide terminals, transitions from CPW transmission line to microstrip, microstrip bendings and microstrip line paths, and active region, where optical modulation occurs.

Active Region

Modal simulation of the active region cross-section uses the geometry described in Figure 3.2. Dimensions are according to the geometry information in Table 3.3.

Electric field components of the microstrip transmission line are detailed in Figure 3.8. QTEM mode is identified as having veru small Z components in comparison to X and Y components of the electric (see Fig. 3.8(c)) or magnetic (see Fig. 3.8(d)) field travel in the Z direction [101]. Power flow magnitude is highly concentrated between the electrodes, which have approximately 6.3 μm of separation between the two (see Fig. 3.8(f)).

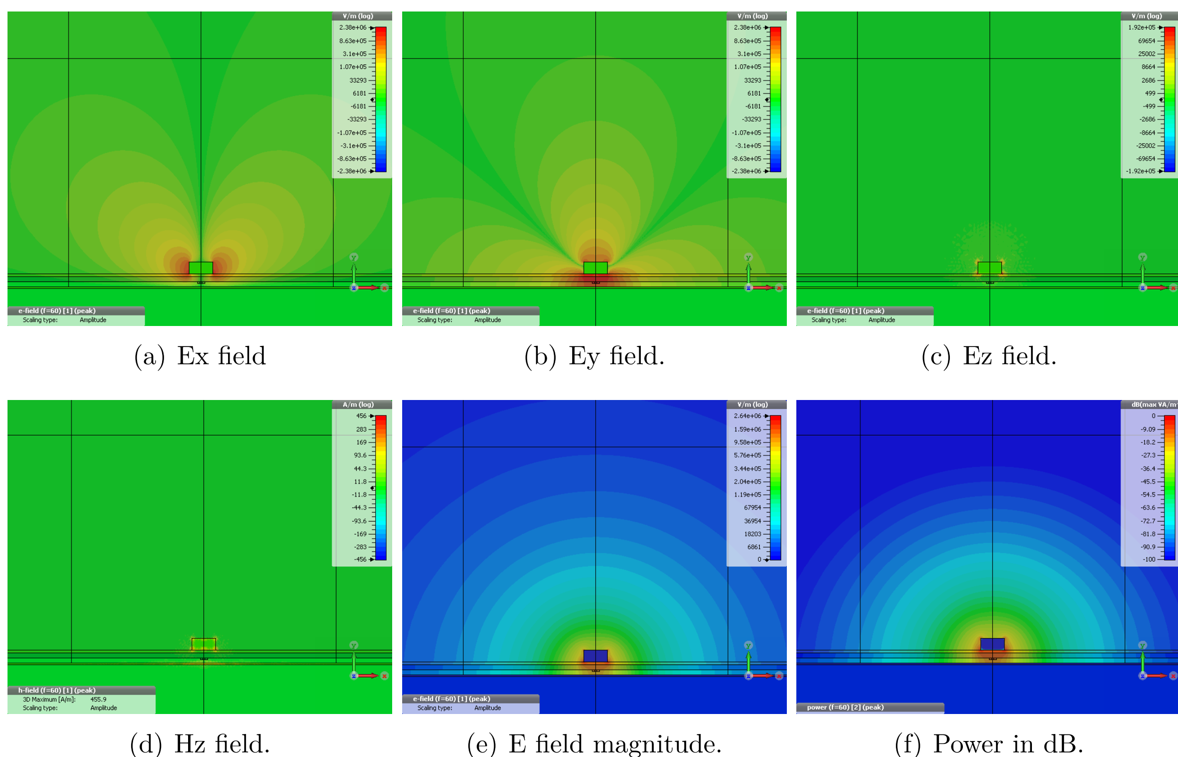

(a) Ex field (b) Ey field. (c) Ez field.

(d) Hz field. (e) E field magnitude. (f) Power in dB.

Figure 3.8: Modal analysis of the Microstrip line in one of the active arms of the TFPS modulator.

From the modal study, we calculated the line impedance (Z_{line}), effective

permittivity (ϵ_{eff}) and Loss constant (α), which are shown in Figure 3.9.

We calculated the s-parameters for various straight active region lengths L_{active} as shown in Figure 3.10. For the LX8242 Gigoptix modulator ($L_{active} = 9$ mm) we got insertion loss of -3 dB at 17 GHz from Fig. 3.10(a) and return loss is less than -25 dB.

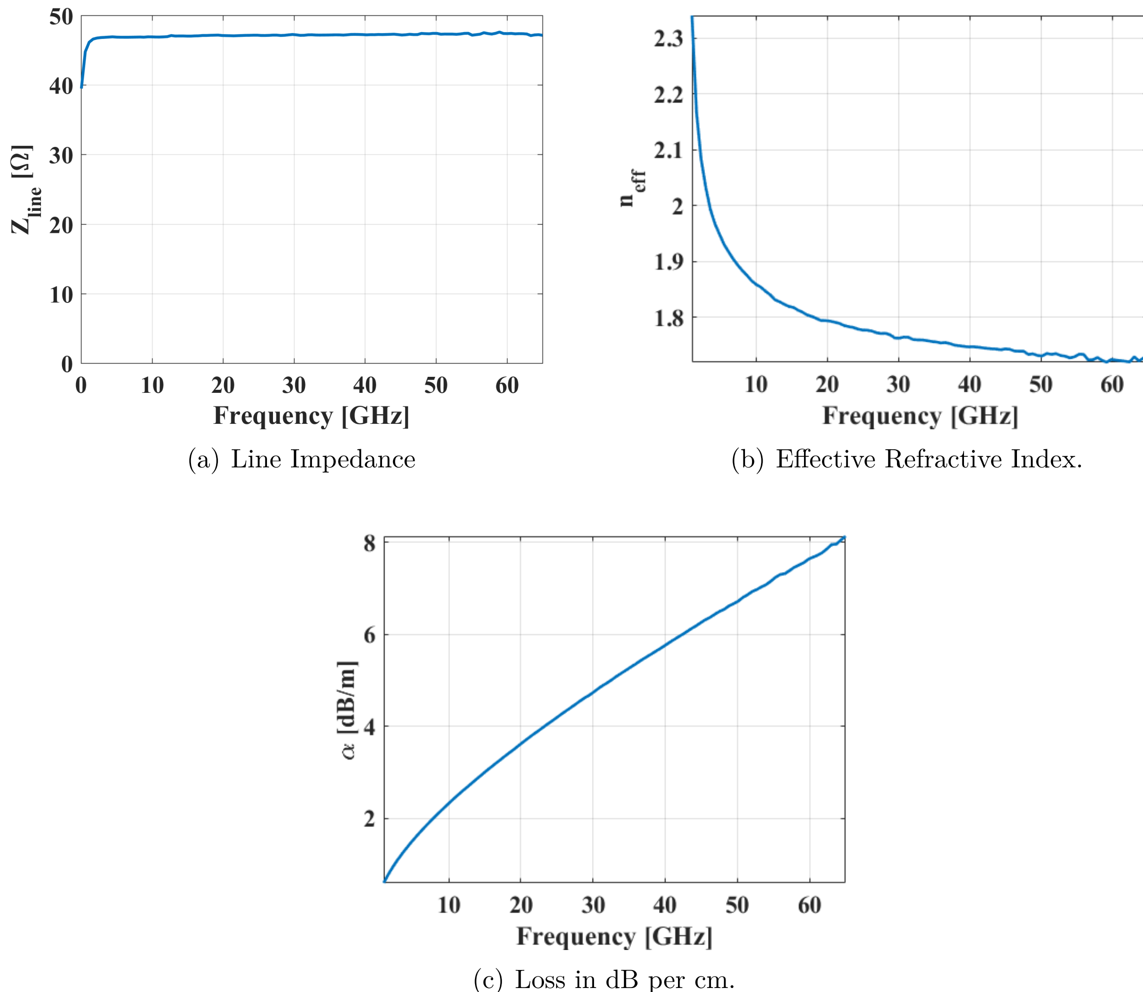

(a) Line Impedance

(b) Effective Refractive Index.

(c) Loss in dB per cm.

Figure 3.9: Modal analysis results of the polymer microstrip QTEM mode.

Microstrip bending

To minimize the footprint, it is important to design the smallest possible bend transmission line (see Fig. 3.6) without limiting the electric band. As the mode is converted from a coplanar waveguide (CPW) mode to a microstrip (MS) mode, the bending has the geometry of a MS and is depicted in Figure 3.11(a).

The material setup corresponds to the transversal section shown in Figure 3.1, minus the polymer waveguide core, as there is no poled region before reaching the active section of the TFPS modulator. Thus, B74-APC materials is unpoled and only a $h_{apc} = 2.5\mu m$ slab.

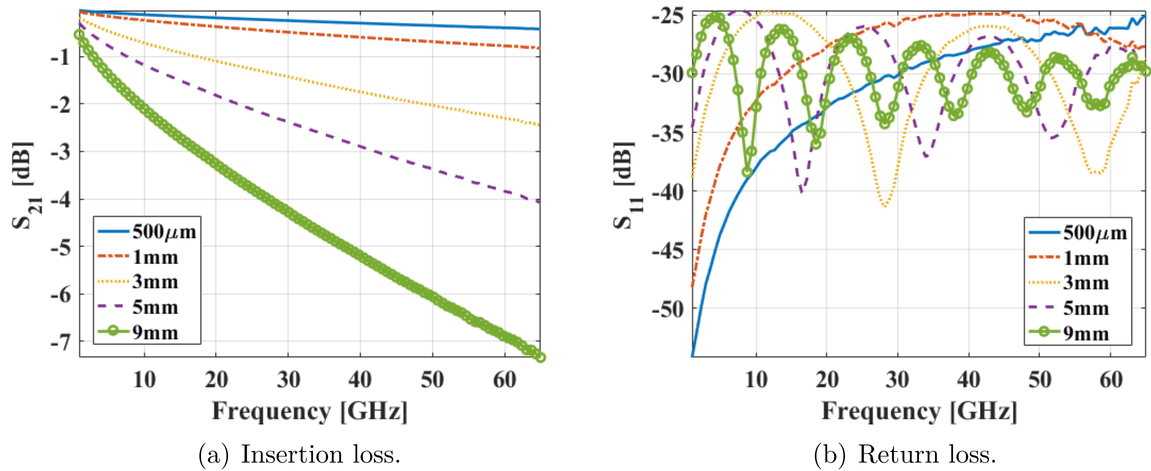

(a) Insertion loss. (b) Return loss.

Figure 3.10: S-parameters of the active region on a TFPS modulator. Length varies from $L_{active} = 500\mu$m to $L_{active} = 9$ mm.

By performing electromagnetic FEM simulation with a total of 485354 mesh elements, the resultant electric field distribution in dB is shown in Figures 3.11(b) and 3.11(c), when the bending radius (R_b) is $100\mu m$ and $50\mu m$, respectively.

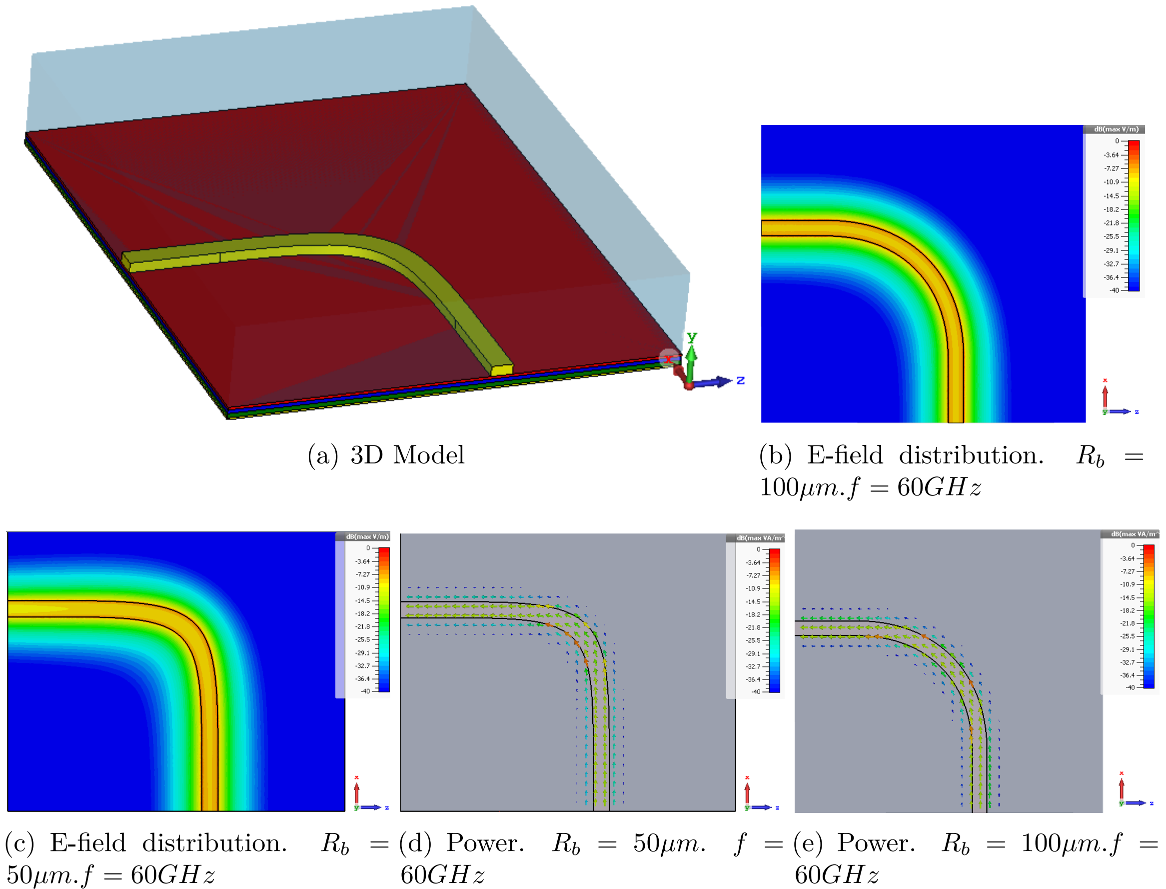

(a) 3D Model

(b) E-field distribution. $R_b = 100\mu m.f = 60GHz$

(c) E-field distribution. $R_b = 50\mu m.f = 60GHz$

(d) Power. $R_b = 50\mu m.\ f = 60GHz$

(e) Power. $R_b = 100\mu m.f = 60GHz$

Figure 3.11: Microstrip bending simulation model of the TFPS modulator. Trace width is $12\mu m$.

Figure 3.12(a) shows losses due to various bending radii. When $R_b = 100\mu m$ (see Fig. 3.11(b)) the loss is less than $0.15dB$ at $f = 65GHz$, when R_b decreases the band drops more significantly towards higher frequencies as part of the power is radiated from the TL due to the abrupt change in the propagation direction (compare Fig. 3.11(d) with Fig. 3.11(e)).

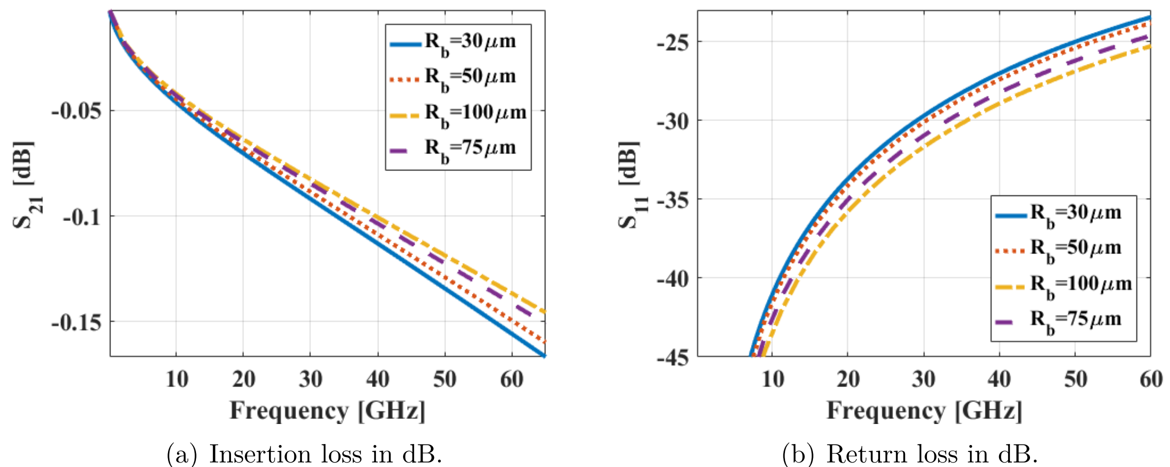

(a) Insertion loss in dB.

(b) Return loss in dB.

Figure 3.12: S-parameters of the bending microstrip in the TFPS modulator technology.

CPW to Microtrip mode converter

Direct probe feeding (50Ω) and measuring of the electric paths of our chip is done through a coplanar waveguide structure. Whilst the active region is a microstrip transmission line, a low-loss compact converter from a QTEM mode propagating in a CPW to a QTEM in a microstrip (3.3(d)) is required to improve the electric band of the system.

Figure 3.13 shows a quadrature configuration input. There are four ports and each of them consists of a coplanar waveguide at the input that is adiabatically converted to a microstrip geometry along z direction. Yellow color represents top gold layers and orange colors represent bottom gold layer. Bottom and top gold layers suffer an adiabatic variation until the bottom layer turns into an uniform film (see Fig. 3.14) and the top gold layer turns into a microstrip trace. Both metallic layers are interconnected by epoxy-filled vias. Velocity matching layer is only deposited on top of the microstrip line.

The four adjacent coplanar transmission lines in Figure 3.13 work as input ports for each electric path on top of each Mach-Zehnder modulator arm (a single MZ is depicted in 3.6), each arm has its own electrical microstrip path. A single transition from coplanar to microstrip corresponding to a single MZ arm will be analyzed. The electric field distribution is shown in Figure 3.15(a). The power flow depicted in Figure 3.15(b) clearly shows the conversion from a super mode QTEM in a CPW into two segments to a

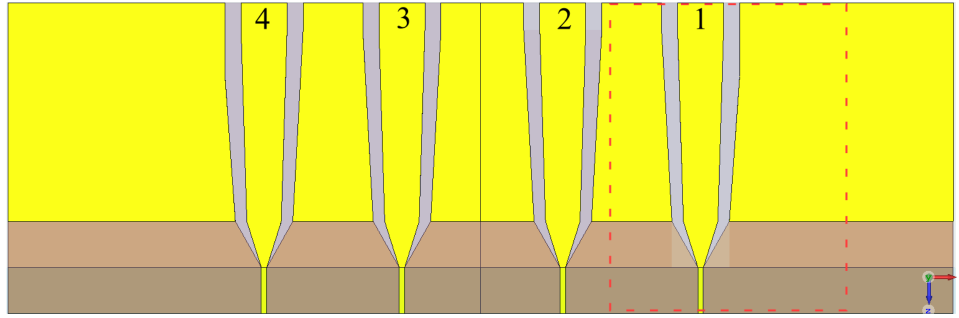

Figure 3.13: Electrical signal input ports of the TFPS modulator. Each electrode over a Mach-Zehnder modulator arm is fed by a port (1, 2, 3 or 4). Dashed box encloses our simulation domain. Gold layers are shown.

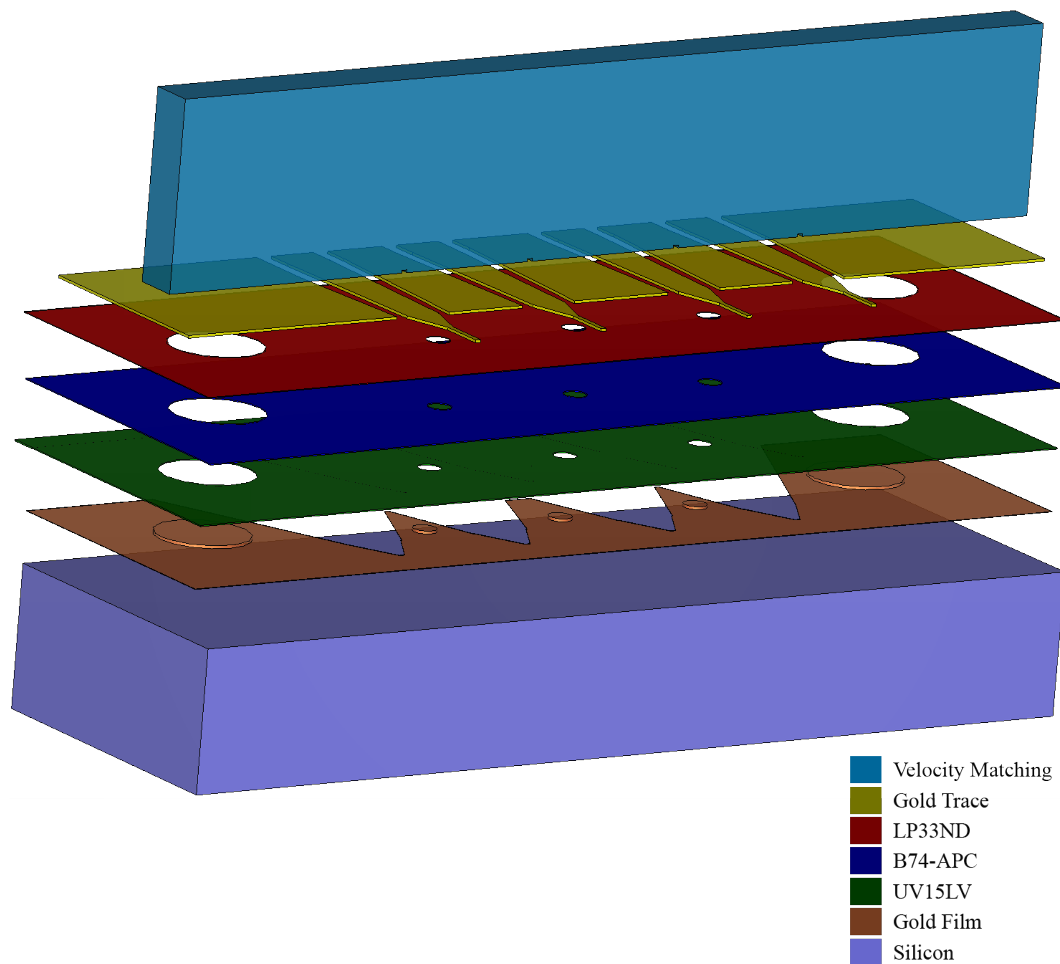

Figure 3.14: Fabrication layers of the CPW to microstrip converter structure (CPW launch). Velocity matching layer is deposited only on top of the microstrip.

single mode in the microstrip transmission line.

The electric path in Figure 3.6 keeps its 50Ω along the entire path, from the input to the termination pads. Based on this architecture, the S-parameters of the input are shown in Figure 3.16. Maximum loss is at 55GHz, −0.59dB, while reflection loss is bellow −23dB in the whole band.

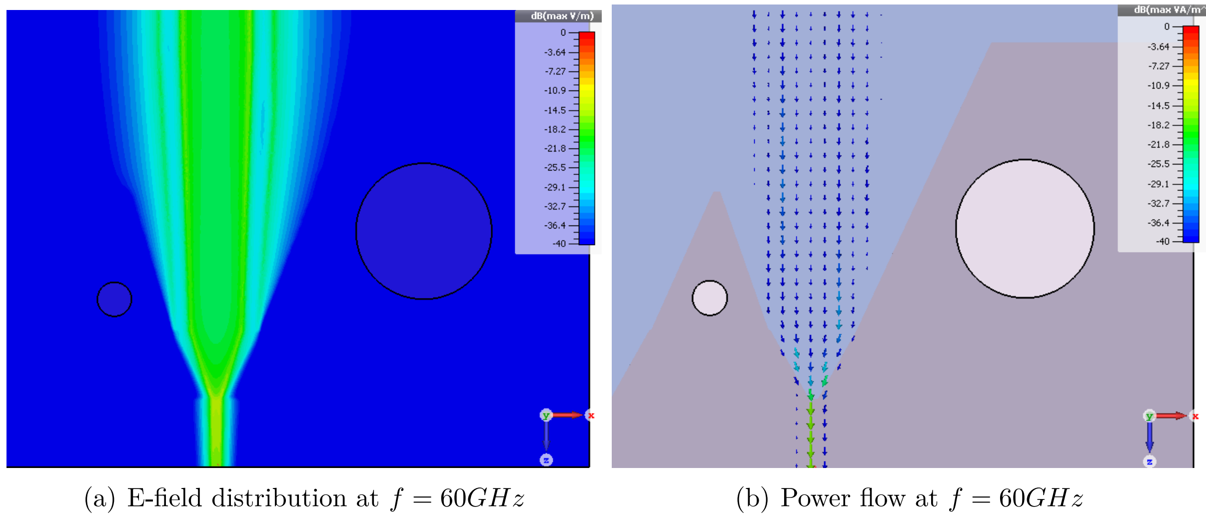

(a) E-field distribution at $f = 60GHz$ (b) Power flow at $f = 60GHz$

Figure 3.15: Electrical field distribution and Power flow of the input converter of the LX8242 modulator.

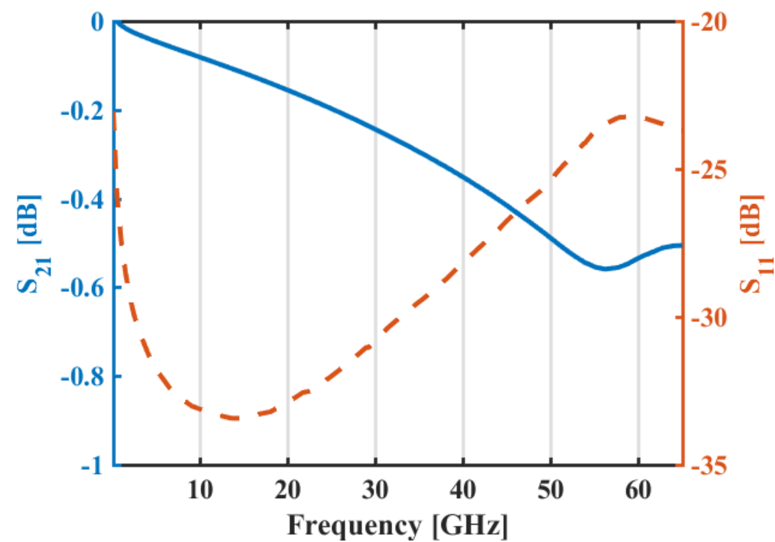

Figure 3.16: S-parameters of the input CPW to microstrip mode transformer. LX8242 polymer modulator.

Termination

Termination is the polymer modulator's end of electric path. The geometry used for the Termination CPW in Figure 3.7 is the same as the coplanar input. The structure is soldered to a 50 Ω resistor for impedance matching.

Electrical Band

The electrical path that will influence the final electrooptical band is calculated until the Active region (see Fig. 3.7). As seen in this section, the MZ arm's length is the primary source of electrical loss according to Figure 3.10(a).

If the length to achieve a half-wave phase shift on our modulator were 9 mm as in the Gigoptix/BrPhotonics commercial modulator LX8242, the RF signal loss would be governed mainly by the insertion loss of the active region (shown in Fig. 3.10(a)). The total loss of the RF path can be obtained by cascading the scattering parameters of each simulation block. The result of this cascading is 15.7 GHz at -3 dB from the coplanar input to the end of the active region.

3.3 Electrooptical properties

3.3.1 Half-wave Voltage (V_π)

To achieve intensity or phase modulation on a Mach-Zehnder architecture, an amount of voltage enough to shift one arm half-wave (or π phase) is needed. The half-wave voltage value is given by [20]:

$$V_\pi = \frac{\lambda_0}{2\Gamma L} \tag{3.5}$$

where Γ is the overlap integral between optical and electrical transversal electric fields:

$$\Gamma = \frac{1}{V_0} \frac{\int\int \frac{1}{2} n_{eff}^2 r_{33,t} E_{m,t} \left|E_{o,t}\right|^2}{\int\int \left|E_{o,t}\right|^2} \tag{3.6}$$

where n_{eff} is the effective refractive index, r_{33} is the electrooptic constant in pm/V. Also note that in the overlap integral expression we use E_o as transversal optical electric field and E_m, transversal RF electrical field.

Optical and RF field simulations were obtained using a two-dimensional cross-section in Comsol Multiphysics 5.2 and the results were processed from the sections above. By using $r_{33} = 82$ pm/V and an active region of 9 mm we obtained a theoretical value for the half-wave voltage: $V_\pi = 2.3$ V.

3.3.2 Electrooptic bandwidth

The electrooptic bandwidth is measured at the 70.7% of the electric field amplitude maximum value (-3 dB). Let us consider a phase modulation on a single Mach-Zehnder polymer modulator. The electric field at the output is given by

$$E_{out}(t) = E_{in}(t) e^{j\Delta\phi m(t)}, \tag{3.7}$$

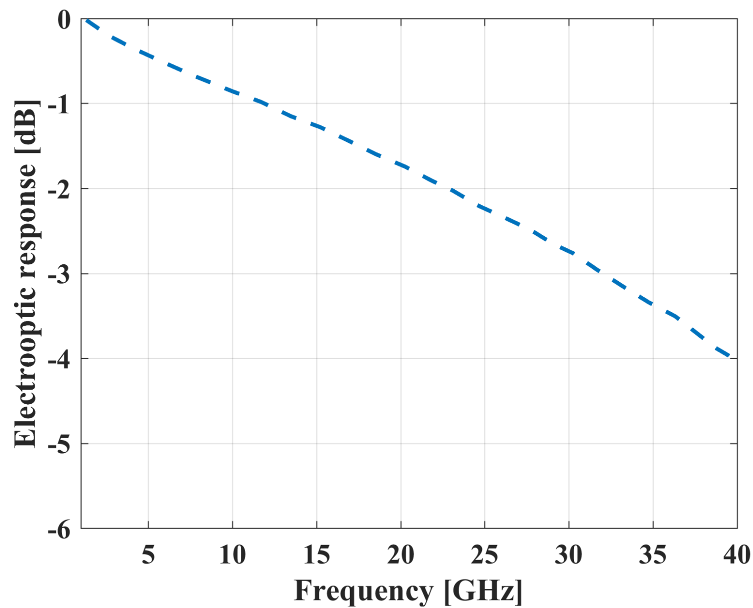

Figure 3.17: Electrooptic response of the 9mm MZ polymer modulator.

where E_{in} and E_{out} are the input and output optical electric field, respectively. The phase deviation is given by $\Delta\phi$ and $m(f_m)$ is the electrooptic response function [102].

$$m(f_m) = e^{-\alpha_m(f_m)L/2}\sqrt{\frac{\sinh^2(\alpha_m L/2) + \sinh^2(k_m \delta L/2)}{(\alpha_m L/2)^2 + (k\delta L/2)^2}} \tag{3.8}$$

where $k_m = (2\pi n_m)/\lambda_m$ is the wave number, $\delta = 1 - n_0/n_m$ is the relative index mismatch between RF effective index (n_m) and optical effective index (n_0), L is length and α_m is the RF attenuation constant.

Figure 3.17 shows the electrooptical transmission as a function of frequency of a 9mm arm MZ polymer modulator. The -3 dB level is at 31.5 GHz with respect to the response at 1 GHz.

3.4 Bias circuits

To achieve two types of modulation, say phase and intensity, on a single MZ structure, one of the arms of the MZ interferometer should be phase shifted. This condition can be achieved by elongating only one arm or by using bias circuits that introduce a thermal effect that inserts a phase shift.

Bias circuits are designed to introduce a πrad phase shift between the arms of the Mach-Zehnder structure.

Electro-thermal and thermo-optical effects will allow us to calculate the required power to achieve a π rad phase deviation between two arms of the MZ polymer modulators.

Figure 3.18 shows the phase shift in the two arms. The arm that has the

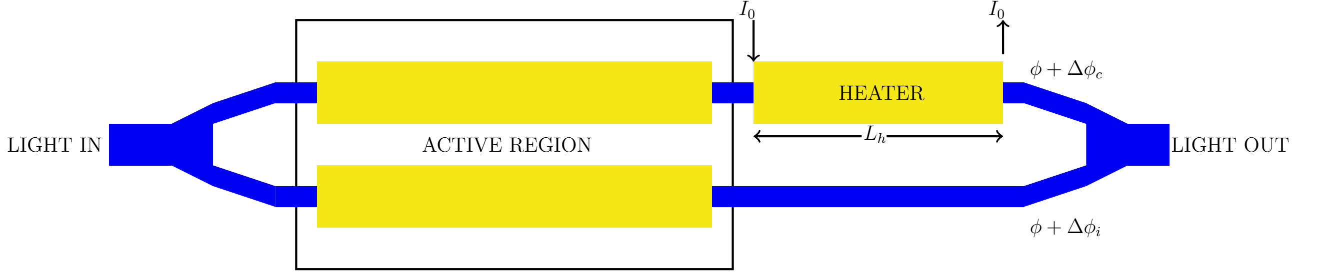

Figure 3.18: Bias circuit (heater) on a MZ polymer modulator.

electrode (heater) shifts $\phi+\Delta\phi_c$ while the other arm has an interference phase shift $\phi+\Delta\phi_i$ due to the temperature rise. The actual phase shift between arms is $\Delta\phi_h = \Delta\phi_c - \Delta\phi_i$. The aim of this section is to find the length L_h that makes $\Delta\phi_h = \pi$.

3.4.1 Thermo-optic effect

The heat transfer model is defined by an elliptic partial differential equation for the temperature T:

$$\begin{aligned} \rho C\frac{\partial T}{\partial t} + \nabla \cdot \overrightarrow{q} &= Q \\ \overrightarrow{q} &= -\kappa \nabla T \end{aligned} \tag{3.9}$$

where $\overrightarrow{q}$ is the conductive heat flux, ρ is the material's density, Q is a heat source, C is the specific heat capacity and κ is the thermal conductivity.

Dirichlet boundary conditions imposed to the model include $T = T_0$ which is the temperature induced by the electric current in the transversal section of the heater (see Fig. 3.19) and the ambient temperature $T_1 = 293.15$ K at the bottom of the structure. Silicon substrate is 625μm thick. All other boundaries are considered Neumann conditions $(-\vec{n} \cdot \vec{q} = 0)$ which are considered as outflowing or open boundaries.

Polymer stack's heat capacity is 1200 J/(Kg.K), silicon heat capacity is 700 J/(kg.K) and is 1005 J/(Kg.K). Thermal conductivity of the polymer stack is 0.15 W/(m.K), silicon is 124 W/(m.K) which can be addressed as the system's heat-sink. Polymers' density is around 1200 kg/m^3 and silicon's is 2329 kg/m^3.

To find T_0, we must first consider the thermo-optical effect that is governed by the thermo-optic coefficient, which gives a refractive index that is temperature dependent: $n(T) = n_0 + \frac{\mathrm{dn}}{\mathrm{dT}}\Delta T$, where n_0 is the refractive index of each polymer layer at 293.15 K, ΔT is the variation from this temperature and $\frac{\mathrm{dn}}{\mathrm{dT}} = 1 \times 10^{-4}$ is the thermo-optic coefficient of the polymer stack shown in Fig. 3.20 [103].

Temperature distribution is depicted in Figure 3.20. The required electrode

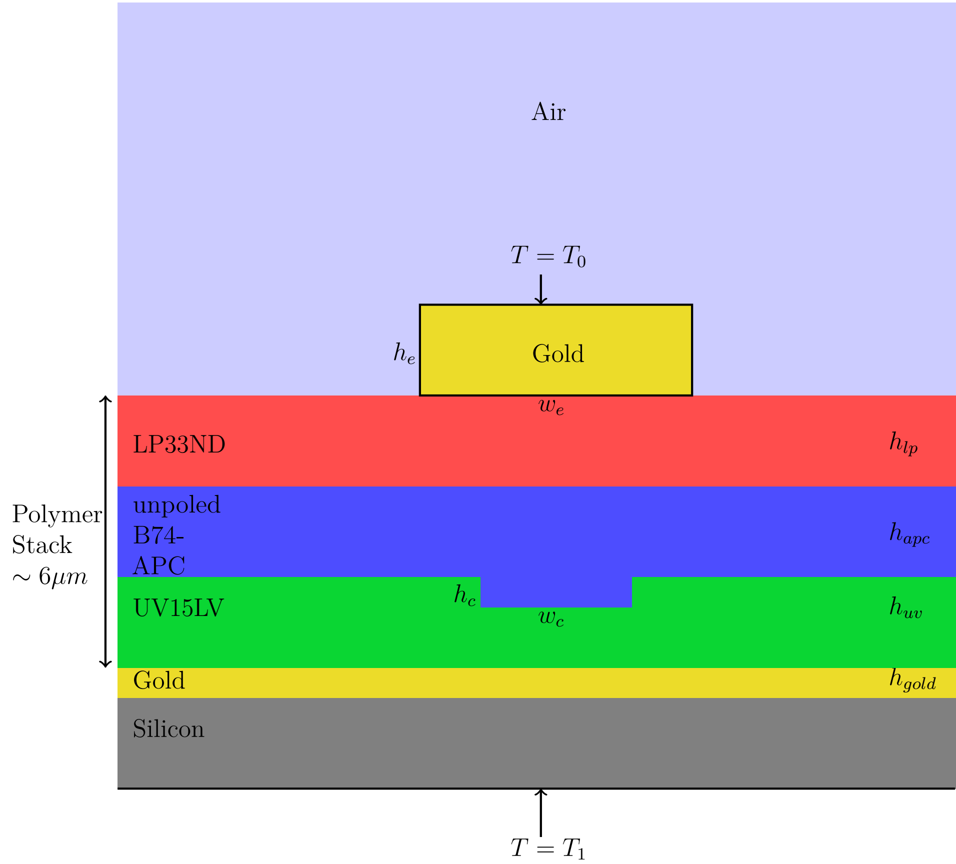

Figure 3.19: Simulation environment of the thermo-optical effect. The polymer stack is represented as a thermal unit with the same Thermal coefficient.

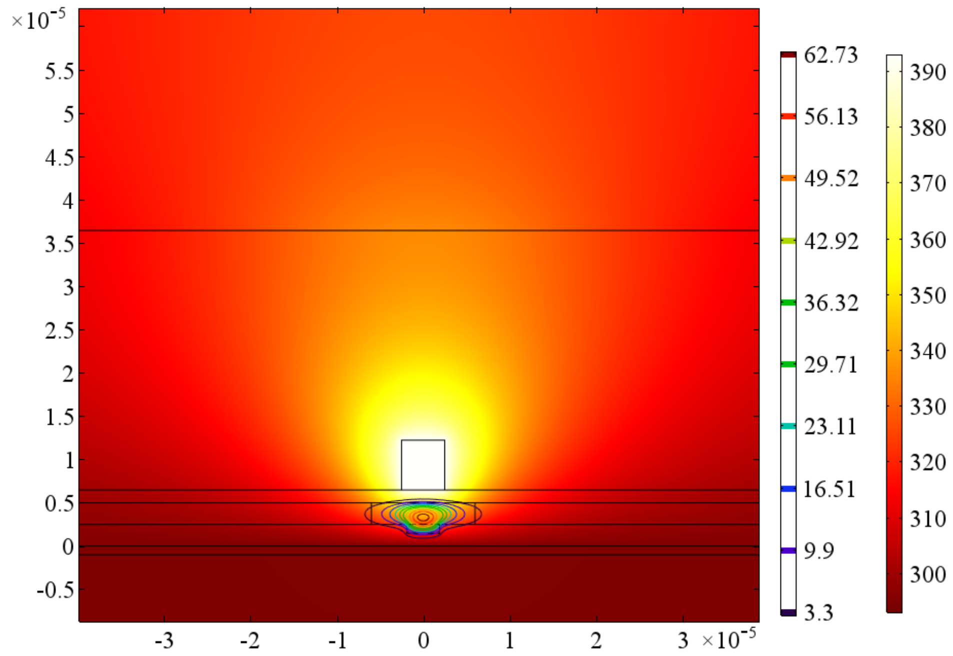

Figure 3.20: Heat distribution of T(surface) and first TM mode's electric field distribution of the non poled polymer waveguide (contour). Axis units are meters.

temperature (T_0) to get an accumulated phase shift $\Delta\phi_c = \pi$rad is detailed in Table 3.4. Note that the accumulated phase shift was calculated over the heater length $L_h = 1600$ for this stage of analysis. Accumulated Phase is $\Delta\phi_c \sim \pi$ when $T_0 = 303.75$ K. For this value, from the numerical calculations that led to Figure 3.21, we calculated the phase shift interference on the second MZ arm $\Delta\phi_i = 0.23$rad (distances between MZ arms is 50μm). Total accumulated phase shift is $\Delta\phi_h = 2.911$rad. Figure 3.22 shows the accumulated phase as a function of temperature. Note that the numerical simulation was performed by keeping the distance between arms constant (see fig. 3.18). Non-linearities may be found if the heater electrode length is placed on the bending waveguide towards the MZ end.

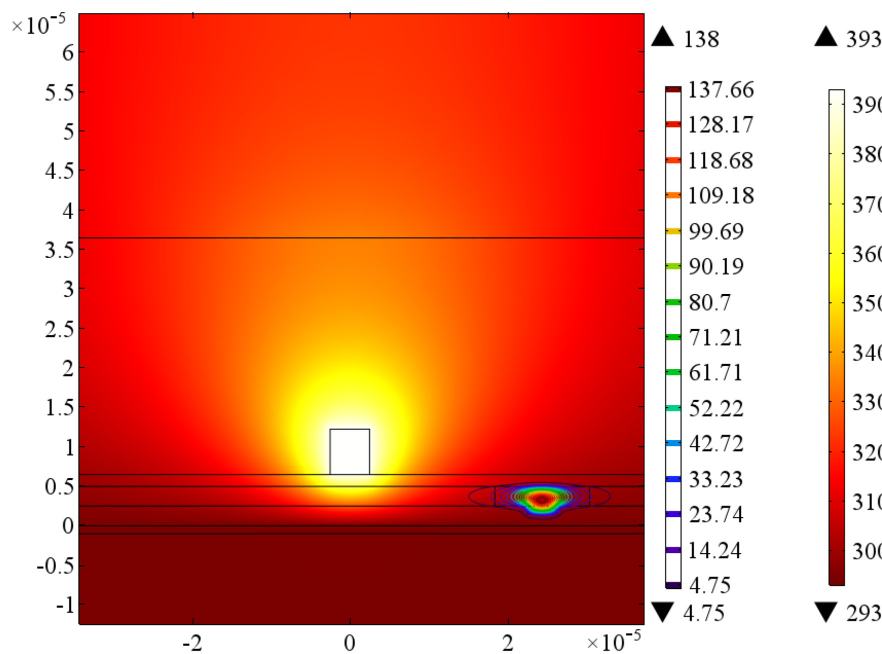

Figure 3.21: Heat distribution of T(surface) and first TM mode;s electric field distribution of the opposite MZ arm polymer waveguide (contour). Axis units are meters.

T_0 (K)	Prop. const. β (10^6rad/m)	Phase (rad)	$\Delta\phi_c$(rad)	Av. T (K)	ΔT [K]
293.15	6.70520	11097.1060	0	293.150	0
295.8	6.70570	11097.9335	0.8275	294.320	1.170
298.45	6.70610	11098.5955	1.4895	295.500	2.350
301.1	6.70660	11099.4230	2.3170	296.670	3.520
303.75	6.70710	11100.2505	3.1445	297.840	4.690
306.4	6.70760	11101.0780	3.9720	299.010	5.860

Table 3.4: Accumulated phase shift over L_h in one of the arms of the MZ polymer modulator. ($\lambda = 1550$ nm).

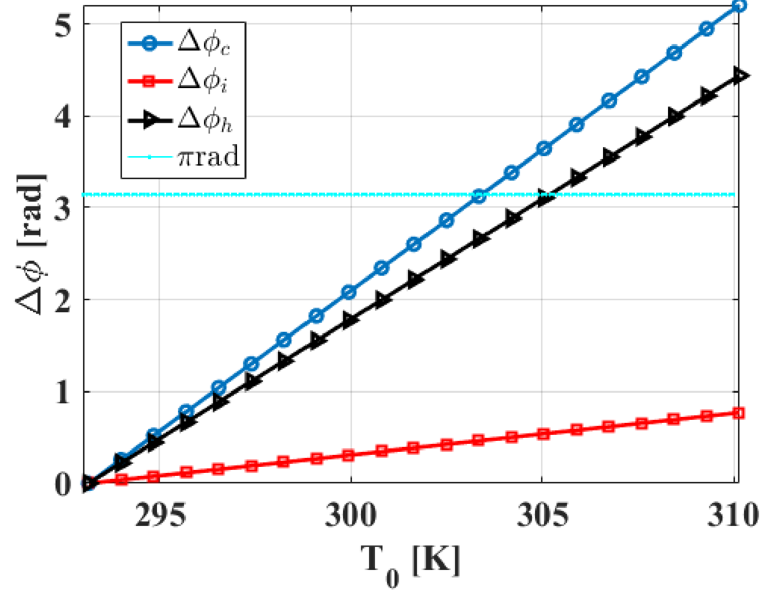

Figure 3.22: Accumulated phase shift induced by the thermo-optical effect in the polymer modulator chip. $\Delta\phi_c$ corresponds to the set up in Figure 3.20 and $\Delta\phi_i$ to Figure 3.21. $\Delta\phi_h = \Delta\phi_c - \Delta\phi_i$ is the real phase shift between MZ arms.

3.4.2 Electro-thermal effect

To achieve the temperature required in the electrode (T_0), a current is induced creating the electro-thermal effect or Joule effect. An accurate power consumption estimation (eq. 3.10) to achieve a πrad was presented in a variable optical attenuator from [104] and then applied to polymer modulators in [45]. Power is estimated as:

$$P = \kappa \frac{2\lambda w_e}{\gamma d \frac{\mathrm{dn}}{\mathrm{dT}}} \tag{3.10}$$

where κ is the polymer stack thermal conductivity, d is the polymer stack thickness and $\frac{\mathrm{dn}}{\mathrm{dT}}$ already has been defined as the polymer thermo-optic coefficient, γ is the thermal efficiency, and the heater width $w_e = 5$ μm. A typical thermal efficiency is around 0.4 to 0.5.

By using (3.10) we can infer that if w_e increases, the power to maintain a π phase shift also increases. The best option is to choose the tiniest w_e possible without it being difficult to align with the 3.8 μm wide polymer waveguide core. Around 5 μm.

A safe maximum current density of the gold path based on its electrical conductivity is around 1 mA/μm^2. For this purpose, and knowing that $w_e = 5$ μm, we can make $L_h = 1600$ μm. With these parameters we performed a numerical simulation of the Joule effect in our device by using Comsotl Multiphysics [100]. The results are depicted in Figure 3.23. Note that to maintain a πrad phase, according to Fig. 3.22, $T_0 = 305$K. From that we need 0.074 A or $P = 0.014$ W.

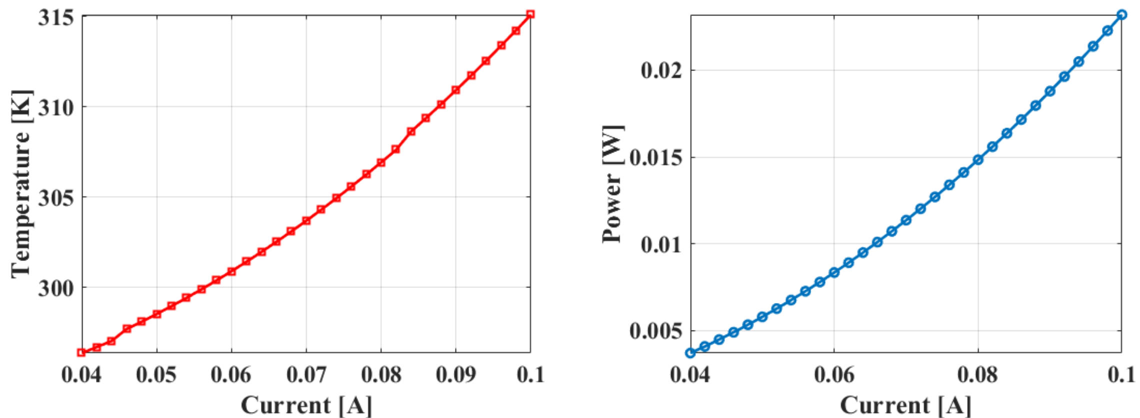

(a) Temperature of the Electrode (T_0) as a function of Current

(b) Temperature of the Electrode (T_0) as a function of Power

Figure 3.23: Numerical simulation results of the polymer modulator heater to maintain a πphase between MZ arms.

Note that there is good agreement between the model in (3.10) and the numerical simulation for the $\Delta\phi_c$ required temperature which is 303 K, hence 0.068 A calculated from Fig. 3.23, and 0.067 A approximated by the equation. The approximate model does not consider the phase shift created by the temperature interference in the second MZ arm.

3.4.3 Measurements

Let us apply the EO polymer MZ modulator bias circuits methodology to the LX8901 modulator by BrPhotonics. This modulator has a heater electrode length of 2000μm and a transversal area of $5.5\mu m \times 5\mu m$, a polymer stack of $5.9\mu m$ and the distance between MZ arms remains $50\mu m$ throughout the whole length.

By performing the thermo-optic simulation to this geometry, we found out the phase shift between the MZ arms ($\Delta\phi_c - \Delta\phi_i$) in Figure 3.24. The electrode temperature T_0 for a phase shift of π is 301.39K, which implies a $\Delta T_0 = 8.51$K when compared to room temperature.

After performing the electro-thermal simulation, we found that a current of 59.5mA is needed to achieve the desired electrode temperature shift as depicted in Fig. 3.25.

The setup used to perform the bias measurements is depicted in Figure 3.26. Light input is given by a laser and read by a power meter, while DC current (I_0) is injected into the bias circuit through the heater pads. This bias current will case the phase deviation between the MZ arms $\Delta\phi_c - \Delta\phi_i$ as predicted by the simulation. We are also predicting an slight phase mismatch attributed to a possible small difference between MZ arms length which we are calling $\Delta\phi_{dev}$.

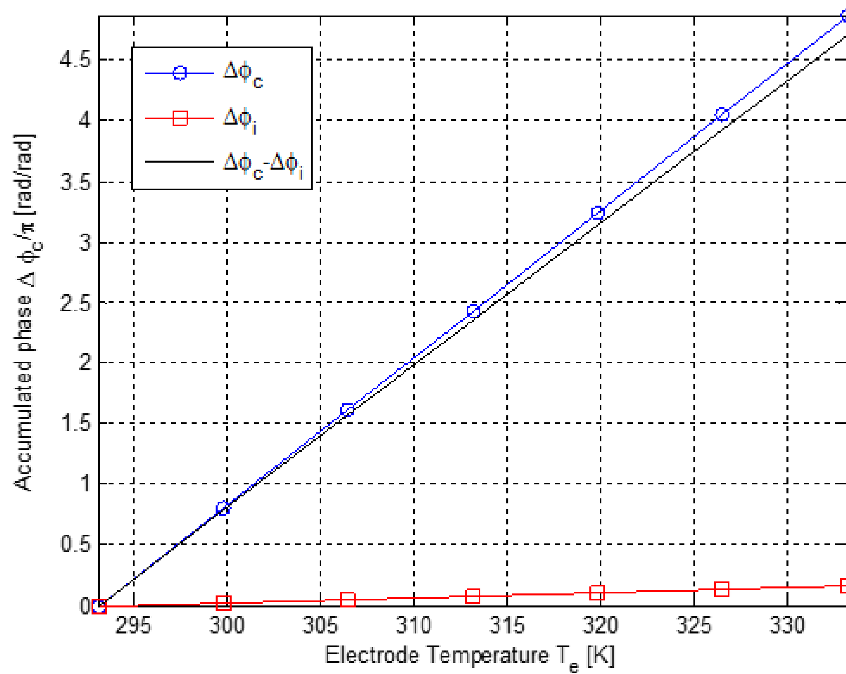

Figure 3.24: Thermo-optic simulation result of an LX8901 Eo polymer modulator. Phase Shift on each MZ arm ($\Delta\phi_c$ and $\Delta\phi_i$) as a function of the heater temperature.

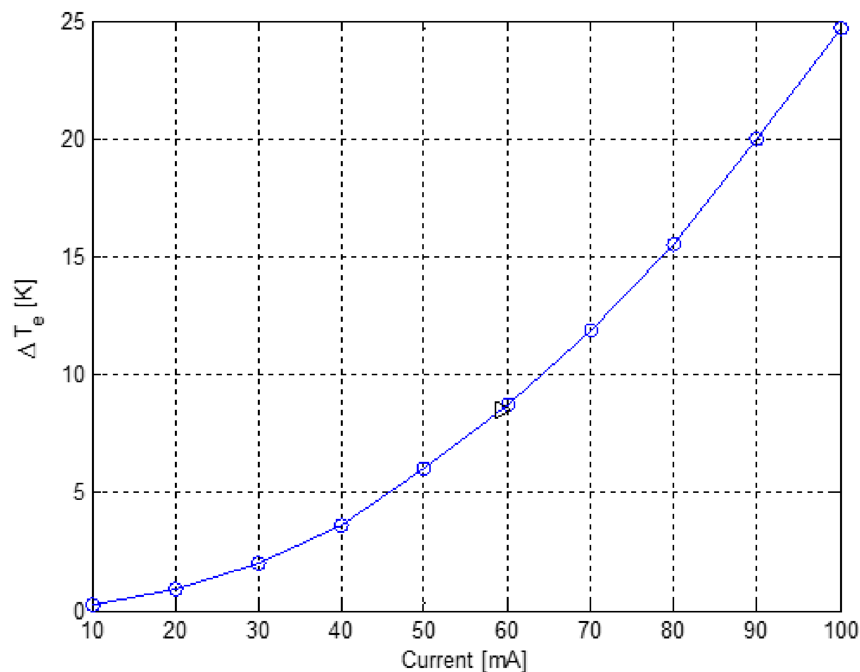

Figure 3.25: Electro-optic simulation result. Current sweep applied to the bias heater circuit length cases the electrode temperature to vary when compared with room temperature (ΔT_0). Triangle marker represents the current needed to achieve $\Delta T_0 = 8.51$K.

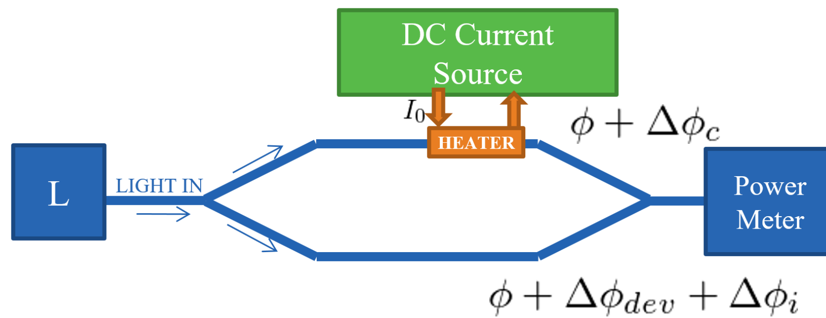

Figure 3.26: Heater bias measurement setup.

A current sweep was injected into the bias circuit while the optical power was measured (see Fig. 3.27). The first valley, which represents the first π rad deviation between MZ arms appears around 61 mA.

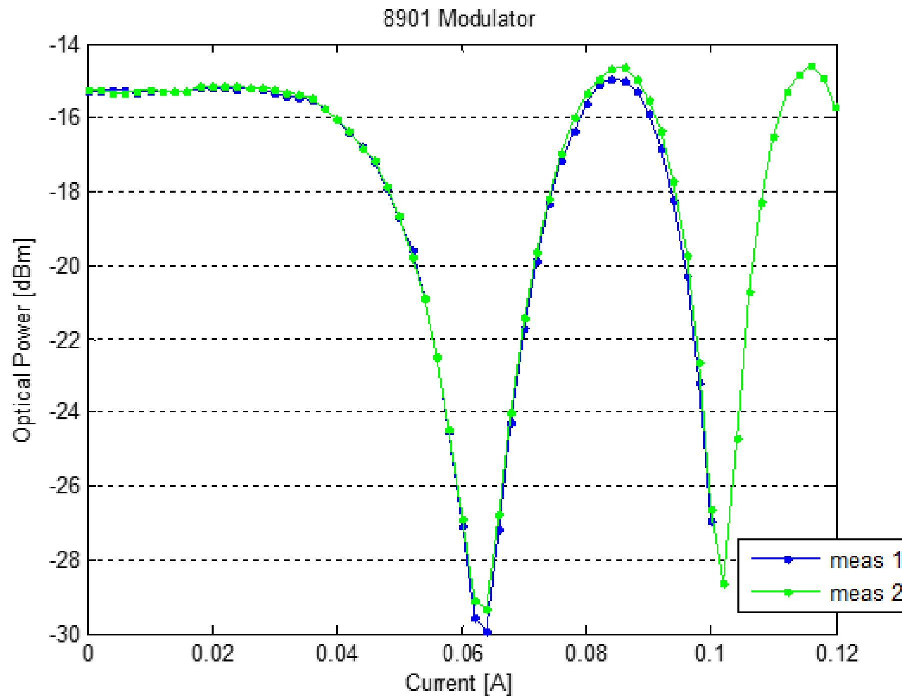

Figure 3.27: Optical power measured versus injected current (I_0) to the bias heater circuit of an LX8901 EO polymer modulator.

3.5 Summary

This chapter presented a basic polymer electrooptic modulator physical architecture. The use of APC substrate as a host for the chromophore molecules is presented. Using previous material characterization data in the 1550μm wavelength and in the DC to microwave band we simulated optical waveguides and the microstrip transmission line to perform the electrooptic effect. After calculating the electrical band of the whole electrode

system we calculated the electrooptic bandwidth and thus got an idea of the modulator's efficiency. V_π was also calculated. Thermo-optic and electro-thermal simulations were performed to improve the literature's modeling of the power needed to feed a π rad bias circuit, which resulted in a contribution to previous approximation equation.

Chapter 4

Transmitter optical sub-assemblies: Electrical Interconnects

This chapter presents a compact and wide-band RF path design as a part of the hybrid platform transmitter optical sub-assembly for polymer electrooptic modulators.

As new standards become increasingly demanding, low loss, wide band and low cost are even more important to enable RF interconnects. This chapter will be divided into an introductory section which will show the design methodology for the RF interconnects, section 4.2 will show some industry standards for various network applications, section 4.3 shows the development of our proposed electrical interconnects, section 4.4 shows a system overview of all the single devices integrated on a block cascading platform, lastly, section 4.5 shows the effects of the proposed RF interconnects on the TOSA electrooptical response.

4.1 Design Methodology

Our contribution to the design methodology of RF interconnects for transmitter optical sub-assemblies applied to long-haul data center interconnects, or even non-coherent metropolitan networks is the inclusion of the Thin-Film Polymer on Silicon (TFPS) chip analysis (previously discussed in Chapter 3) into the design flow as shown in Fig. 4.1.

The input blocks (orange) section are the general requirements for each of the process blocks (purple). To determine the system requirements, we considered commercial Thin-film polymer on silicon chip optical and RF paths, the general packaging industry needs (previously discussed in the introductory chapter of this thesis) and high-performance, wide-band RF interconnects state of the art of each device. The main system requirements include: The practicability, fabrication capacity to finally produce series-production ready devices, high performance, wide electrooptic band, low return loss. Numerical values for these requirements are discussed in section 4.2.

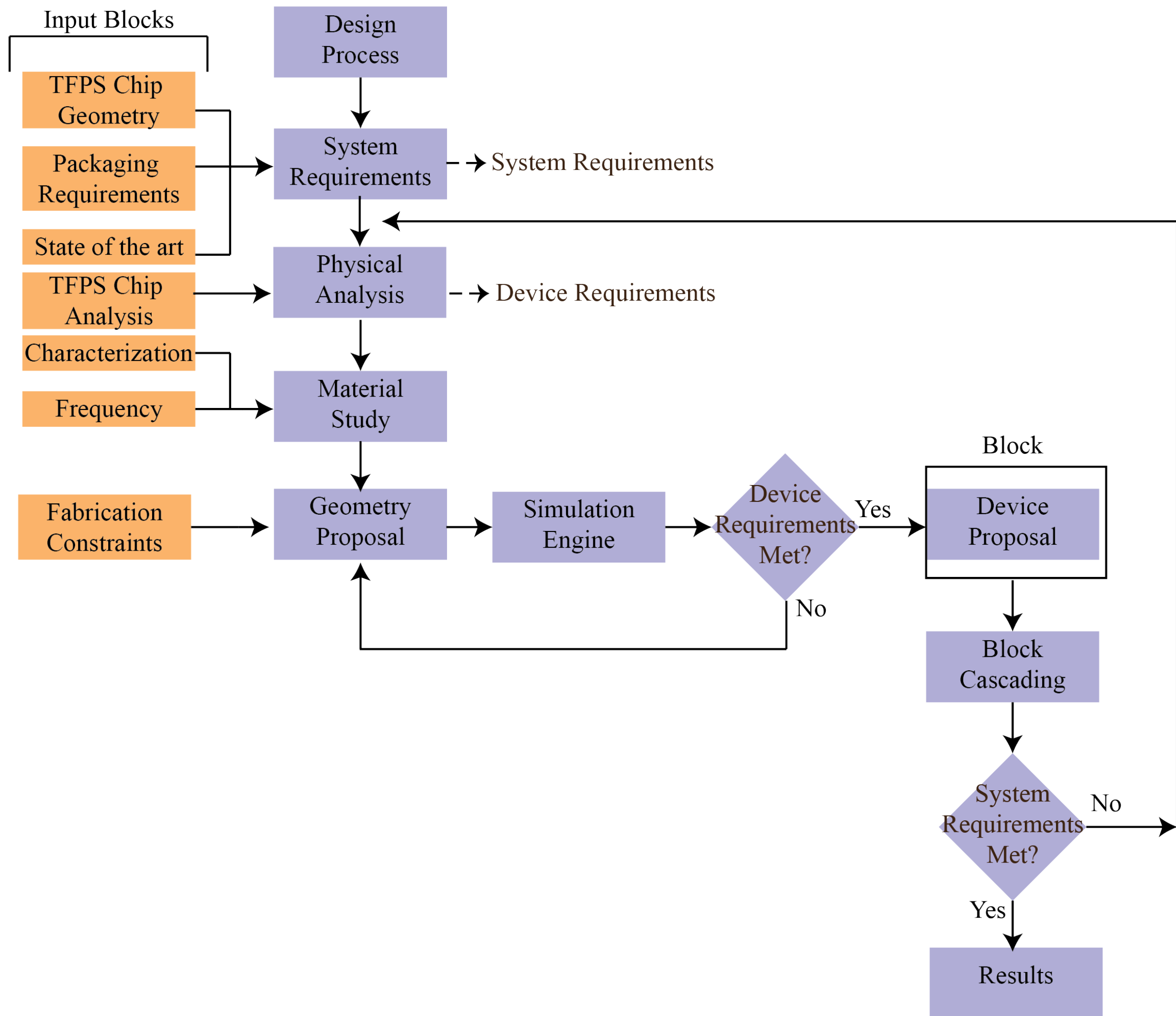

Figure 4.1: Schematic of the design process for the RF paths. Input blocks are colored orange, while active process blocks are violet.

The transmission lines analysis in the TFPS chip (fourth orange block) was thoroughly studied in Chapter 3 and it will be considered for the physical analysis proposal which enables us to list the RF devices requirements that will make our design meet the system requirements. In general lines, a single device set of requirements include: wide band, low loss up to 65 GHz, small footprint and interconnect devices size matching (such as integrated circuit pads and pins).

The material study includes the polymers characterization of their dielectric properties which are dependent on frequency. This study was provided by BrPhotonics and will be detailed in section 4.3.1. A first geometry can only be proposed after considering current thin-film manufacturer constraints [105]. The proposed device's performance is theoretically evaluated by the electromagnetic simulation engine Computer Simulation Software [106], Microwave Module. If the device requirements are not met, the flux goes back to the geometry optimization and is reevaluated. Once optimized, the scattering parameters (S-Parameters) of the simulated device are considered as an operating block

which then is operated to evaluate the system goals. Once all interconnecting devices are considered, to exit the flux, the system requirements must be met.

To evaluate the system requirements (System Requirements met? block) we must calculate the electrooptic band and the return loss of the whole system. This includes the TFPS modulator transmission line analysis performed in chapter 3 physically interconnected to the packaging transmission lines and connectors.

The following section will analyze some standards for transmitter optical sub-assemblies which will be considered when evaluating the performance of the RF interconnect system at the end of the chapter.

4.2 Industry standards for optical telecommunication networks

As telecommunication traffic increases, new broad band technologies such as 100-Gbit/s Ethernet, which was standardized in 2010, became very common in telecommunications setups around the world. Bandwidth requirements are listed in this document, in order to address the following applications(extracted from [13]):

- Servers, high performance clusters, blade servers, storage area networks, network attached storage.
- Switching, routing, aggregation in data centers, internet exchanges, service provider peering points, high bandwidth applications such as video on demand and high performance computing environments.

IEEE P802.3ba 100Gb/s requirements include operating at least for 40 km on single mode fiber (SMF) with a bit error rate better than or equal to 10^{-12}. Some transmitter optical sub-assemblies (TOSA) that follow these regulation have been developed, for instance in [107], they used electroabsorption modulators integrated with four-lane distributed-feedback lasers (EADFB).

A recent amendment to the P802.3 standard is currently being discussed, to achieve 200 to 400Gb/s Ethernet [108], IEEE P802.3bs. The objectives now include appropriate support for optical transport network over 2km or 10km of SMF. Key applications of this new standard include: cloud-scale data centers, internet exchanges, co-location services, wireless infrastructure, service provider and operator networks, and video distribution infrastructure. Transmitter and receiver requirements and optical modulation amplitudes (OMA) according to P802.3bs are depicted in table 4.1.

There are efforts to find an interesting architecture to fulfill the P802.3bs as the one shown in [109], with 8×28.125GBd DWDM PAM-4 signal transmission over standard SMF in the 1550nm transmission window. They achieved a BER of 10^{-6} for

Table 4.1: P802.3bs IEEE standard recommendations for 400Gbit/s over 2km and 10km on SMF. [108]

Description	400GBASE-FR8	400GBASE-LR8	Unit
Reach	2	10	km
Transmitter			
Signaling Rate per lane	26.6	26.6	GBd
Operating BER	2.0e-04	2.0e-4.	
OMA, per lane (max)	5.5	5.7	dBm
OMA, per lane (min)	0	0.5	dBm
Transmitter and dispersion penalty	2.0	2.2	dB
Receiver			
Signaling Rate, per lane	26.6	26.6	GBd
Receiver sensitivity per lane	-10.0	-11.8	dBm
Receiver 3dB electrical upper cutoff frequency, per lane (max)	21.0	21.0	GHz
Optical Margin			
DeMux loss	3.0	3.0	dB
Cross-talk penalty	0.3	0.3	dB
Optical margin	3.7	1.9	dB
Receiver sensitivity, per lane, post-DeMux	-13.3	-15.1	dBm
Receiver sensitivity, per lane (typical measured)	-17	-17	dBm

each channel which is enough to transmit over even longer distances than 10km. This and other advanced modulation techniques such as XQAM, together with signal processing and coding are becoming very important to increase the channel capacity and reduce BER significantly as shown in [110].

For metro networks traffic growth is usually driven by more demand of video streaming and proliferation of cloud computing, mobile data delivery, social media and more recently by machine-to-machine communication. In this scenario, the OIF has cited the constraints and challenges for 400G WDM [14]. Two sub-channels of 200Gb/s or four of 100Gb/s are proposed with a maximum transmission reach of $\sim$ 500 km and $\sim$ 2000 km, respectively. A brazilian company, BrPhotonics, together with CPqD made an effort to accomplish 200Gb/s in [39]. Using a TOSA with an EO bandwidth of 23 GHz, $V_\pi = 3.5$ V in differential mode, power dissipation of 2.5 W and narrow-line width TL (less than 100 kHz), using the TFPS modulator in [92] and comparing its performance with a commercial $LiNbO_3$ modulator. EO bandwidth penalty (about 11 GHz) was found because of the TOSA carrier board necessary to interconnect the RF signal, forcing a compensation filter in the DSP stage. This electrical bandwidth reduction, which clearly affects the EO bandwidth, will be addressed in the following section to prepare this polymer-based TOSA technology for 400Gb/s standards attendance.

Specific transmitter assemblies agreements for metro were made by the OIF

for 100G technology. Table 4.2 resumes the opto-electronic properties recommendations that we are going to meet in this chapter.

Table 4.2: OIF transmitter package implementations agreement from [44]. Optoelectronic properties.

Parameter	Unit	Min.	Typ.	Max.	Remarks
S_{21} EO Bandwidth (3dB)	GHz	20			3% smoothed, reference frequency at 1.5GHz
S_{11} Electrical Return Loss					
f<25GHz	dB	10			
25<f<32GHz		8			
V_π PRBS	V			2.5	Specified PRBS31 at 32GBd and over DC bias control range: -1.5 ... -15V
V_π LF	V			2.5	Measured at 1.5GHz
RF Impedance	Ω		50		
I/Q skew	ps			4	For each polarization component and for each tributary
Total skew	ps			10	

4.3 Electrical Interconnects

Wide electrical bandwidth and space effective RF interconnections are the pillars of any electrical RF path inside a TOSA. Figures 4.2 and 4.3 show the high speed electrical path of a TFPS modulator based transmitter optical subassembly. Z_{con} is the equivalent impedance due to a GPPO™by Corning Gilbert Inc., multipin or any connector. TL_{in} is the ceramic transmission line to convert the modulator TL to the connector mode or feeding transmission line. $Z_{s1,s2}$ are impedances due to soldering or wire/ribbon bonding. TL_{mod} is the traveling wave electrode of the modulator already discussed in Chapter 3. The electrical part of the transmitter ends with an impedance matching terminator ($Z_{terminator}$) interconnected by a TL_{out} which is a tapered transmission line.

Materials such as ceramic and laminated gold can be used to reduce losses. Interconnection with external electrical feed is done through connectors that allow for high packaging integration. This aspects will be discussed in this section.

4.3.1 Materials

Thin Film gold over ceramic is a very common high speed RF platform on behalf of its high dielectric constant and compatibility with soldering and wire bonding.

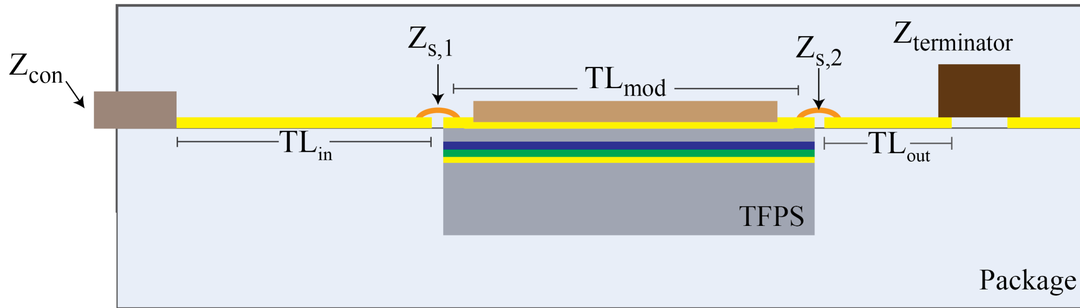

Figure 4.2: Longitudinal cut of the electrical signal path representation of a transmitter optical subassembly package including electrooptic polymer thin-film on silicon (TFPS) chip. Yellow represents metalization.

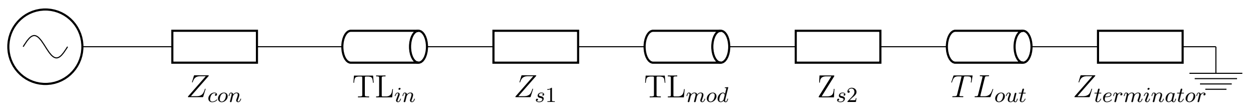

Figure 4.3: High speed electric signal path of the whole system specifying the ceramic package line (Z_{con} is impedance due to connectorization, TL_{in} is the transmission line eq. impedance, $Z_{s1,s2}$ is due to bonding losses.)

Ceramic

Alumina (Al_2O_3) 99.6% has two versions by ATP [111], asfired and polished with at most 76 nm and 25 nm centerline average roughness, respectively. Thickness varies from 0.127 mm to 2.0 mm with a tolerance of around ±12.7 μm to ±25.4 μm. Dielectric constant (ϵ_r') is 9.9 at 1 MHz, going to 9.424 when approaching 17GHz. Loss tangent, defined as ϵ''/ϵ', is 0.0001 at 1 MHz, 0.0002 at 10 MHz and 0.00031 at 17 GHz [112]; further values are [113], 0.0004 at 40 GHz and 0.0005 at 100 GHz.

Metalization

The best conductor in the market to work together with Alumina 99.6% is gold. ATP, Kyocera [114] and other packaging distributors and manufacturers work with sputtered gold and electroplated gold on top. Electroplated gold will provide with lower medium square root roughness which is important to gain bandwidth when working with relatively long transmission lines.

Although other metals and composites are sputtered on top of the alumina surface, they are mostly small enough as not to affect the overall losses due to conductivity. Typical high conducivity, solderable/bondable compatible layers are: TiW (0.03-0.08 μm), sputtered Au (0.5-1 μm), electroplated Au (0.5-12.7 μm). For better wire bond suitability around 2 μm thick Au will be used in every simulation unless specified otherwise.

Attenuation constant of the RF transmission line is a linear combination of losses related to its dielectric and metal: $\alpha = \alpha_c + \alpha_d$. While α_d depends on the

tangent loss, finite electrical conductivity ($\tan\delta_c$) of metals affects directly the value of α_c. Furthermore, electroplated or sputtered gold have considerable roughness when working in high frequencies.

Roughness effects in the conductivity are dependent on frequency according to the first approach by Hammerstad and Bekkadal [115]. They define the corrected attenuation constant as: $\alpha = f_{rough}\alpha_c + \alpha_d$, where f_{rough} depends on the square root roughness parameter R_q according to:

$$f_{rough} = 1 + \frac{2}{\pi}\arctan\left[1.4\left[\frac{R_q}{\delta_s}\right]^2\right] \tag{4.1}$$

where skin depth (δ_s) is defined as $\delta_s = \sqrt{\frac{1}{\pi\mu\sigma f}}$.

After finding f_{rough}, we can define the rough metal conductivity as [116]:

$$\sigma_{rough} = \frac{\sigma}{f_{rough}} \tag{4.2}$$

where the bulk conductivity of gold $\sigma = 4.1 \times 10^7$ S/m [117]. Measured root-mean square height of electroplated gold goes from $\sim$ 7.2 nm to 14.9 nm according to [118] using silicon wafer as substrate, and from 50 to 100 nm according to [119] using polymer or ceramic as substrate. By using (4.2) and (4.1) we found a frequency dependent function for $\sigma_{rough} = 3.78$ S/m at 65 GHz, which is going to be used in all simulations later on.

4.3.2 Wire bonding

Wire bonding effects in the electrical signal path are represented in Figure 4.3 as $Z_{s1,s2}$.

Wire bonding process consists on melting the tip of a gold wire by heating plate and microwaves to bond it to a preferably thick gold pad. As the gold wire passes its melting temperature, the diameter thickens usually until doube its size [120, 121]. Thus, the bonding pad has to be at least two times the wire diameter and at least $1.5\mu m$ thick to avoid material damaging and undesired contacts. In this section, a performance study by FEM modeling of various wire bonding transitions using CST software [106] is presented. To evaluate the effect of wire bonding, let us consider two sets of lossless 50 Ω generic coplanar pads which are interconnected by 18 μm wires as shown in Figure 4.4(a). Most manufacturers specify a minimum spacing between circuit edge and metalization. In alumina/thin film it usually is 25.4 μm, while in Silicon substrate chips it is about 30 μm. Thus, we will fix $h = 60$ μm and sweep d from a minimum of 40 μm to 150 μm, which could encompass possible misalignment between chips. We found that higher distances d prompt wire length to increase as well, which in turn makes the transition more inductive, specially as frequency increases (see Fig. 4.4(b)). Another less forceful cause for wire length increasing is h, its impact is depicted in Figure 4.4(c) for a fixed $d = 68$ μm. Good

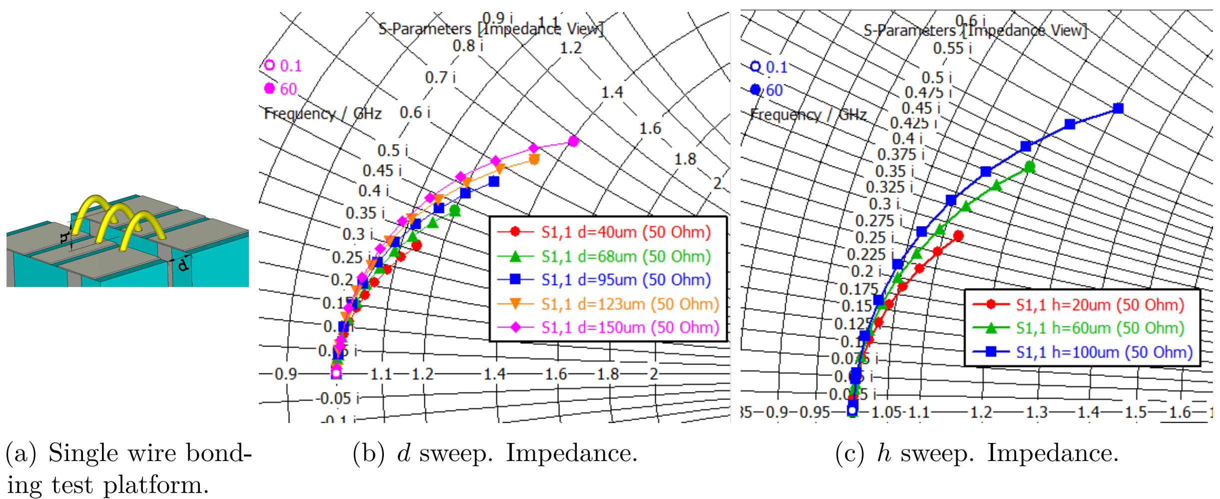

(a) Single wire bonding test platform. (b) d sweep. Impedance. (c) h sweep. Impedance.

Figure 4.4: Single wire bond test. Distance between pads (d) and wire height (h) were sweeped.

crafting and wire bonding machinery can minimize h; an optimal value of 20 μm can be considered, but future simulations will use 50 μm as a safe repeatable value.

To minimize inductance induced losses, double wiring (Fig. 4.5(a)) has been recommended for wide bands of up to 50 GHz [122]. Figures 4.5(b) and 4.5(c) show h and d dimension sweeps using double bonding. As the distance between pads (d) increases, the overall impedance is more controlled and even wire height diminishes its effect when $h = 60$ μm.

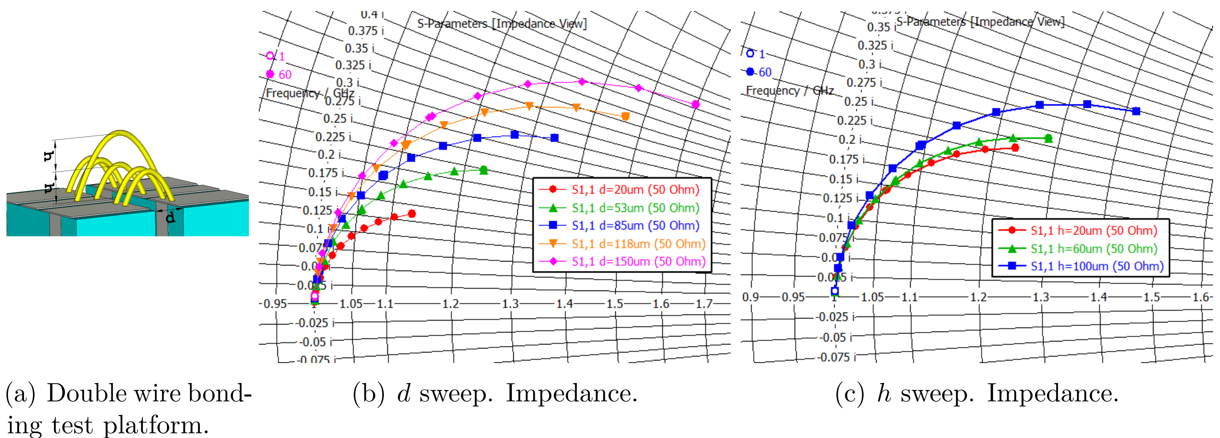

(a) Double wire bonding test platform. (b) d sweep. Impedance. (c) h sweep. Impedance.

Figure 4.5: Double wire bond on signal pad test. Distance between pads (d) and wire height (h).

An important high frequency alternative to wire bonding is ribbon bonding [123, 124]. Pads are interconnected with thick gold strips which are $12.5\mu m$ thick and their width can be adjusted to various pad widths. As the signal pad of a LX8242 TFPS modulator is $100\mu m$ wide, $50\mu m$ ribbons were used in the test platform as shown in Figure 4.6(a). Inductive behavior is not as good as double wiring (see Fig. 4.6(b)) but it shows

an important improvement from single wire test which was already reported in [122].

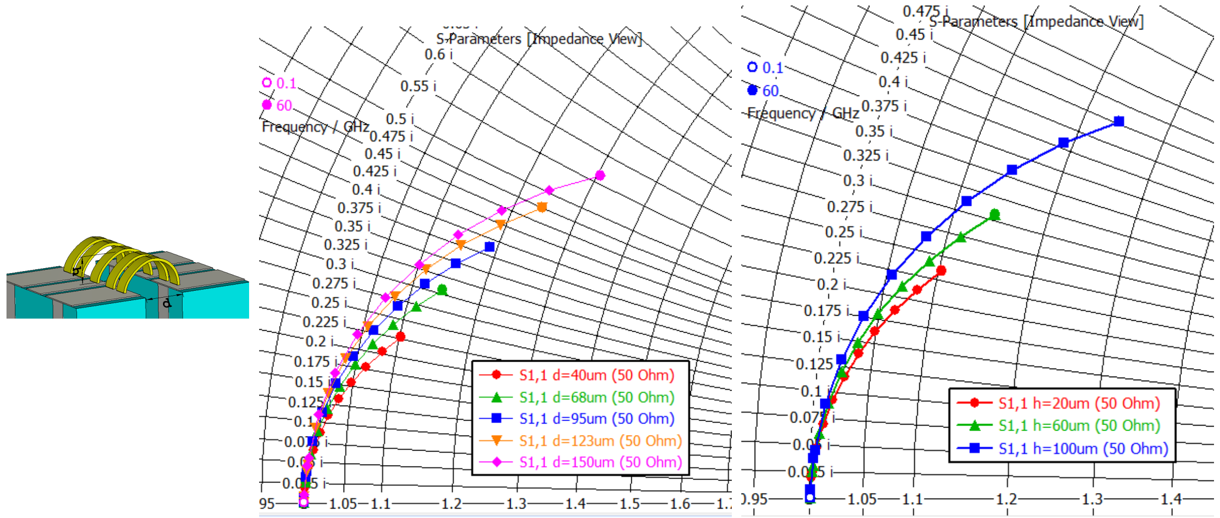

(a) Ribbon bonding test platform. (b) d sweep. Impedance. (c) h sweep. Impedance.

Figure 4.6: Ribbon interconnection pad test.

The Electric field distribution on a ribbon bond 4.3.2 is more similar to the coplanar port mode distribution, given the planarity of the ribbon, while in the single wire case, there is an abrupt width change from pad to wire diameter. On the other hand, double wire bonds on the signal pad favor the coplanar super-mode propagation with two positive and two negative potentials. Note that single wire electric field distribution shows resonance on high frequencies which is coherent with the results in [125].

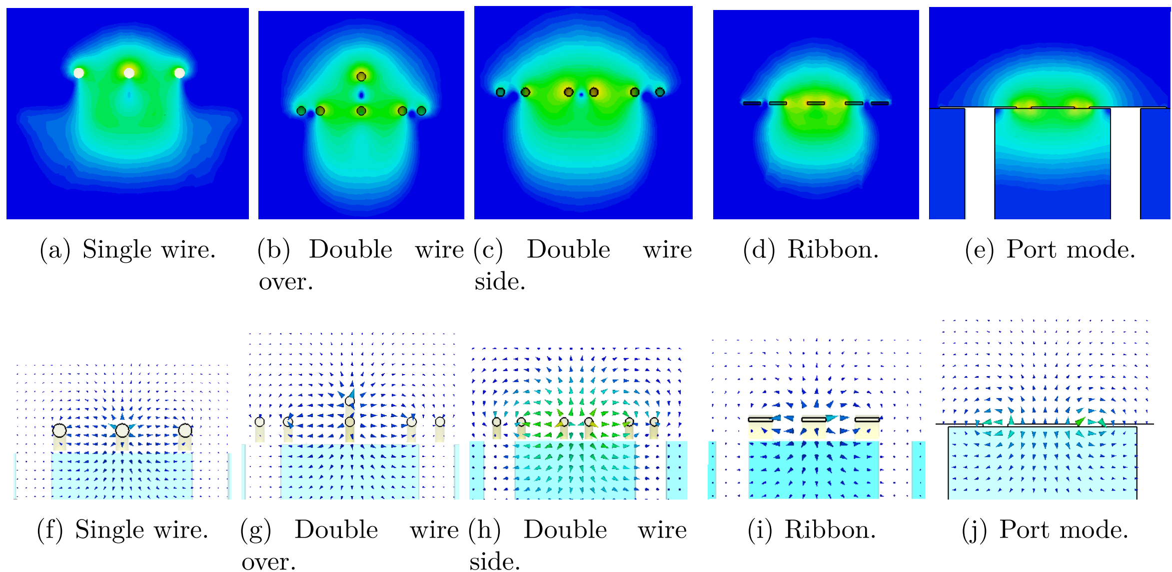

(a) Single wire. (b) Double wire over. (c) Double wire side. (d) Ribbon. (e) Port mode.

(f) Single wire. (g) Double wire over. (h) Double wire side. (i) Ribbon. (j) Port mode.

Figure 4.7: Comparison between the electric field distribution at 40 GHz at the center ($d/2$) of all bonding test platforms and the coplanar waveguide set of pads mode used.

4.3.3 Electrical Feed by Connectors

Low loss connectors to feed a transmit optical subassembly RF circuit are one of the main recommendation for high-speed feeding by the OIF transmitters regulation [44].

Wide band precision RF GPPO-like W1 connector by Anritsu [126] is suitable for frequencies from DC to 110GHz with a typical insertion loss of 0.7dB. Dimensions of the female connector are $38.5mm^2 \times 12.27mm$ (see Figure 4.8 for further details).

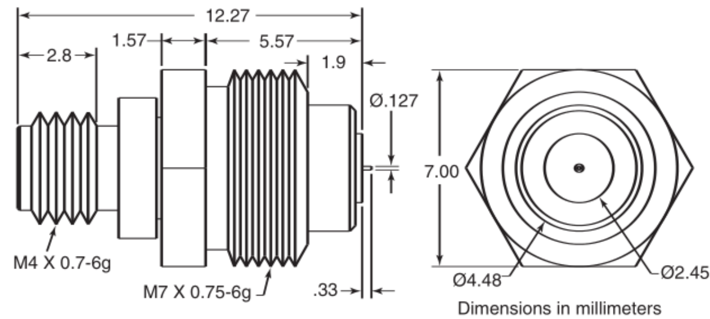

Figure 4.8: Female W1 connector schematic as shown in Anritsu catalog [126]. Dimensions in millimeters

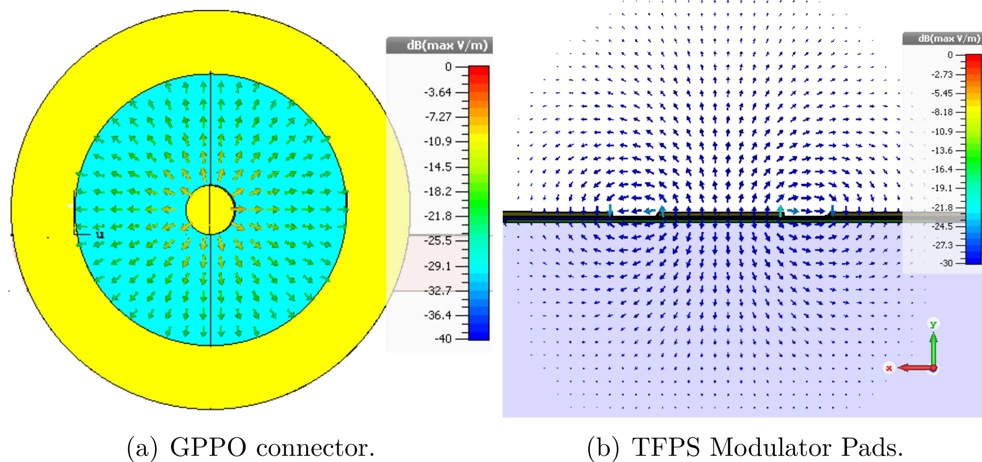

(a) GPPO connector. (b) TFPS Modulator Pads.

Figure 4.9: GPPO connector and differential input TFPS modulator pads Electric field distribution comparison.

Let us consider the input of a single-ended Mach-Zehnder TFPS modulator (Fig. 4.10(a)). RF In is the input high speed signal pads which for a single-ended configuration would be in a Ground-Signal-Ground (GSG) arrangement. These pads convert coplanar supermode to microstrip TL mode. Light and electric signal interaction occur in the Active Region. After this section, the RF circuit ends on 50Ω termination pads (RF out).

A more detailed picture of the coplanar waveguide RF input pads is shown in Figure 4.10(b). The electric field vector of a single-ended modulator (shown in Figure

4.9(b)) corresponds to the E-field of a coplanar transmission line with two grounds, and it has big similarities with a typical GPPO connector transverse E-field (see Fig. 4.9(a)).

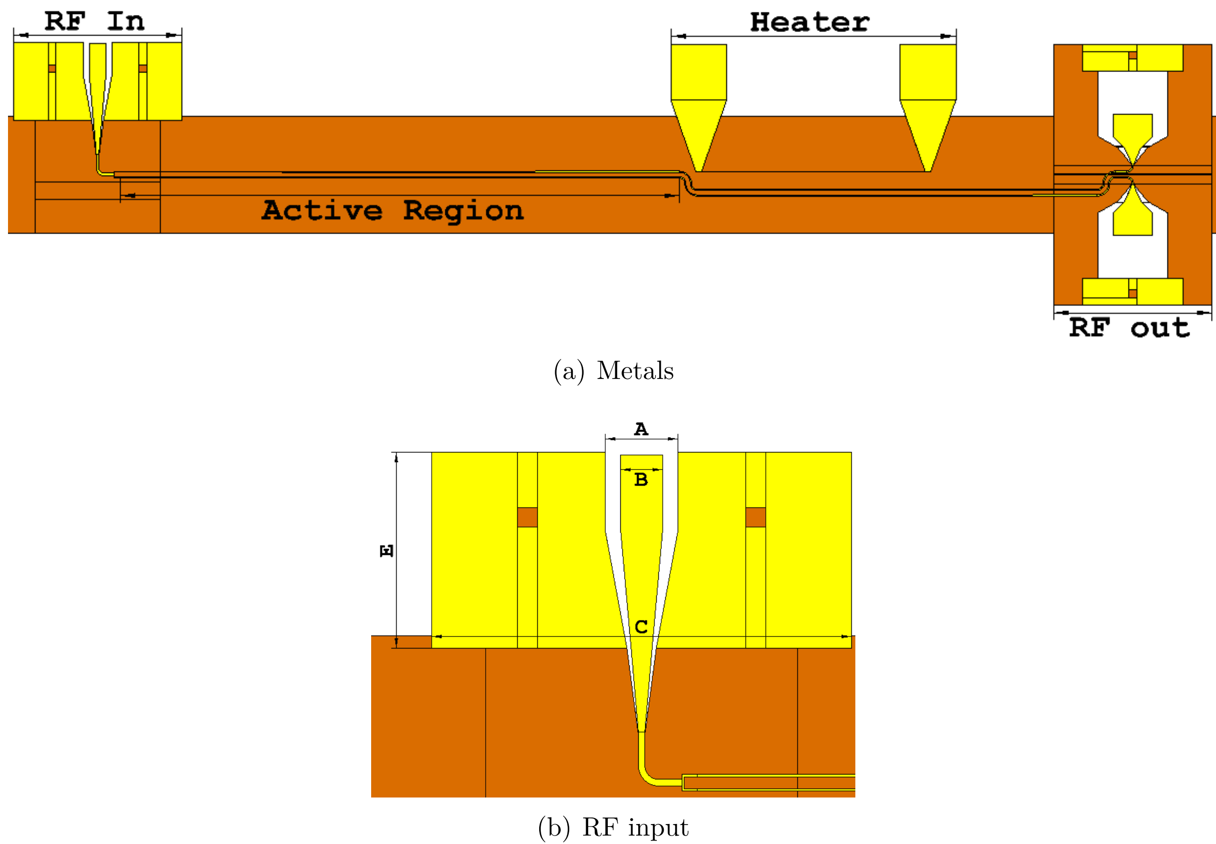

(a) Metals

(b) RF input

Figure 4.10: Single ended MZ TFPS modulator schematic. Yellow represents the electrical path's trace. Ground metalization is represented in orange.

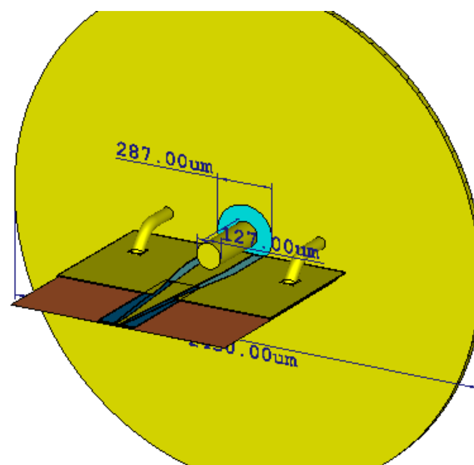

Figure 4.11: W1 connector attached to a single-ended MZ TFPS modulator input.

A W1 connector attached to the RF input pads through wire soldering is shown in Figure 4.11 as modeled in CST Studio Suite simulator [106]. S-parameters of this geometry are shown in Figure 4.12 considering the following values (from Fig.

4.10(b)): $A = 260\mu m$, $B = 150\mu m$, $C = 1500\mu m$ and an adiabatic transition from CPW to microstrip of at least $E = 600\mu m$. Coplanar to microstrip on-chip conversion can be disregarded if the transition is adiabatic (see S-parameters in Fig. 3.16) and the impedance remains 50Ω. Nevertheless, for the specific LX8901 TFPS BrPhotonics/Gigoptix modulator, each active region microstrip characteristic impedance has to be $\sim 50\Omega$ which has a significant effect on the return loss as shown in Fig. 4.12.

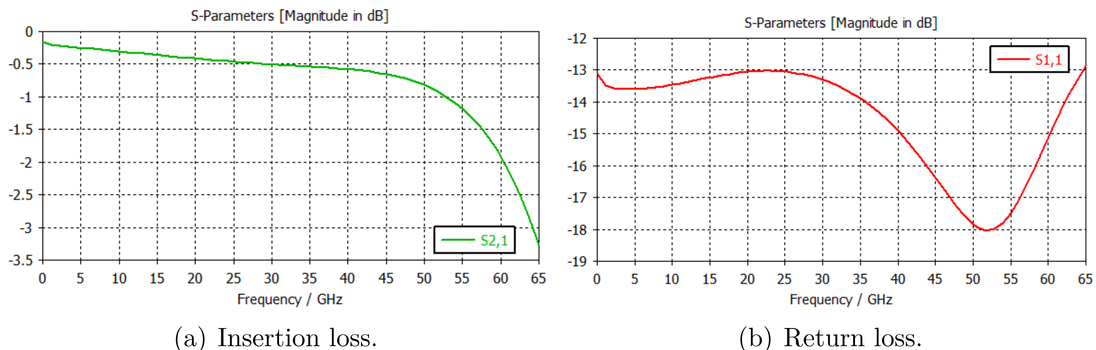

(a) Insertion loss.

(b) Return loss.

Figure 4.12: W1 connector/single-ended modulator transmission and reflection parameters.

As G3PO connector dimensions (see Fig. 4.13(a)) practically double the input of LX8901 pads, we can note that a package which uses W1 connector is the correct choice. Mismatch between other GPPO connectors such as G3PO can be solved by fabricating an spot size converter on a thin film ceramic.

A $3mm$ long taper as a mode size converter on a $508\mu m$ thick alumina substrate (see Fig. 4.13(b)) was designed to match the mode of a G3PO connector size. Gold filled vias were used to maintain 50Ω line impedance through the whole length. Figure 4.13(c) shows the mode conversion over a linear taper. Metallic regions are represented in white/gray where tangential electric field is $E_t \sim 0$.

The backside of a G3PO connector is soldered in a similar fashion as a W1 (see Figure 4.14(b)). We demonstrated that even by using a 3 mm taper and gold wire bonding, as shown in Figure 4.14(d), the result is considerable band improvement of 18 GHz as seen in Figure 4.14(a). Return loss has a significant improvement of about 4.6 dB when $f < 45$ GHz and 1 dB when $f > 60$ GHz.

Although these connectors can be directly soldered to the chip's transmission line input or with a small transition to minimize return loss, when working with any form of quadrature modulation the quantity of connectors needed to feed our TOSA increases with the modulation complexity which directly affects packaging dimensions.

4.3.4 Electrical Feed by Multipin RF Layouts

To attend TOSA packaging size demands, multipin RF surface mount (SMT) feed-through layouts, regulated by the OIF [44], with 1.0mm and even 0.8mm pitch can be

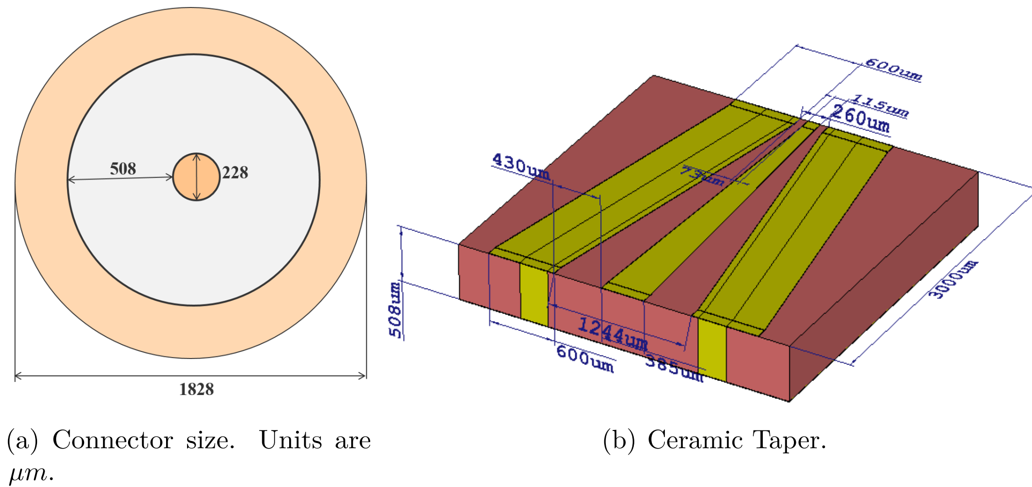

(a) Connector size. Units are μm.

(b) Ceramic Taper.

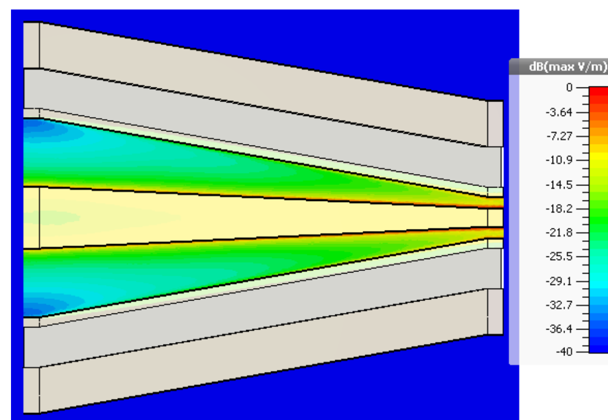

(c) E-field distribution@40GHz.

Figure 4.13: Ceramic taper for packaging with G3pO connector using LX8901 single-ended TFPS modulator.

used. Kyocera [114] offers four channel layouts solutions for TOSA, ROSA and transceivers attending 100Gbps regulation.

Flexible printed circuit boards (PCB) [127, 128] are used as multipin connectors to attach TOSA into a carrier (generally PCB). More recently there have been applications using flexible PCB for better connector positioning [129, 130] and transmitter/receiver interconnection to form a transceiver module [131].

Surface mount feed-through layout with 0.8mm pitch is presented in Figure 4.15(a), which was extracted from OIF regulation. A longitudinal cut of the electric field shows correct excitation of GSSG differential interface (see Fig. 4.15(b)). When quadrature configuration of MZ modulators is needed, adjacent modulator share the same ground in a GSSGSSG configuration.

Quadrature TFPS modulator feeding pads are shown in Figure 4.16. Four signal inputs on a GSGSGSGSG configuration which correspond to two Mach-Zhenders electrodes are observed. All four signal pads are 100 μm wide while ground pads are 130 μm. Distance between signal pads of a differential line is 300 μm. Two differential signals

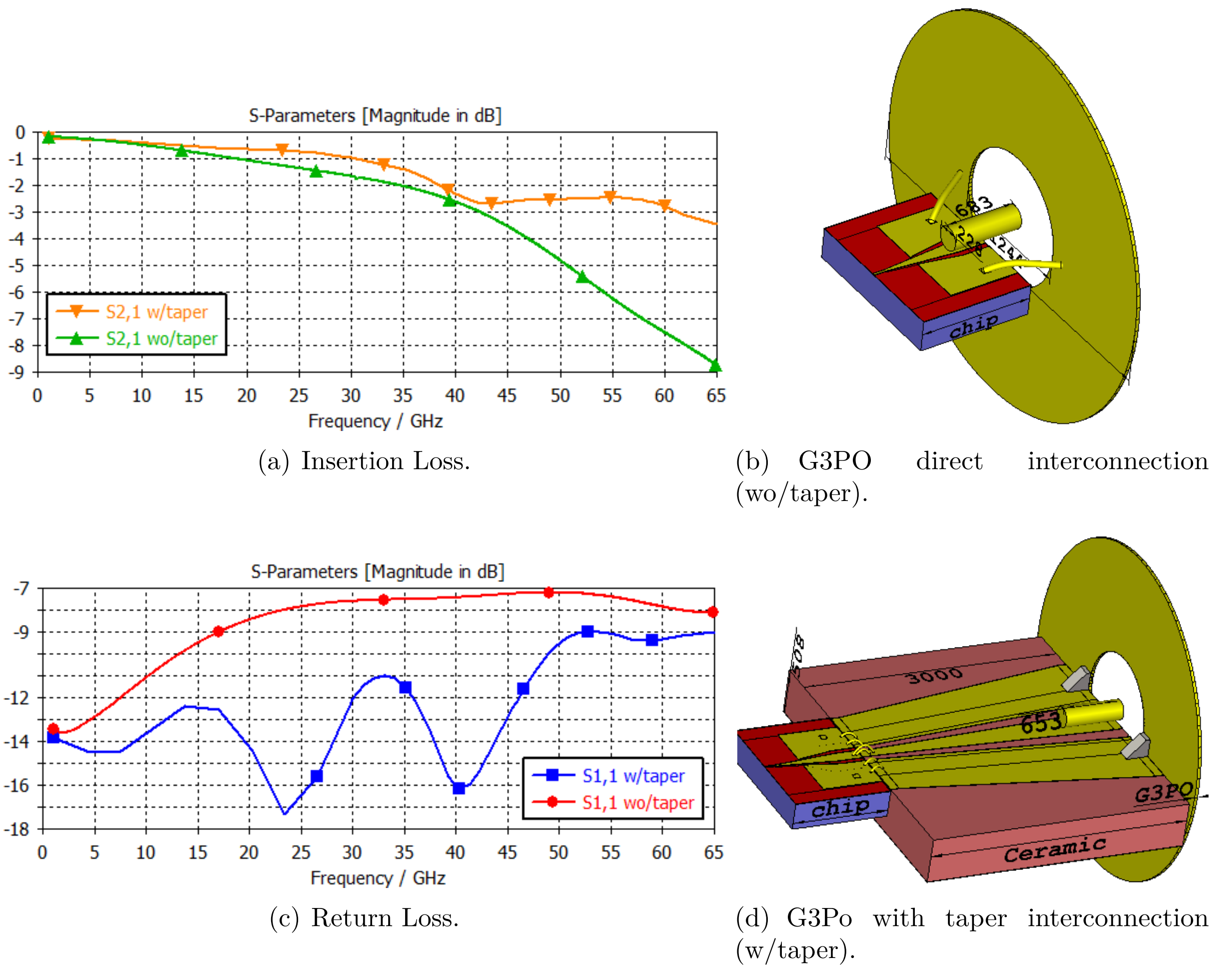

(a) Insertion Loss.

(b) G3PO direct interconnection (wo/taper).

(c) Return Loss.

(d) G3Po with taper interconnection (w/taper).

Figure 4.14: S-Parameters of tapered and taper-less G3PO connection to an LX8901 by Gigoptix/BrPhotonics. Dimensions in μm.

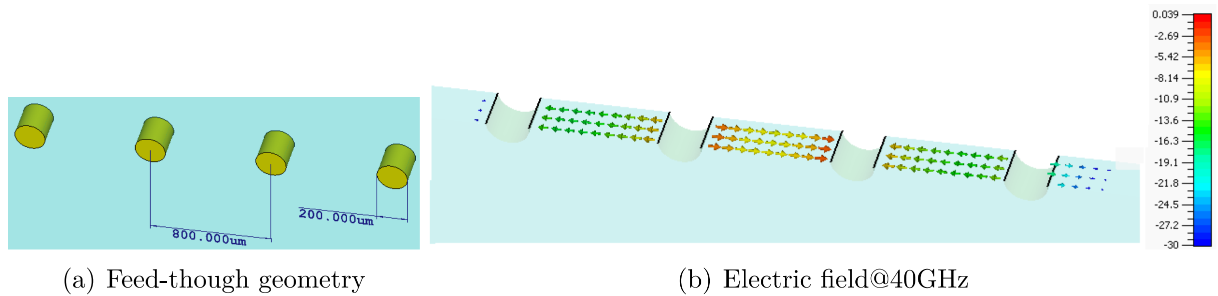

(a) Feed-though geometry

(b) Electric field@40GHz

Figure 4.15: Differential feed-though interface with 0.8mm pitch, according to OIF agreement.

are separated by a 180 μm ground pad. Coplanar transmission line mode is adiabatically transformed into a microstrip mode which is 12 μm wide. Line impedance is kept at 50Ω throughout the entire transition.

Size difference between modulator pads and the feed through layout are the scope of this section. For maximum transmission efficiency, a TL that will also work as a mode size converter was designed to keep a differential impedance of $Z_{DIFF} = 100\Omega$. This

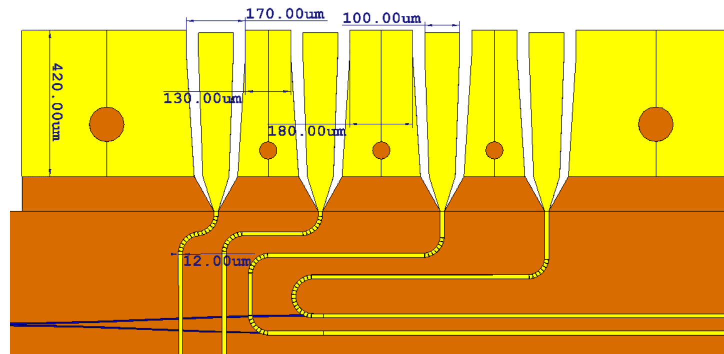

Figure 4.16: Electrical feed pads of an LX8242 DP-QPSK TFPS modulator by Gigoptix/BrPhotonics. Only two sets of electrical pads corresponding to two Mach-Zehnder modulators are shown. Yellow represents top metalization. Bottom lamination is orange. Optical trench is represented in blue. Dimensions in micrometers.

mode converter was designed on a 127 μm thick polished alumina substrate with about 2 μm golden top metal as depicted in Figure 4.17(a).

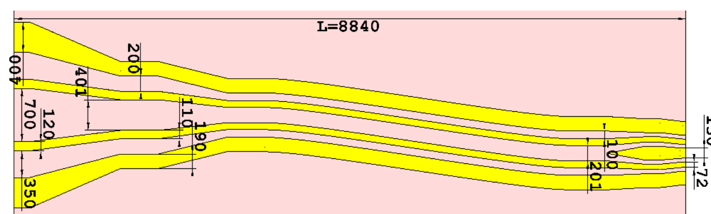

(a) Geometry. Dimensions in μm

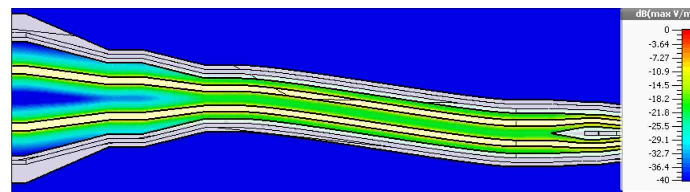

(b) E-field distribution @40GHz.

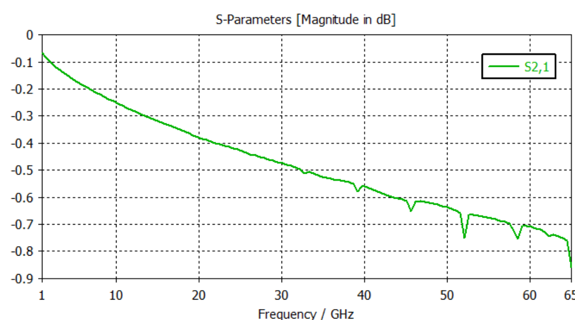

(c) Transmission.

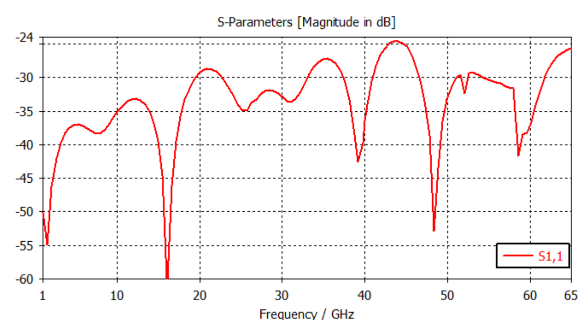

(d) Reflection.

Figure 4.17: Interconnection ceramic. Top metal is represented in yellow while Alumina 99.6% is pink. Dimensions in micrometers.

The inferior end of the TL is matched to the TFPS modulator input pads which are in a GSGSG configuration. To convert GSGSG into GSSG we extend the center ground

and then interconnect it through a filled via to the backplane gold metalization. Considering the minimum aspect ratio of a filled via in thin film technology $\frac{d_{via}}{substratethickness} = 0.5$, an extension of the center ground pad is needed to place the center GND via. After this, two coplanar differential lines travel through the rest of the length (see Figure 4.17(a)). Side grounds are also interconnected with vias, which can be seen in the E-field distribution (in Fig. 4.17(b) metal is represented in white where $E_t = 0$). As all transitions have been made adiabatically, we found insertion loss to be less than 0.8dB and return loss is better than -24dB on an 8840μm long interconnection ceramic.

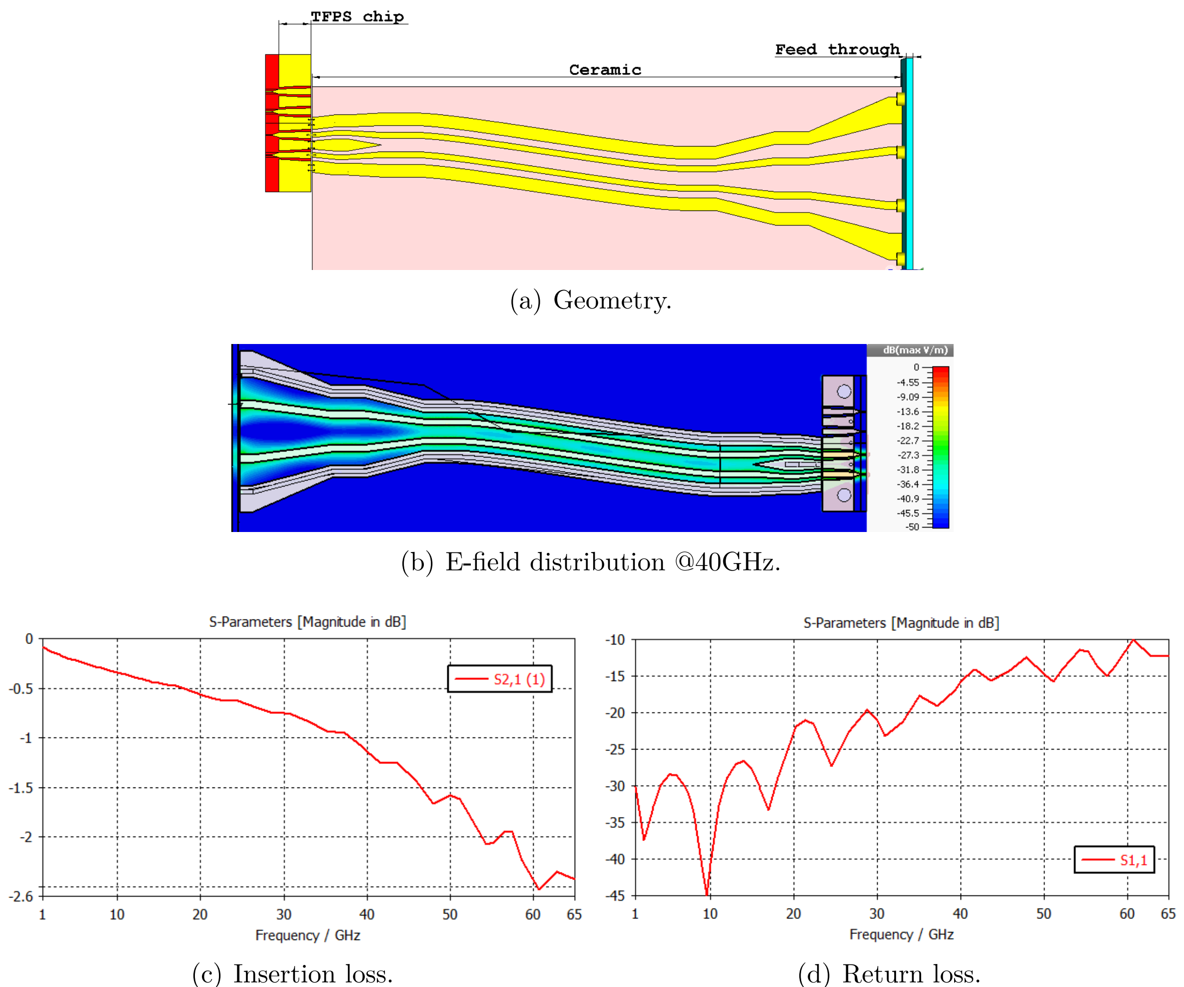

(a) Geometry.

(b) E-field distribution @40GHz.

(c) Insertion loss.

(d) Return loss.

Figure 4.18: Feeding transmission line with feedthrough pins layout and wire bonds towards the modulator pads. S-Parameters of the whole feeding transmission line including losses caused by wire bonding.

Setting up the RF circuit, we interconnect the feed through, ceramic and TFPS modulator chip pads with double signal and ground wire bonding as shown in Figure 4.18(a). The electric field distribution (in Fig. 4.18(b)) shows no abrupt changes and an overall smooth distribution, which is reflected in the low loss of up to -2.6dB at 60GHz and a very controlled return loss that is better than -10dB in the whole band.

4.3.5 Termination circuit

Conceptually, a termination circuit has an ideal capacitor that allows only RF signal through and blocks direct current bias as shown in Figure 4.19. Then, a resistor which will act as a circuit terminator need to match the transmission line characteristic impedance, $R_{TL} = Z_L = 50\Omega$. Although real components have parasitic elements, in this section we considered only their geometry and the effect it could cause on a $60GHz$ band RF path.

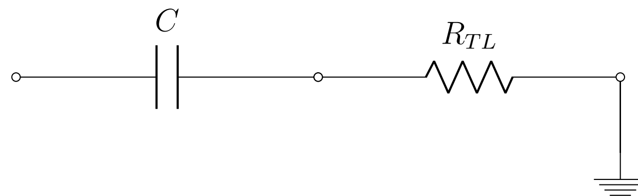

Figure 4.19: Termination Circuit for a TFPS MZ modulator.

Let us consider the output pads of LX8242 Gigoptix/BrPhotonics TFPS modulator as depicted in Figure 4.20. Distance between ground pads is $170\mu m$ while the signal pad is $100\mu m$ wide. On the other side typical wide band components have very large pads (see Figs. 4.21(a) and 4.21(b)). To achieve wide band towards ultra-high speed applications, transmission lines that ensure low reflection coefficients have to be proposed for industry applications.

To match the impedance and dimensions of Fig. 4.20, a $508\mu m$ thick alumina was selected. Dimensions are detailed in Figure 4.22(a). Capacitor and Resistor faces represent lumped elements in our simulation environment.

Coplanar mode stimulus at the TL input gives us a very controlled reflectance, under $-20dB$ in the whole band, as depicted in Figure 4.23(a), turning slightly more inductive when reaching higher frequencies (from fig. 4.23(b)). As two consecutive pad termination can be found in any quadrature modulator, we bended the termination 65° and sought to minimize its effect by smoothing any peaks.

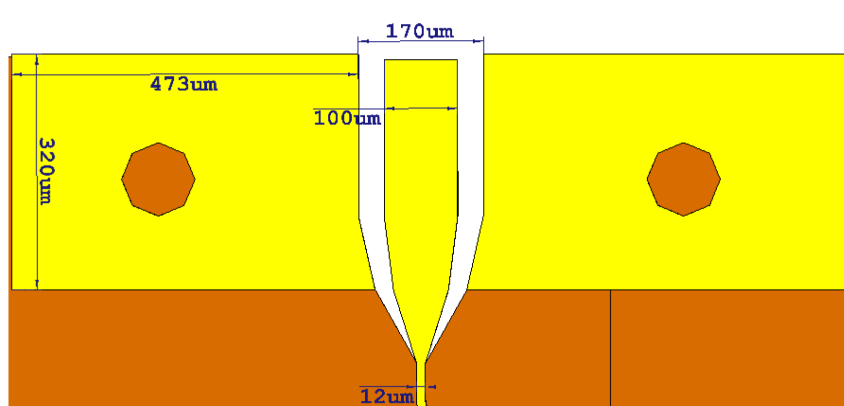

Figure 4.20: LX8242 coplanar waveguide RF output pads.

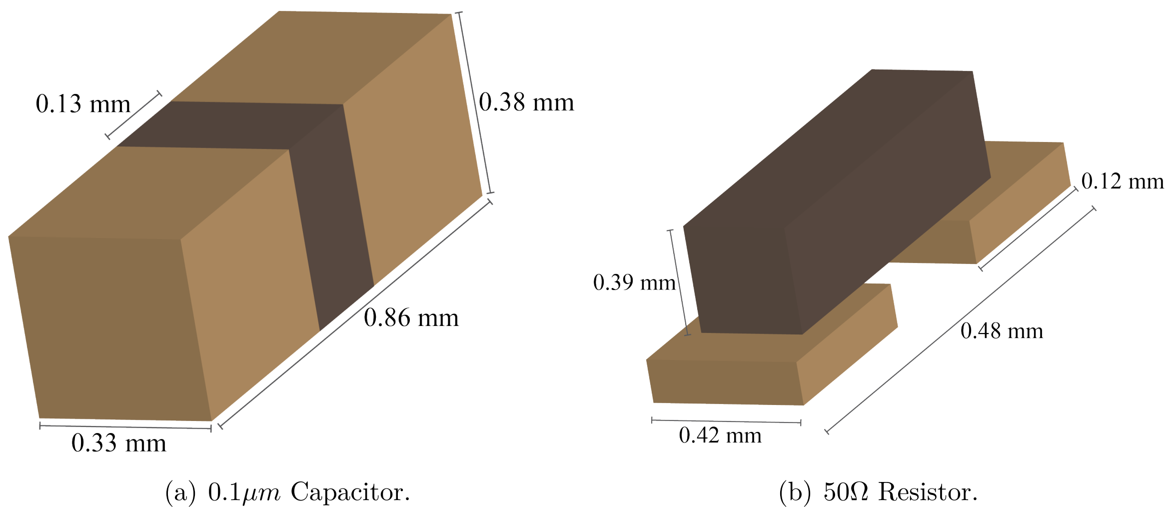

(a) $0.1\mu m$ Capacitor.

(b) 50Ω Resistor.

Figure 4.21: Common dimensions examples of wide band elements. Dimensions are in millimeters. Tolerances are ranging from ±0.02 to ±0.05 mm.

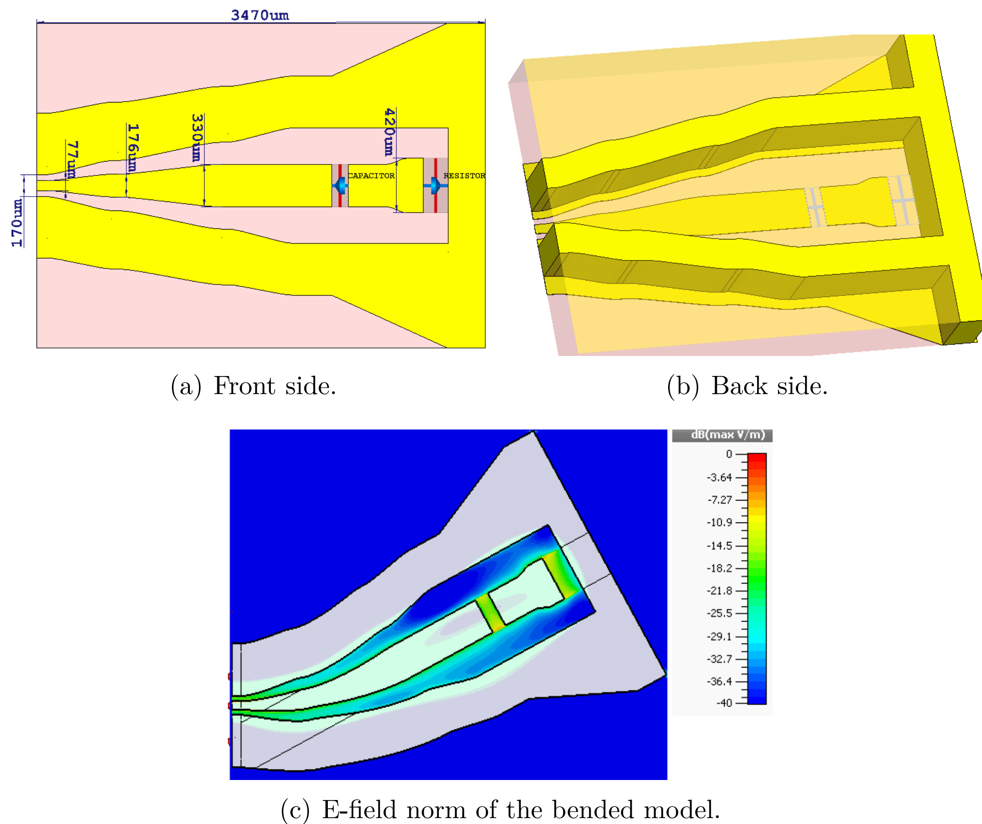

(a) Front side.

(b) Back side.

(c) E-field norm of the bended model.

Figure 4.22: Termination transmission line with capacitor correction and characteristic impedance matching resistor.

Wire bonding changes the TL behavior to mostly inductive from 19 GHz to 39 GHz and more capacitive from 40 GHz to 65 GHz (Fig. 4.24(c)) while it also increases the return loss magnitude by $\sim 4dB$ when $21 > f > 40$ GHz and by a maximum of 8 dB at 60 GHz which is understandable given that the overall simulation includes RF input pads transition to microstrip TL inside chip (see Fig. 4.24(a)).

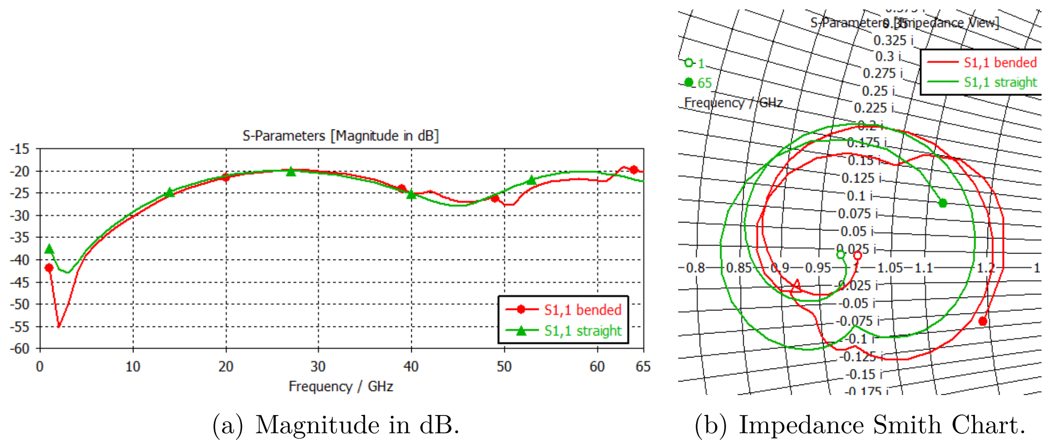

(a) Magnitude in dB. (b) Impedance Smith Chart.

Figure 4.23: Reflection coefficient of the designed termination transmission line with capacitor correction and matching resistor.

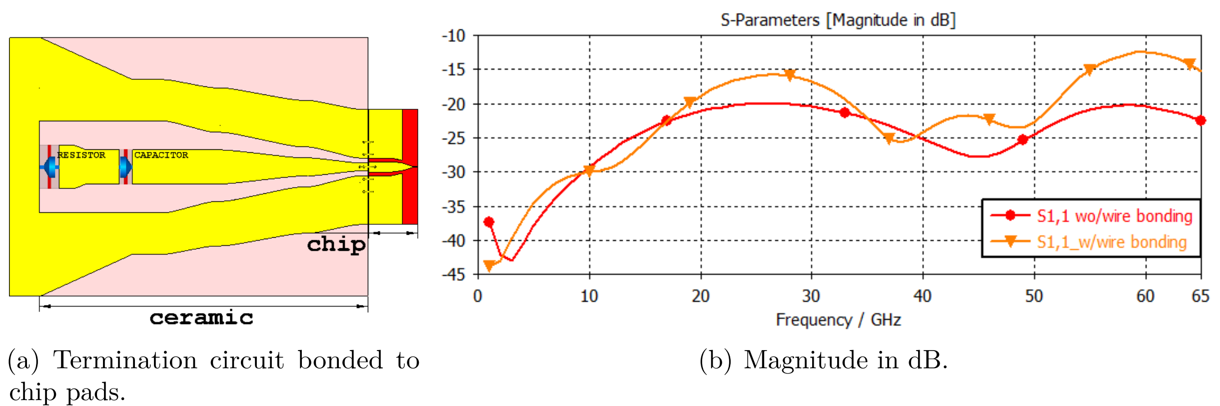

(a) Termination circuit bonded to chip pads.

(b) Magnitude in dB.

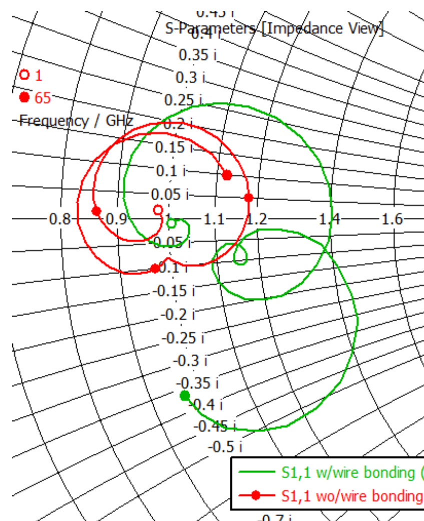

(c) Impedance Smith Chart.

Figure 4.24: Reflection coefficient of the termination transmission line considering wire bonding. wo/wire bonding describes the behavior of the ceramic transmission line by itself, while w/wire bonding shows the behavior of the TL plus wire bonding set and the modulator's input pads.

4.4 Electrical Path

Let us consider the electrical signal path described in Figures 4.2 and 4.3. Z_{con}, TL_{in} will vary according to the type of connector used.

In this section return loss of the whole packaging electric system, including TFPS chip, will be calculated and compared with today's industry requirements previously described in Section 4.2.

4.4.1 Single-ended Modulator

For a single-ended electrooptical polymer modulator matching the one in Fig. 4.10(a), let us consider first a W1 connector attached to the RF in pads as shown in 4.11, microstrip transmission line in the active region, followed by the output microstrip towards the RF out section where 50Ω resistors are placed to match each TL (see Fig. 4.25).

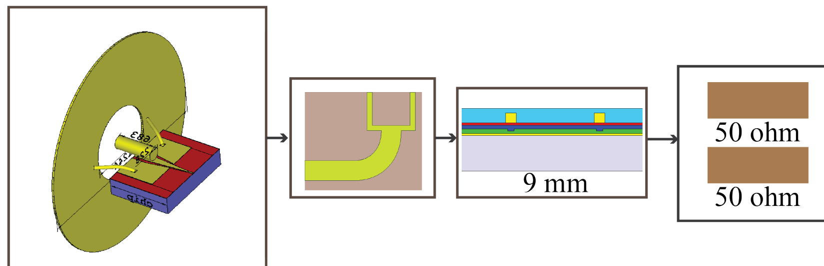

Figure 4.25: TOSA electrical path of the single-ended modulator with W1 connector.

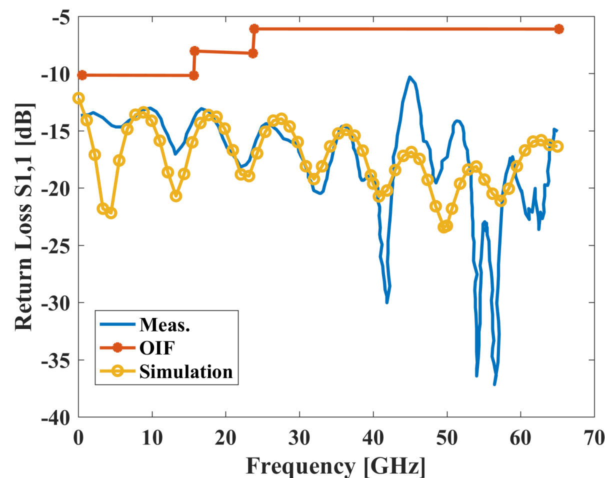

Figure 4.26: Measured and simulated results of the TOSA electrical path for LX8901 BrPhotonics modulator with W1 connector.

Measurements of a TOSA with W1 connector on a LX8901 BrPhotonics/Gigoptix modulator were performed and compared to our electromagnetic model. Results are de-

picted in Fig. 4.26. Differences between simulated and measured results when frequency is > 40 GHz can be attributed to wire soldering.

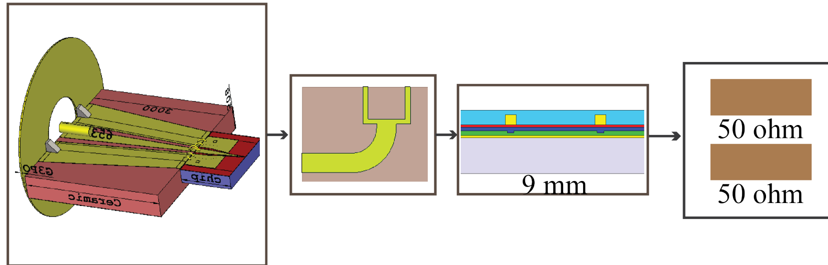

Figure 4.27: Single-ended modulator TOSA electrical path with G3PO connector.

A G3PO connector was directly soldered to an LX8901 modulator similar to the configuration in Fig. 4.14(b). The measured and simulated results are shown in Fig. 4.28.

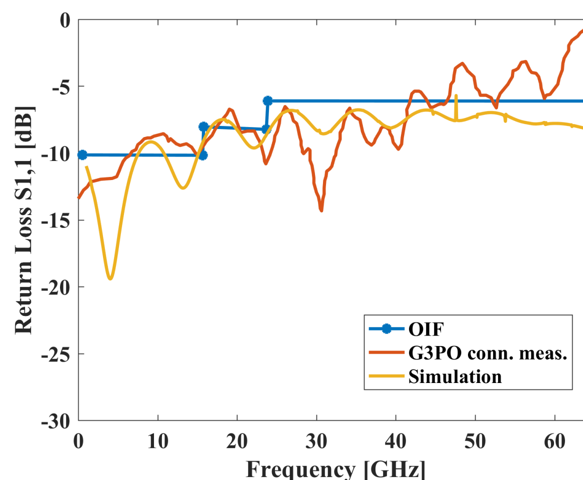

Figure 4.28: G3PO wire soldered to an LX8901 TFPS modulator.

Once the model was validated by the good agreement in Fig. 4.26, our proposal to accommodate the mode linearly by using a tapered coplanar TL as interconnect for a typical G3PO connector (see Fig. 4.14(d)) is depicted in Figure 4.27.

Figure 4.29 shows the return loss. OIF recommendations are depicted in red. All recommendations were met, while there is an important improvement over direct G3PO connectorization.

4.4.2 Quadrature Modulators

Multi-platform high integration, quadrature electrooptic polymer modulators can be interconnected by feed-through multi-pin configuration. Let us use the results from Fig. 4.18(d) as an starting building block to include the LX8242 BrPhotonics/Gigoptix

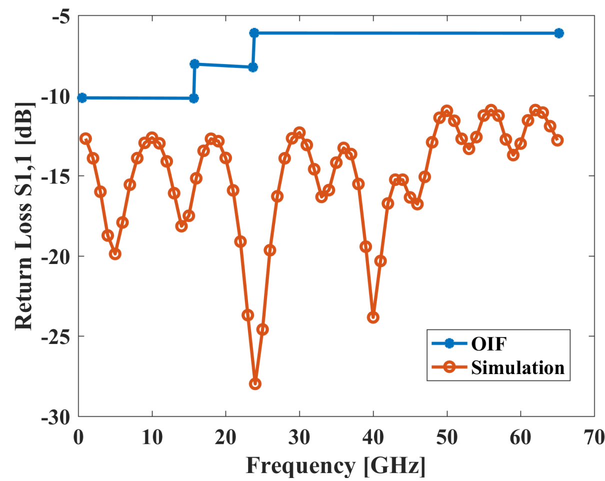

Figure 4.29: Return loss of the G3PO connector TOSA with mode converter taper when compared to OIF recommendations.

TFPS modulator depicted in Figure 4.30. As the feed is a differential signal of the form GSSG, the electric signal goes through an 15700 μm microstrip TL length where only 9 mm correspond to the active region (where modulation is performed, see Chapter 3) and each microstrip TL ends on a single-ended 50Ω termination as seen in Fig. 3.1.

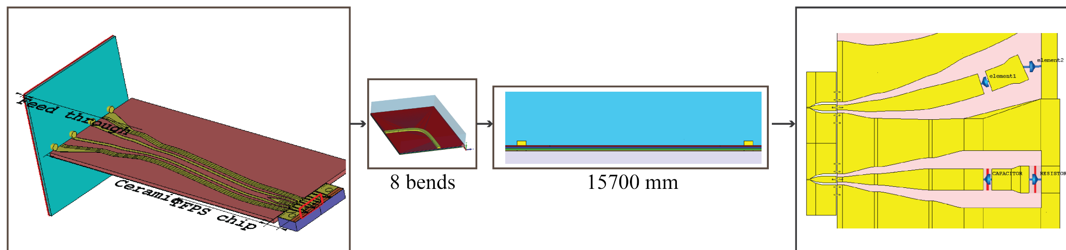

Figure 4.30: Feed through pins interconnection with LX8242 modulator by BrPhotonics electric path diagram.

Figure 4.31 shows the return loss of the system in Fig. 4.30. OIF criteria was met while the ceramic RF remains small (less than 13 mm of electrical path). The low values of $S_{1,1}$ towards the higher frequency bound could be used to project these kind of RF ceramic packaging path for enabling even 400G quadrature EO polymer modulators.

4.5 Electrooptic bandwidth

By using the definitions described in Chapter 3, we obtained the electrooptic response of the system which is shown in Figure 4.32. The dashed line is the electrooptic response of an LX8242 electrooptic polymer modulator chip and the continuous line shows the electrooptic response of an LX8242 chip cascaded with the RF feed depicted in Fig. 4.18(a).

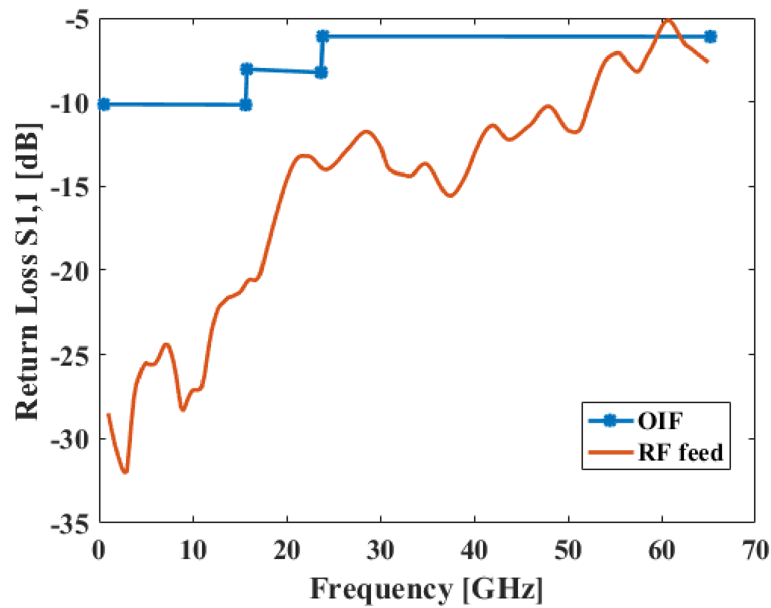

Figure 4.31: Return loss of Fig. 4.30 configuration.

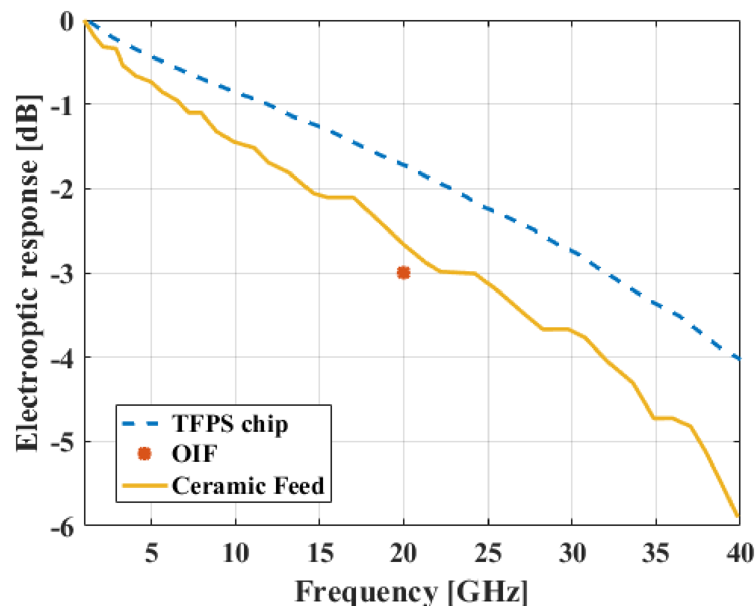

Figure 4.32: Electrooptic response of the LX8242 chip compared to proposed RF feed plus chip response.

The electrooptic band of the TFPS chip at the 0.5% of the max. reference level for a $1GHz$ normalized response is 31.7 GHz. BrPhotonics internal reports provided the measured electrooptic band of the TFPS chip to be 26 GHz. However, a de-embedding process was performed considering the electrical response of the probe used to execute the electrooptic measurements, reaching a band of 31 GHz, which is in good agreement with the simulation.

When the ceramic RF feed is cascaded with the TFPS chip, the electrooptic

band is 22.2 GHz. Overall, there is a loss of 9.5 GHz of band when interconnecting the chip into the ceramic packaging.

4.6 Summary

An RF ceramic path for packaging applications for electrooptic polymer modulators was presented. Return loss was kept well bellow the OIF recommendations for metro and long-haul networks for both, single-ended and quadrature modulators with single and differential signals, respectively. Furthermore, the electrooptic bandwidth with RF packaging electric path fell only 9.5 GHz when compared with the chip-only simulation.

Chapter 5

Optical Interconnects

Different optical technologies allow for different monomode waveguide dimensions. Many passive devices have been demonstrated in this platform: rotators [71, 72, 132] and splitters [73], crossings [133, 134] and many others [74] that enable high throughput optical interconnects for telecom applications.

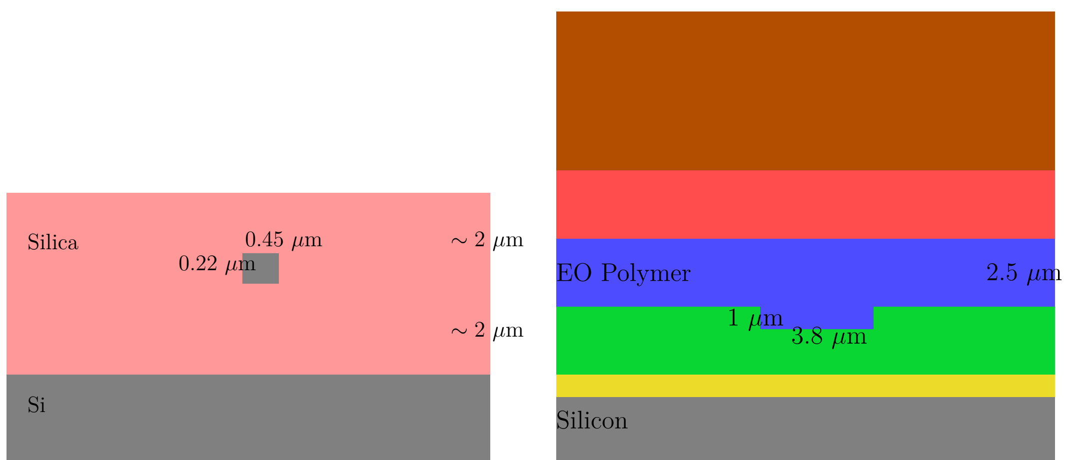

(a) Silicon-on-insulator channel waveguide with silica cladding.

(b) EO Polymer modulator waveguide

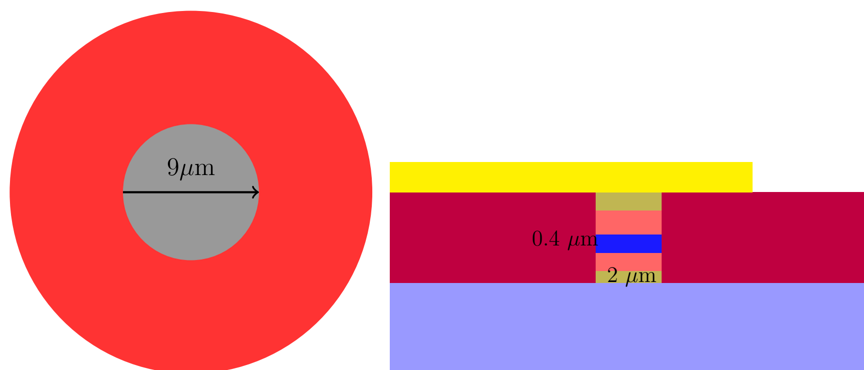

(c) Monomode silica fiber.

(d) High III-V semiconductors.

Figure 5.1: Typical core dimensions of the different technologies on a hybrid Transmitter Optical Subassembly. Not to scale.

Consider a silicon-on-insulator waveguide geometry like the one in Figure 5.1. While Silicon-on-insulator platform monomode waveguide core width is around 0.45 μm and thickness is typically 0.22 μm, polymer waveguide core dimensions are around eight times bigger. Typical monomode silica fiber core diameter is 9 μm. Lastly, depending on the technology, III-V semiconductor waveguides, suitable for active devices, range from 2 μm to 3.5 μm wide.

The substantial difference between technologies suggest the need for adequate spot size converter devices, which we are going to call optical interfaces or interconnects.

5.1 Design Methodology

Our contribution to the design methodology of optical interconnects for transmitter optical sub-assemblies applied to non-coherent long-haul data center interconnect devices is the application of basic notions of the mode coupling theory to optimize the polymer/silicon-on-insulator vertical interconnect. The design methodology followed in this chapter is depicted in Fig. 5.2. The flux blocks diagram is described bellow.

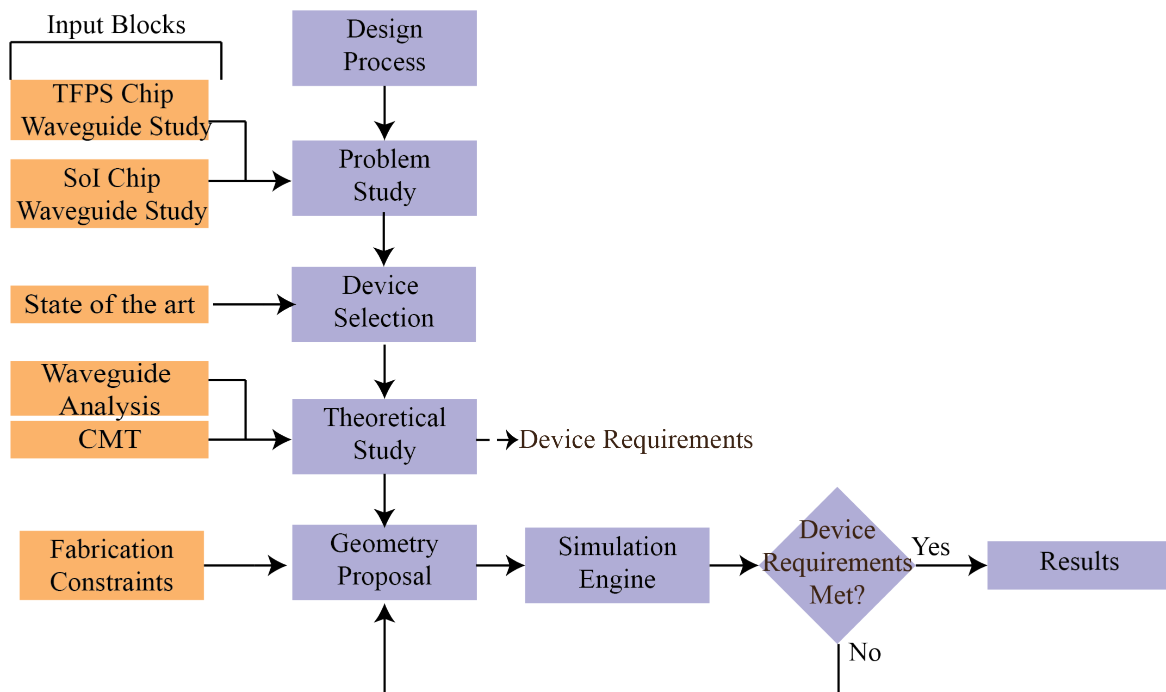

Figure 5.2: Flux blocks diagram showing the design methodology used for our optical interconnect.

First, the SOI and TFPS modulator waveguides size difference and refractive index mismatching are studied in the Problem Study block. To overcome these issue, a general review of the state of the art in optical interconnects for hybrid platform photonic integrated circuits is analyzed, which results in the selection of a vertical transmission via

spot size converter tapers in the Device Selection block. Afterwards, a theoretical study of a linear taper is performed. By analyzing the linear taper size, we propose some device requirements: all power must be transmitted from one platform to another, bidirectionally (loss should only be perceived due to the material), the device size must be reduced, and it must overcome loss due to lateral misalignment. Using notions from the coupled mode theory (CMT in orange blocks), the fabrication constraints for TFPS and SOI platforms and the possible hybrid platform interface and bonding technology, we propose non-linear taper designs which can meet all requirements. Results are presented in the final section.

5.2 State of the Art for Optical Interconnects

Good quality for optical interconnects, for application in TOSA, is measured in power efficiency, bandwidth of operation and mechanical stability. In this section, a revision of interconnection technologies is presented. From active devices fabricated in III-V platform, passive components in silicon-on-insulator, silica fiber and electrooptic polymer modulator.

5.2.1 Lens Array

Ohyama *et al.* [107] proposed a TOSA with a V_{pp} of 1.5 V. They achieved an error of about 10^{-13} at transmission distances of 40 km over single mode fiber (SMF). The total size was 8.7 mm $\times$ 28.7 mm $\times$ 6.5 mm. It used an array of four electroabsorption modulator integrated distributed feedback (EADFB) lasers to achieve 25 Gb/s per lane. They used two sets of EADFB laser arrays in two chips, combined the light of two lanes with 2×1 MMI couplers on chip and then combined the light of the two chips with a polarization beam combiner (PBC). This setup requires sub-micron alignment accuracy [135] which extends the TOSA assemble process as a result of high-power laser for alignment purposes. The lenses coupling loss was designed to be in the order of -3 dB.

To avoid additional process in lens alignment, [136] proposes a passive approach by using lens-integrated surface-emitting laser. They integrate monolithically a 45° total reflection mirror and lens into a distributed feedback (DFB) laser. This model was designed to achieve a coupling efficiency of -1.46 dB with no deviation. Nevertheless, experimentally, -5 dB was achieved considering ± 1.5 μm misalignment shift.

These approaches, while suitable for very compact transmitter optical subassemblies, remain greatly affected by misalignment problems.

5.2.2 III-V to SOI

Vertical-cavity surface emitting-lasers (VCSEL) constitute a well-discussed option for immediate integration with silicon-on-insulator platform, by fabricating silicon

gratings [25] or by depending on very precise alignment [68].

Hybrid III-V/SOI lasers were also proposed [22, 23, 69]. They used the supermode approach, which consists of a system composed of an amplifying waveguide (III-V) coupled with a passive interconnection waveguide (SOI) for effective inter-platform integration.

Lastly, epitaxial growth [24, 25, 137, 138] of GaAs, InP or Ge on silicon was used to overcome alignment problems if approached by another bonding technique. This way very short interconnections were realized.

5.2.3 Fiber to SOI and vice versa

Grating couplers have demonstrated losses of 0.58 dB for half-width bands (−3 dB) up to 70nm in 1550nm [139]. Recently, new devices with complex geometries were proposed to overcome the fiber positioning challenge by emitting in the vertical direction. Tseng *et al.* [140] achieved −1.46 dB in the 1310nm window with about 20 nm within the −3 dB band by using partially and perfectly reflecting mirrors at both ends of their grating. In the 1550nm window, Liu *et al.* achieved a coupling efficiency of 28.5%, albeit with a much planar response. 1dB mark is at 38nm for grating coupler that uses a tilted membrane structure to couple light vertically [141].

Alternatively, spot-size converter tapers offer a more planar response over wavelength than gratings. However, they may also involve the tradeoff of a significant footprint. In [142] edge inverted-taper couplers ranging from 690 μm to 4370 μm in length were presented. They measured 0.7 dB of coupling efficiency and simulated up to 0.2 dB.

Polymer to SOI and vice versa

Using polymer as an intermediate layer to interconnect fiber and SOI, Pu *et al.* [143] proposed a compact taper of 300 μm. Losses of 0.36 dB and 0.66 dB were demonstrated for TM and TE, respectively. To achieve such results, they employed to thermal oxidation of silicon oxide on top of the silicon taper. After oxidation, they estimated a tapered tip of approximately 12 nm which requires fine control over the fabrication process.

Considering fabrication limitations, in [27], Soganci *et al.* proposed tapers with 75 nm tips, which can be achieved by any commercial foundry. They presented losses of 1 dB in a length of 700μm. The effect caused by lateral misalignment of 2μm was $\sim$ 0.6 dB for TE and $\sim$ 0.3 dB for TM.

5.3 EO polymer modulator and SOI interface

At chip level, MZ EO polymer modulators already described in Chapter 3 have electro-optic bandwidths beyond 100 GHz [144, 145]. Complex modulation formats were already demonstrated [41, 146] to achieve even higher speeds. Additionally, EO polymer modulators work with transverse magnetic (TM) polarized light for good optical/electrical mode overlap (see gold electrodes and inverted rib in Fig. 5.3), which prompts the use of optical passive circuitry and creates a hybrid integrated device scenario in which optical intra-chip interconnection losses are relevant for the general performance of the transmission system [41, 68].

Previous efforts using passive polymer chip interconnects include butt coupling [147, 148]. Silicon-on-insulator devices have been widely known and are the best for efficiency, integration, bandwidths around 80 nm and rotation losses up to −0.5 dB [28, 72, 149].

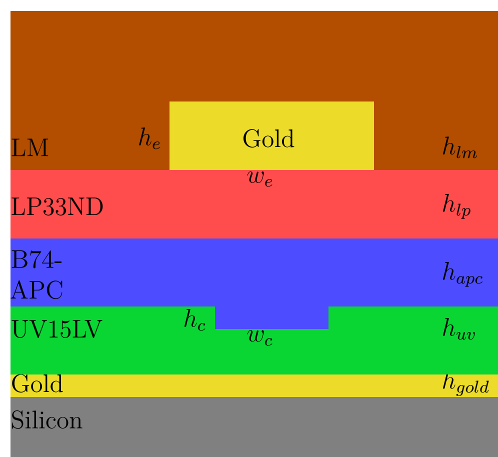

Figure 5.3: Cross section of the active region of the polymer Mach-Zehnder modulator [45]. Gold trace is at the top of the polymer layers and velocity matching material (LM) is also shown.

In this section we propose a taper based on mode coupling theory to interconnect polymer on silicon and silicon-on-insulator chips. This proposal is based in the distance between the polymer core trench and the polymer cladding, h_{apc} (see Fig. 5.3). Hybrid chip disposition inside a package is suggested in Fig. 5.4; for better clarity we divided the packaging disposition into five stages:

- SOI platform is the silicon-on-insulator platform where passive circuitry can be located.
- Transition is the proposed flip-chip interconnection between SOI platform and the electrooptic polymer chip.

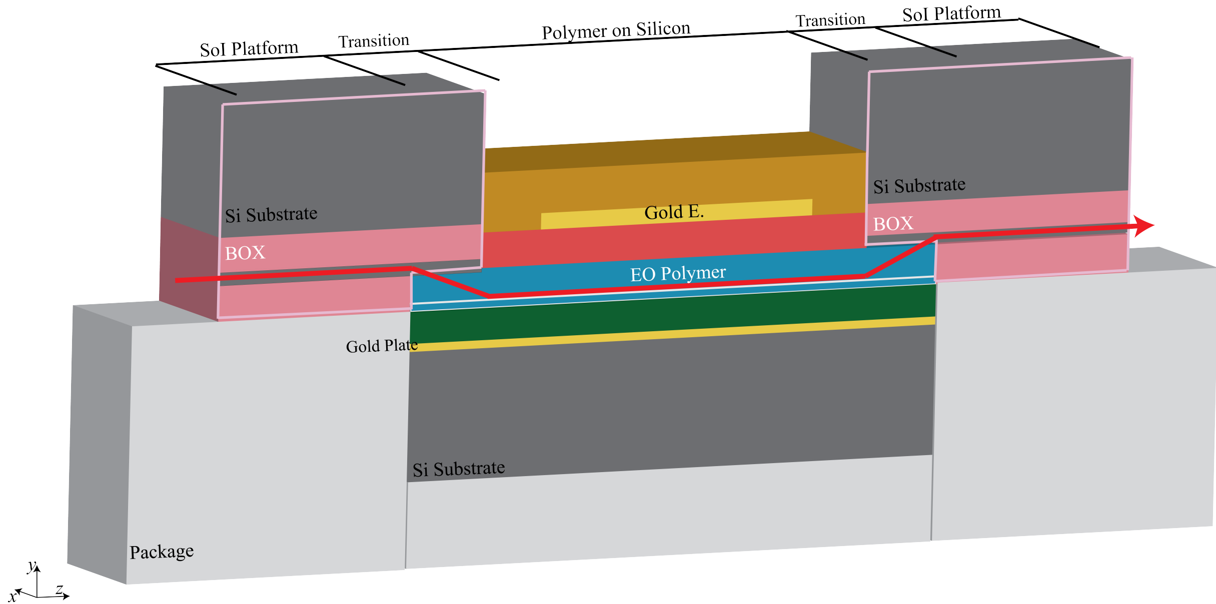

Figure 5.4: Longitudinal cut of the proposed silicon-on-Insulator platform interconnection at the input and output of an EO polymer modulator die. Red arrow indicates path of light. SOI platform, taper transition and polymer-on-silicon platform stages are shown. At the transition, spot size is converted through an adiabatic taper. Geometries are not to scale.

- Polymer on silicon chip is the TFPS platform where the EO polymer modulator is located. Gold electrode represents the active region where modulation is performed.
- Transition and SOI platform at the output of the chip is proposed for passive output circuitry.

The first challenge that this device encounters is that flip-chip [150] technology alignment precision is around 1 μm [25, 137, 151]. To overcome power compromises due to misalignment problems, we propose a specific non-linear taper to try and overcome linear tapers inefficiency [27, 152] in this matter.

As a first approach of the viability of the silicon taper interconnection device, we let the polymer waveguide depicted in Fig. 5.3 leave out LP33ND and LM polymer layers as well as the top gold, which is present only in the arms of the Mach-Zehnder. This way, a cladding-less silicon waveguide can be brought close as shown in Fig. 5.5.

5.4 Coupling analysis

Coupling mode theory analyzes how energy is transfered from one waveguide to another when the two are brought into proximity [153]. Appendix 1 details the set of equations and solution for the coupling mode theory of any two waveguides on an homogeneous medium.

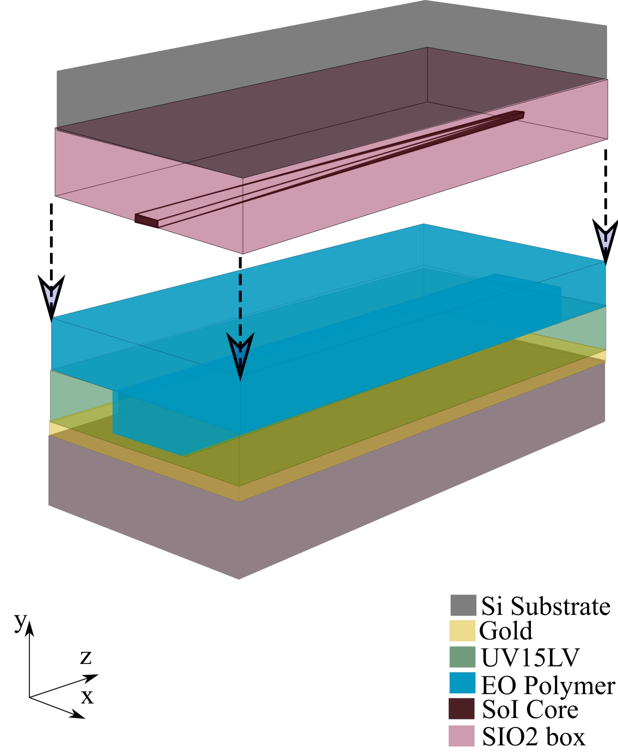

Figure 5.5: Transition between the EO polymer modulator waveguide and SOI taper.

Let us define, by using mode-coupling theory terminology, the perturbed and unperturbed geometries for the SOI and polymer inverted rib waveguides.

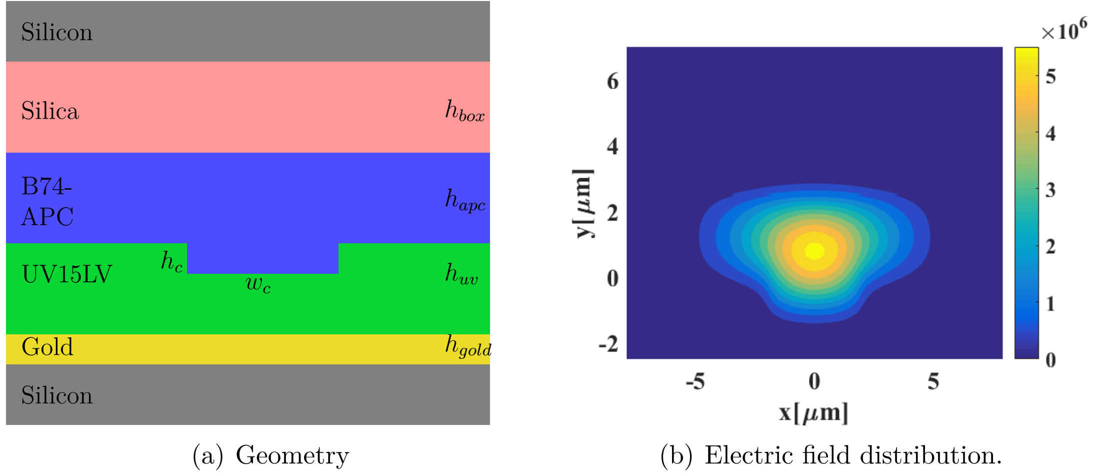

(a) Geometry

(b) Electric field distribution.

Figure 5.6: First unperturbed problem: Polymer waveguide with glass cladding.

The first unperturbed problem is defined by the polymer modulator waveguide with the silicon-on-insulator waveguide core removed as shown in Figure 5.6. Silicon substrates are around 625 μm, while $h_{uv} = 2.5$ μm, $h_{apc} = 2.5$ μm, $h_c = 1$ μm, $w_c = 3.8$ μm, $h_{box} = 2$ μm, $h_{gold} = 1$ μm. Refractive indexes and optical losses for used polymers are $n_{APC} = 1.67$ and $k_{APC} = 1.2$ dB/cm, $n_{UV} = 1.505$ and $k_{UV} = 1.2$ dB/cm [45]. The solution for this problem is an effective index of $n_{eff,p} = 1.655$ and 1.37 dB/cm loss.

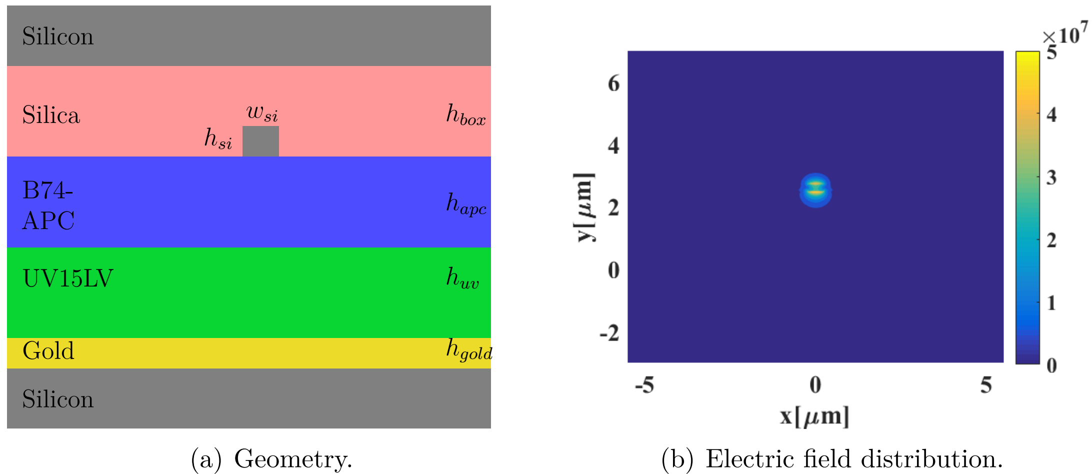

(a) Geometry.

(b) Electric field distribution.

Figure 5.7: Second unperturbed problem geometry: Silicon waveguide with polymer cladding.

Let us define the second unperturbed problem as the silicon waveguide with the polymer trench removed as shown in Figure 5.7. When making $h_{si} = 0.22$ μm and $w_{si} = 0.45$ μm, which are the standard monomode propagation dimensions for SOI, we get $n_{eff,si} = 1.867$ and loss 0.82 dB/cm. Since the solutions of both isolated waveguides are distant from each other, let us solve the problem for varying values of SOI waveguide width w_{si} while w_c =3.8 μm. The results are shown in Figure 5.8. Isolated waveguide solutions are matched for w_{si} =0.19 μm and 0.22 μm for TE and TM modes, respectively.

Following the coupled mode theory methodology, both solutions must travel in the same direction, when brought into proximity one waveguide must be affected very little by the other (falling into a quasi-orthogonal regime), while their coupling coefficient should be inversely proportional to he total coupling length [153].

Lastly, the perturbed problem is shown in Figure 5.9 which is the geometry of interest. As both waveguides are into proximity, let us consider one supermode in Fig. 5.10 for the quasi-TM polarization. Note that $w_{si} = 0.23\mu$m was chosen to fulfill the $\Delta n_{eff} = 0$ condition. The supermode with $n_{eff} = 1.6531$ can be identified as antisymmetric, given that is slightly less than $n_{eff,p}$. The behavior in Fig. 5.10 favors the approximated orthogonality relationship between waveguides. This approximation together with the fact that the difference between effective refractive indexes approaches zero justifies that these waveguides are capable of interchanging energy over a specific propagation length.

5.5 Optimized Silicon Taper

Typical length for achieving a π phase between the two arms of a MZ polymer modulator is around $L_\pi = 5$ mm and up [45], which results in relatively big footprint. Hence, it is important to reduce the taper length (see Fig. 5.5) for integration purposes and also to deal with the intrinsic material losses. With this goal in mind, complex geometry

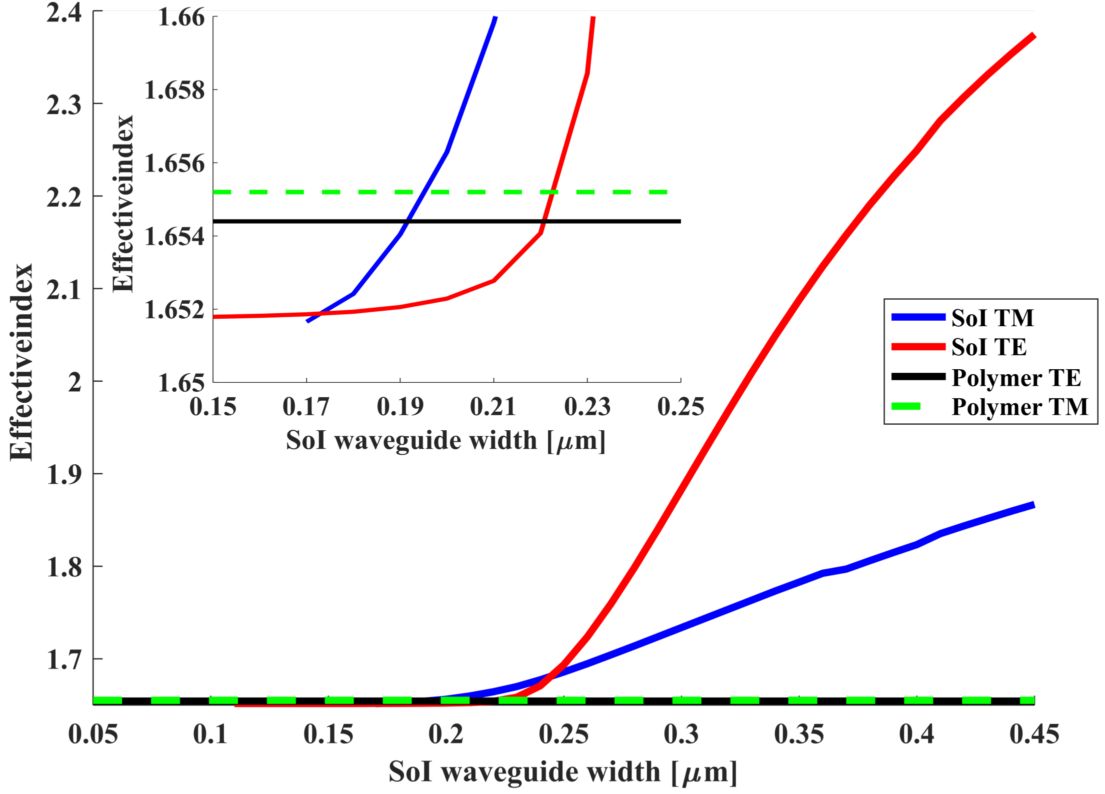

Figure 5.8: Silicon waveguide modal analysis as a function of its width (w_{si}) at $\lambda = 1550$nm. Inset shows a detail of the region of intersection between effective indexes.

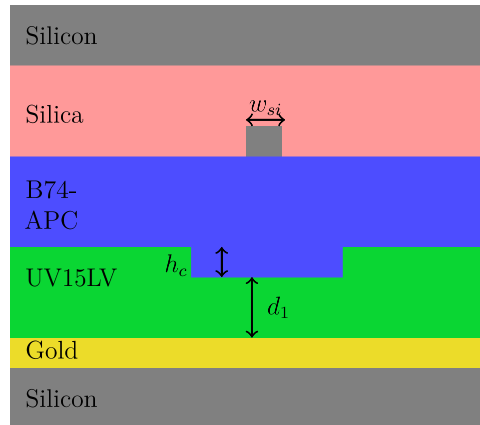

Figure 5.9: Perturbed problem: Silicon and polymer waveguides in close proximity.d_1 is the distance between the bottom metalization and the polymer core.

tapers such as segmented waveguides [154], and linear tapers [27] can be used. This work will focus on the design of a non-linear taper to overcome misalignment sensitivity and polymers intrinsic losses at 1550 nm.

5.5.1 Linear Taper Design

Consider a linear taper, where the silicon core width varies from $w_{si,i}$ =0.075 μm (port 1) to $w_{soi,f}$ =0.45 μm (port 2) linearly over the taper length (L_c) as shown in

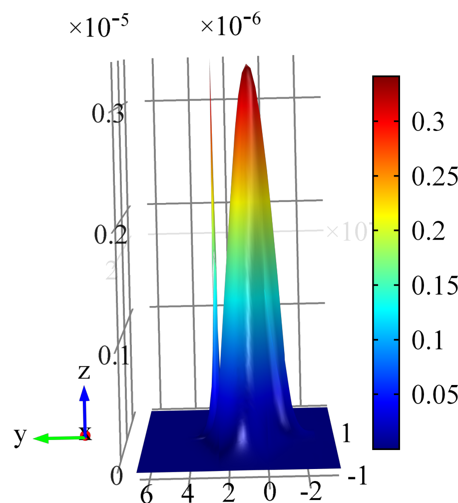

Figure 5.10: Antisymmetric supermode magnetic field distribution. Quasi-TM mode of SOI and polymer waveguides when brought into close proximity. λ = 1550 nm and $\Delta n_{eff} \approx 0$.

Figure 5.11. The polymer core width is fixed at w_c =3.8 μm over the whole taper length. As silicon is transparent in the 1550 nm window, it is important to consider the losses introduced by the polymer waveguide and the gold film in our calculations.

Gold film, in the polymer MZ modulator of Figure 5.3, is d_1 =1.5 μm apart from the polymer core. However, according to [45], we still have some range for h_c and d_1 values that could be useful for coupling purposes in this device. Figure 5.12 shows that losses increase while d_1 decreases due to the gold plate proximity. When there is no gold plate ($d_1 \Rightarrow \infty$), transmittance reaches its peak of -0.12dB at 1000 μm. The case when d_1 =1.5 μm and h_c =1 μm only differs 0.01 dB from the latter. Likewise, as h_c increases, the maximum peak shifts towards the right even as d_1 increases. Material losses are represented in the quasi-linear decay of the transmittance after it has reached its coupling peak. A hypothetical case when d_1 =0.5 μm is represented here for further illustrate the loss due to the gold plate.

In Figure 5.13 a lateral offset of the silicon taper is considered. When L_c >1000 μm, all curves converge indicating that the taper response remains unaffected by misalignment effects up to 1.8 μm. On the other hand, let us consider a 277 μm long linear taper. The maximum power transmitted is -1.037 dB, although 0.5 μm of alignment shift does not dramatically affect the taper response, if the taper position is shifted by 1.8 μm, power decreases by 1.04 dB. Taken together, these results seem to suggest that a linear silicon taper is very sensitive to misalignment problems unless it is significantly long. When added to an already long polymer modulator chip, it may result in integration inefficiency. Alternatively, choosing to implement smaller linear tapers could result in transmitted power inefficiency.

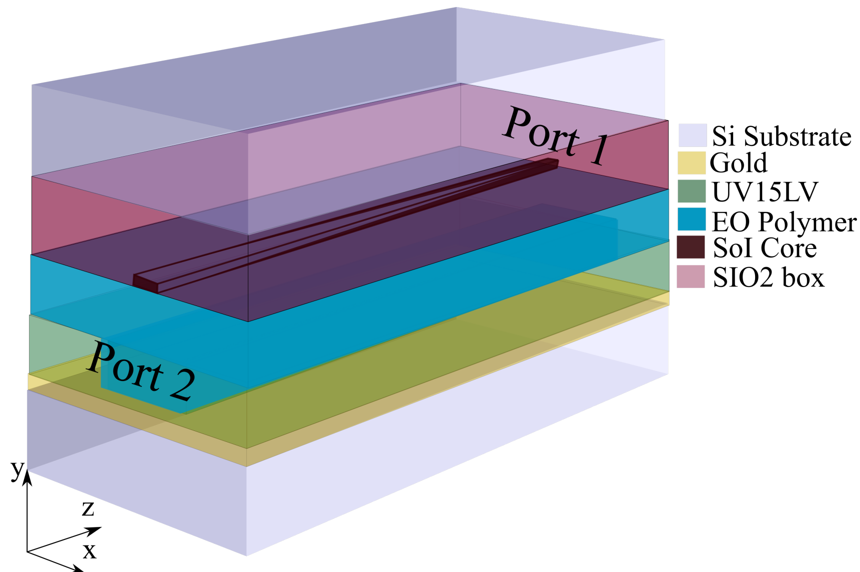

Figure 5.11: Hybrid Silicon Taper geometry showing port identification. Port 1 refers to polymer TM mode and Port 2 is silicon core waveguide TM mode.

5.5.2 Non-linear Taper Design

The proposed non-linear taper uses the effective index variation obtained by the analysis of the unperturbed problems, shown in Figure 5.8 as an important aid to optimize the taper length. Let us divide the taper into 10 continuous sections as depicted in Figure 5.14, where $w_{si,f} = 0.45$ μm and $w_{si,i} = 0.075$ μm. Each section has a fixed initial and final width as shown in Table 5.1.

Table 5.1: 10 Segment Maximum values and taper widths.

S	w_i [μm]	w_f [μm]	Local Max.[dB]	Length [μm]
1	0.0750	0.1125	-5.900	54
2	0.1125	0.1500	-5.600	54
3	0.1500	0.1875	-4.710	55
4	0.1875	0.2250	-0.908	64.5
5	0.2250	0.2625	-1.948	25.5
6	0.2625	0.3000	-4.434	10.5
7	0.3000	0.3375	-5.566	5.5
8	0.3375	0.3750	-6.077	3.5
9	0.3750	0.4125	-6.084	3
10	0.4125	0.4500	-6.220	2

Using Lumerical Mode Eigenmode Expansion solver [155] we performed an optimization by linearly varying each section length from 1 μm to 300 μm. For one varying segment length (in the Z direction), the others were fixed at 5 μm, this way the effect of each segment length in the total transmitted power was observed (see Fig. 5.15). Segment 4 is fairly relevant, with the first maximum -0.908 dB at 64.5 μm. Another important segment is number 5 with its first maximum value at 25.5 μm, transmitting

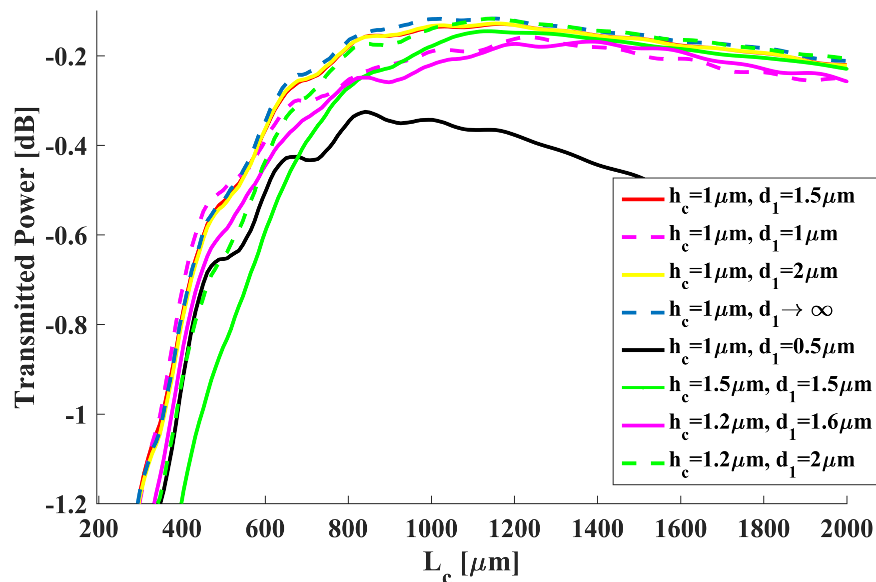

Figure 5.12: Normalized Output power as a function of the linear variation of the taper length in micrometers. Presence of 1 μm gold thin film is evaluated by varying polymer waveguide height (h_c) and distance to the core d_1.

$-1.948dB$. Note that both segments initial and final widths are in the vicinity of $\Delta n \approx 0$ calculated in Figure 5.8 for the TM mode. Segments 3 and 6 from Fig. 5.15, although not as predominant as segments 4 and 5, could potentially aid to the curve smoothness. Segments 7 and forward have a periodic behavior around the initial point (2 μm), which led us to minimize these segments' length as much as possible without compromising the taper smoothness to avoid backscattering.

First local maximums values listed in Table 5.1 will be considered to build minimum length possible non-linear tapers to avoid further loss caused by polymer materials.

From the linear taper offset analysis (see Fig. 5.13) we can see that length is a determining factor not only for coupling efficiency but also for alignment robustness. In this regard, we decided to build two non-linear tapers as detailed in Table 5.2 and evaluate their behavior when submitted to alignment shift. Although segment 5 influence in the transmitted power is not as significant as segment 4. Taper 1 uses the local maximum length of segments 3, 4, 5 and 6 to fabricate a device that is 179.5μm long. For Taper 2 we chose an smoother approach by using the local maximum values of segments 1 and 2, which are 54μm each.

As seen in Figure 5.16, at a wavelength of 1550 nm, we got a decay of 0.3 dB from no misalignment to 1.8 μm. Taper 2 is a 277.5 μm long device, and it offers an almost planar response, albeit its maximum (-0.23 dB) does not reach Taper 1's. From an alignment shift of 1.5 μm and up, there is a trade-off between maximum power and misalignment robustness that can be considered when working with different alignment

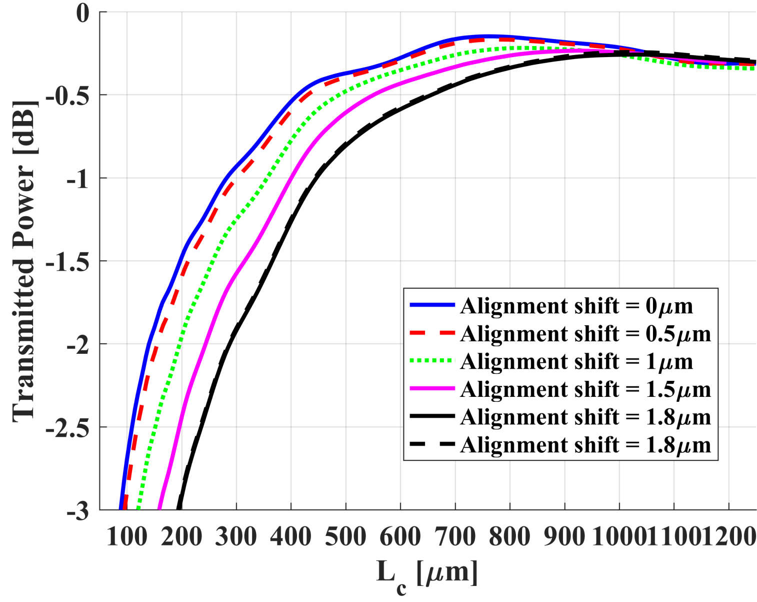

Figure 5.13: Normalized output power as a function of the linear variation of the taper length in micrometers. Silicon taper offset along the x axis from 1 μm to 1.8 μm is considered. TM mode.

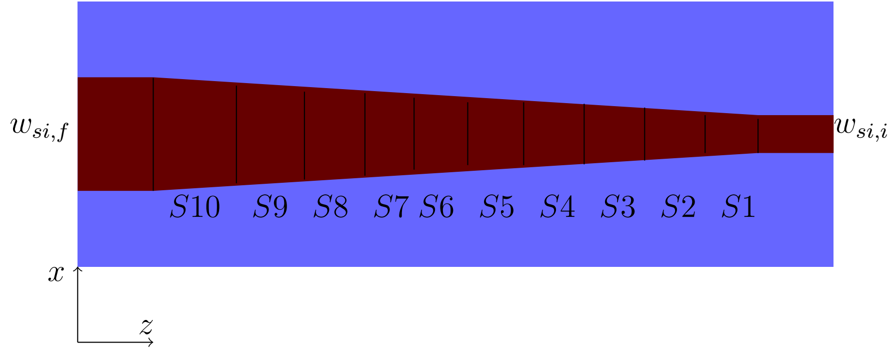

Figure 5.14: Sectioning of the silicon taper over a polymer slab.

techniques. In comparison, linear tapers with the same length as Tapers 1 and 2 offer maximum transmitted power of -1.7dB and -1dB, respectively. Also, they are much more sensitive to misalignment.

Closing in the ends of the C-band, let us define $\lambda_1 = 1520$ nm and $\lambda_2 = 1570$ nm. Fig. 5.17 shows that Taper 2 has a more robust response to lateral misalignment shift, especially towards 1570 nm. At 1520 nm, Taper 1 goes from -0.13 dB to -0.64 dB, while Taper 2 goes from -0.19 dB to -0.54 dB. Overall, if a proper alignment is guaranteed up to 1 μm, then Taper 1 should suffice to get an insertion loss better than -0.33 dB in the whole band. However, if the alignment shift is greater than 1 μm, then Taper 2 is enough to get a transmission better than -0.54 dB in the C-band.

Figure 5.18 shows a comparison between linear and non-linear tapers with no misalignment. Left end is the SOI waveguide with $w_{si,f} = 0.45$ μm and the right end

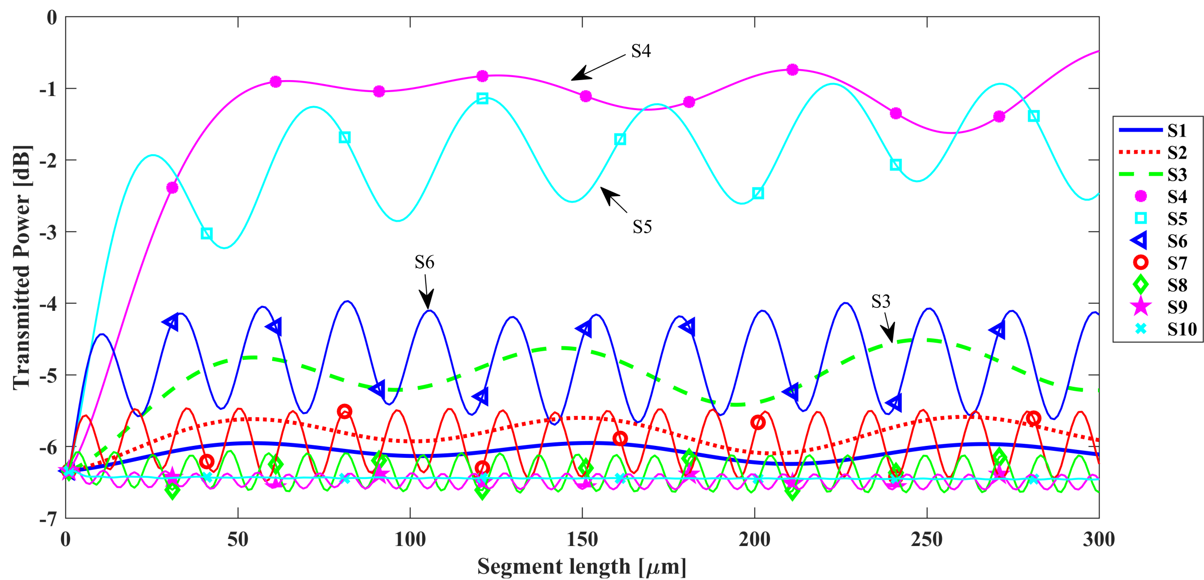

Figure 5.15: Length variation of each 10 sections of the SOI taper.

Table 5.2: Optimized non-linear tapers details.

S	Taper1 Length [μm]	Taper2 Length [μm]
1	5	54
2	5	54
3	55	55
4	64.5	64.5
5	25.5	25.5
6	10.5	10.5
7	5.5	5.5
8	3.5	3.5
9	3	3
10	2	2
Taper length	179.5	277.5

is only the inverted rib polymer waveguide (matching Fig. 5.6). There is a noticeable smooth transition of the electric field in the non-linear taper, while power in the linear taper begins transitioning about half-way through the length.

5.6 Summary

In this chapter an optimized multi-platform interconnection taper was proposed for coupling light between a MZ polymer modulator waveguide to a silicon on insulator platform. We achieved power transmission of ~ -0.13 dB and ~ -0.23 dB from 179.5 μm and 277.5 μm long tapers, respectively. When considering taper offset due to alignment problems up to 1.8 μm, only 2% of the transmittance is affected when using the largest

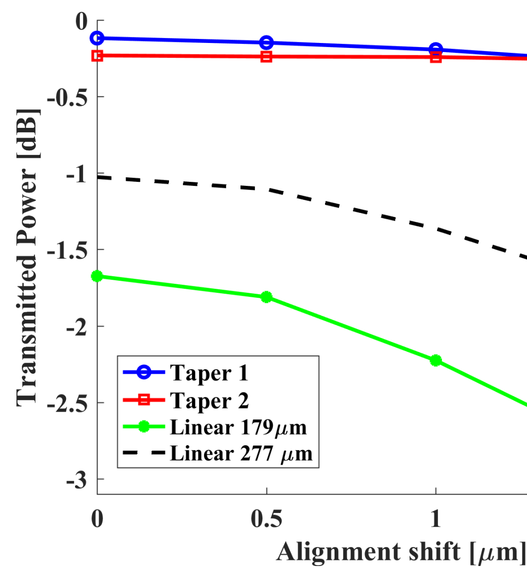

Figure 5.16: Alignment shift effect comparison between linear and non-linear silicon tapers.

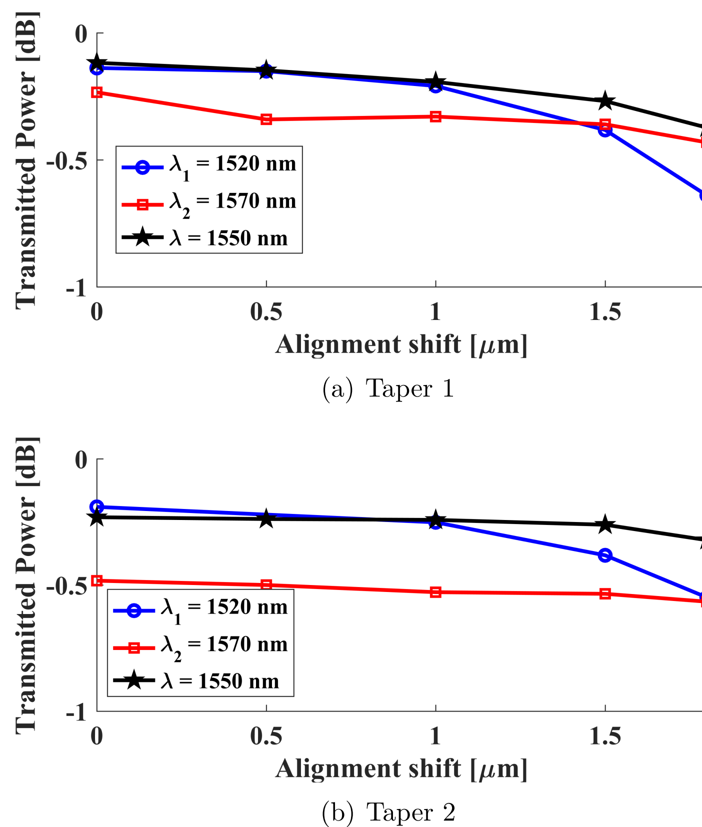

Figure 5.17: Alignment shift effect due to wavelength in the C-band. Taper 1 is 179.5μm long and Taper 2 is 277.5μm long.

taper. The coupled mode theory approach for spot size converter tapers is compact, robust and its low loss has the potential to make it ideal for packaging applications.

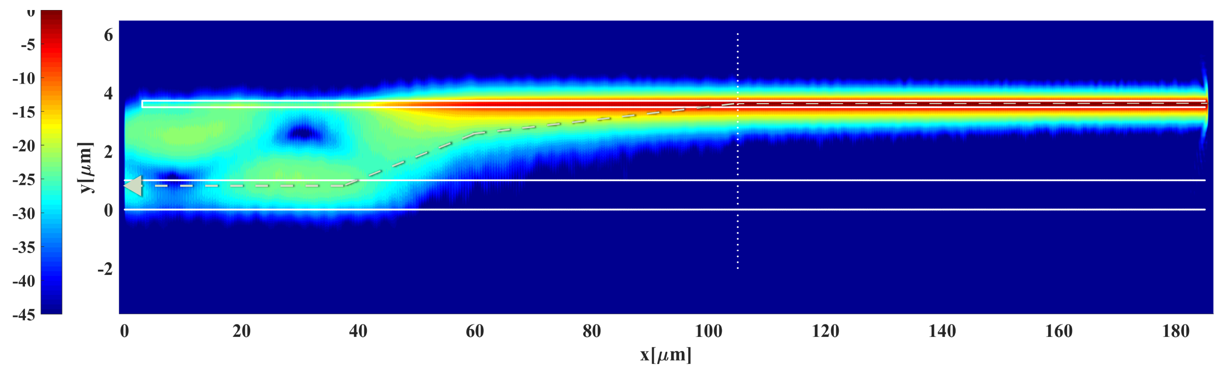

(a) Linear taper

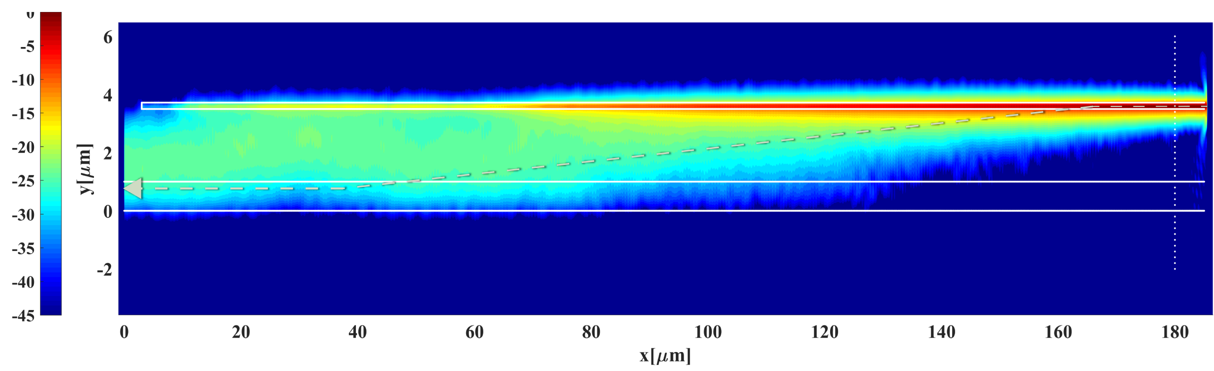

(b) Non-linear: Taper 1

Figure 5.18: X-normal cut of the electric field distribution at 1550 nm for (a) linear and (b) non-linear tapers. Both are 179.5μm long. White lines contour the waveguide polymer (0 to 1μm) and SOI (3.5 to 3.72μm) cores, while dotted line indicates the approximate beginning of the power transition. Dashed arrow shows the direction of propagation.

Chapter 6

Conclusion

In this thesis, a methodology for designing transmitter optical sub-assemblies packaging was presented. This methodology consists in designing the RF and optical sub-assemblies together with the TFPS chip as active parts that interchange information between them to improve the electrooptical characteristics of the whole system. For this purpose, the work was divided into five chapters. Chapter 1 presents the general introduction to the work. Chapter 2 is a brief revision of general concepts that was further developed and applied in the following chapters.

Chapter 3 analyses the basic design of an TFPS modulator with the intention of proposing RF and optical interconnects to fabricate transmitter optical sub-assemblies. For this purpose each element of the electrical path was analyzed and considered as a conforming block of the packaging system design. Electrooptic response and V_π were also calculated.

In chapter 4 a wide band RF interconnection for a TFPS modulator was proposed. Return loss of the whole system, including chip plus ceramic electrical path, was kept well bellow OIF recommendations, while the electrooptic response resulted in a band of 22.2 GHz.

In chapter 5 an optimized multi-platform interconnection taper was proposed for coupling light between a MZ polymer modulator waveguide to a silicon-on-insulator platform. We achieved transmissions of -0.13 dB and -0.23 dB from 179.5 μm and 277.5 μm long tapers, respectively.

This thesis also encompasses the following contributions in the electrooptic packaging field design:

- A per-device electromagnetic simulation of two kinds of TFPS electrooptical modulator interconnected with high speed ceramic based RF path for feeding and termination.

- Electro-thermal and electromagnetic simulation of heaters on a TFPS electrooptical

modulator considering temperature interference between the two arms of the Mach-Zehnder.

- A compact and high performance spot size converter to interconnect light from a TFPS platform to a silicon-on-insulator platform in the context of a high performance hybrid transmitter optical subassembly system.

Bibliography

[1] P. J. Winzer, "Scaling optical fiber networks: Challenges and solutions," *Optics and Photonics News*, vol. 26, no. 3, pp. 28–35, 2015.

[2] C. Laperle and M. O'Sullivan, "Advances in high-speed dacs, adcs, and dsp for optical coherent transceivers," *Journal of Lightwave Technology*, vol. 32, no. 4, pp. 629–643, 2014.

[3] F. N. Khan, K. Zhong, W. H. Al-Arashi, C. Yu, C. Lu, and A. P. T. Lau, "Modulation format identification in coherent receivers using deep machine learning," *IEEE Photonics Technology Letters*, vol. 28, no. 17, pp. 1886–1889, 2016.

[4] N. K. Fontaine, R. Ryf, H. Chen, A. V. Benitez, J. A. Lopez, R. A. Correa, B. Guan, B. Ercan, R. P. Scott, S. B. Yoo, *et al.*, "30× 30 mimo transmission over 15 spatial modes," in *Optical Fiber Communications Conference and Exhibition (OFC), 2015*, pp. 1–3, IEEE, 2015.

[5] P. J. Winzer, , and R. J. Essiambre, *Optical Fiber Telecommunications V-B: Systems and Networks.* Academic Press: Burlington, 2008.

[6] A. Vahdat, H. Liu, X. Zhao, and C. Johnson, "The emerging optical data center," in *Optical Fiber Communication Conference*, p. OTuH2, Optical Society of America, 2011.

[7] N. Eiselt, J. Wei, H. Griesser, A. Dochhan, M. Eiselt, J.-P. Elbers, J. J. V. Olmos, and I. T. Monroy, "First real-time 400g pam-4 demonstration for inter-data center transmission over 100 km of ssmf at 1550 nm," in *Optical Fiber Communications Conference and Exhibition (OFC), 2016*, pp. 1–3, IEEE, 2016.

[8] J. Geyer, C. Doerr, M. Aydinlik, N. Nadarajah, A. Caballero, C. Rasmussen, and B. Mikkelsen, "Practical implementation of higher order modulation beyond 16-qam," in *Optical Fiber Communications Conference and Exhibition (OFC), 2015*, pp. 1–3, IEEE, 2015.

[9] G. Liga, A. Alvarado, E. Agrell, and P. Bayvel, "Information rates of next-generation long-haul optical fiber systems using coded modulation," *Journal of Lightwave Technology*, vol. 35, no. 1, pp. 113–123, 2017.

[10] R. Rios-Müller, J. Renaudier, H. Mardoyan, A. Konczykowska, F. Jorge, B. Duval, J.-Y. Dupuy, *et al.*, "Multi-dimension coded pam4 signaling for 100gb/s short-reach transceivers," in *Optical Fiber Communication Conference*, pp. Th1G–4, Optical Society of America, 2016.

[11] P. Groumas, Z. Zhang, V. Katopodis, A. Konczykowska, J. Dupuy, A. Beretta, A. Dede, J. Choi, P. Harati, F. Jorge, *et al.*, "Tunable 100 gbaud transmitter based on hybrid polymer-to-polymer integration for flexible optical interconnects," *Journal of Lightwave Technology*, vol. 34, no. 2, pp. 407–418, 2016.

[12] A. Chiuchiarelli, S. M. Rossi, V. N. Rozental, G. C. Simoes, L. H. Carvalho, J. C. Oliveira, J. R. Oliveira, and J. D. Reis, "50-ghz+ thin-film polymer on silicon modulator for pam4 100g-per-wavelength long-reach data center interconnects," in *ECOC 2016; 42nd European Conference on Optical Communication; Proceedings of*, pp. 1–3, VDE, 2016.

[13] I. Std, "P802.3ba 40gb/s and 100gb/s ethernet task force url, 19th june 2010," *IEEE P802.3ba 40Gb/s and 100Gb/s Ethernet Task Force URL http://www.ieee802.org/3/ba/.*

[14] C. The optical internetworking forum, 48377 Fremont Blvd, "Oif tech opticons 400g, july 2015," *http://www.oiforum.com/wp-content/uploads/OIF-Tech-Options-400G-01.0.pdf.*

[15] M. P. Yankov, D. Zibar, K. J. Larsen, L. P. Christensen, and S. Forchhammer, "Constellation shaping for fiber-optic channels with qam and high spectral efficiency," *IEEE Photonics Technology Letters*, vol. 26, no. 23, pp. 2407–2410, 2014.

[16] D. Korn, C. Koos, L. Alloati, D. Hillerkuss, J. Li, A. Barklund, R. Dinu, J. Wieland, M. Fournier, J. Fedeli, H. Yu, W. Bogaerts, P. Dumon, R. Baets, W. Freude, and J. Leuthold, "Silicon-organic hybrid iq modulator for 16qam at 112gb/s," in *CLEO Europe*, 2013.

[17] T. L. Koch and U. Koren, "Photonic integrated circuits," *AT&T Technical Journal*, vol. 71, no. 1, pp. 63–74, 1992.

[18] M. Smit, X. Leijtens, H. Ambrosius, E. Bente, J. van der Tol, B. Smalbrugge, T. de Vries, E.-J. Geluk, J. Bolk, R. van Veldhoven, L. Augustin, P. Thijs, D. D'Agostino, H. Rabbani, K. Lawniczuk, S. Stopinski, S. Tahvili, A. Corradi,

E. Kleijn, D. Dzibrou, M. Felicetti, E. Bitincka, V. Moskalenko, J. Zhao, R. Santos, G. Gilardi, W. Yao, K. Williams, P. Stabile, P. Kuindersma, J. Pello, S. Bhat, Y. Jiao, D. Heiss, G. Roelkens, M. Wale, P. Firth, F. Soares, N. Grote, M. Schell, H. Debregeas, M. Achouche, J.-L. Gentner, A. Bakker, T. Korthorst, D. Gallagher, A. Dabbs, A. Melloni, F. Morichetti, D. Melati, A. Wonfor, R. Penty, R. Broeke, B. Musk, and D. Robbins, "An introduction to inp-based generic integration technology," *Semiconductor Science and Technology*, vol. 29, no. 8, p. 083001, 2014.

[19] J. Eng and C. Kocot, *Optical Fiber Telecommunications VIA: Chapter 14. VCSEL-Based Data Links.* Optics and Photonics, Elsevier Science, 2013.

[20] E. J. M. A. Chen, *Broadband Optical Modulators.* CRC Press, 2012.

[21] M. Streshinsky, A. Ayazi, Z. Xuan, A. E.-J. Lim, G.-Q. Lo, T. Bachr-Jones, and M. Hochberg, "Highly linear silicon traveling wave mach-zehnder carrier depletion modulator based on differential drive," *Optics Express*, vol. 21, no. 3, 2013.

[22] A. Yariv and X. Sun, "Supermode si/iii-v hybrid lasers, optical amplifiers and modulators: A proposal and analysis," *Optics express*, vol. 15, no. 15, pp. 9147–9151, 2007.

[23] X. Sun and A. Yariv, "Engineering supermode silicon/iii-v hybrid waveguides for laser oscillation," *JOSA B*, vol. 25, no. 6, pp. 923–926, 2008.

[24] S.-W. Seo, S.-Y. Cho, and N. M. Jokerst, "A thin-film laser, polymer waveguide, and thin-film photodetector cointegrated onto a silicon substrate," *IEEE photonics technology letters*, vol. 17, no. 10, pp. 2197–2199, 2005.

[25] Y. Wang, S. Djordjecvic, J. Yao, J. Cunningham, X. Zheng, A. V. Krishnamoorthy, M. Muller, M.-C. Amann, R. Bojko, N. A. Jaeger, *et al.*, "Vertical-cavity surface-emitting laser flip-chip bonding to silicon photonics chip," in *Proceedings of IEEE Optical Interconnects Conference*, pp. 122–123, 2015.

[26] E. A. Marcatili, "Dielectric rectangular waveguide and directional coupler for integrated optics," *Bell Labs Technical Journal*, vol. 48, no. 7, pp. 2071–2102, 1969.

[27] I. M. Soganci, A. La Porta, and B. J. Offrein, "Flip-chip optical couplers with scalable i/o count for silicon photonics," *Optics express*, vol. 21, no. 13, pp. 16075–16085, 2013.

[28] A. Cutolo, M. Iodice, A. Irace, P. Spirito, and L. Zeni, "An electrically controlled bragg reflector integrated in a rib silicon on insulator waveguide," *Applied physics letters*, vol. 71, no. 2, pp. 199–201, 1997.

[29] J. Leuthold, C. Koos, W. Freude, L. Alloatti, R. Palmer, D. Korn, J. Pfeifle, M. Lauermann, R. Dinu, S. Wehrli, *et al.*, “Silicon-organic hybrid electro-optical devices,” *IEEE Journal of Selected Topics in Quantum Electronics*, vol. 19, no. 6, pp. 114–126, 2013.

[30] L. Alloatti, R. Palmer, S. Diebold, K. P. Pahl, B. Chen, R. Dinu, M. Fournier, J.-M. Fedeli, T. Zwick, W. Freude, *et al.*, “100 ghz silicon–organic hybrid modulator,” *Light: Science & Applications*, vol. 3, no. 5, p. e173, 2014.

[31] R. Palmer, L. Alloatti, D. Korn, P. C. Schindler, M. Baier, J. Bolten, T. Wahlbrink, M. Waldow, R. Dinu, W. Freude, *et al.*, “Low power mach–zehnder modulator in silicon-organic hybrid technology,” *IEEE Photonics Technology Letters*, vol. 25, no. 13, pp. 1226–1229, 2013.

[32] D. Jin, H. Chen, A. Barklund, J. Mallari, G. Yu, E. Miller, and R. Dinu, “Eo polymer modulators reliability study,” in *Proc. SPIE*, vol. 7599, p. 75990H, 2010.

[33] J. Mallari, C. Wei, D. Jin, G. Yu, A. Barklund, E. Miller, P. O’Mathuna, R. Dinu, A. Motafakker-Fard, and B. Jalali, “100gbps eo polymer modulator product and its characterization using a real-time digitizer,” in *Optical Fiber Communication (OFC), collocated National Fiber Optic Engineers Conference, 2010 Conference on (OFC/NFOEC)*, pp. 1–3, IEEE, 2010.

[34] Y. Kutuvantavida, G. V. Williams, M. D. H. Bhuiyan, S. G. Raymond, and A. J. Kay, “Effects of chromophore conjugation length and concentration on the photostability of indoline-based nonlinear optical chromophore/polymer films,” *The Journal of Physical Chemistry C*, vol. 119, no. 6, pp. 3273–3278, 2015.

[35] C. Hu, Z. Chen, H. Xiao, Z. Zhen, X. Liu, and S. Bo, “Synthesis and characterization of a novel indoline based nonlinear optical chromophore with excellent electro-optic activity and high thermal stability by modifying the π-conjugated bridges,” *Journal of Materials Chemistry C*, 2017.

[36] J. Liu, G. Xu, F. Liu, I. Kityk, X. Liu, and Z. Zhen, “Recent advances in polymer electro-optic modulators,” *RSC Advances*, vol. 5, no. 21, pp. 15784–15794, 2015.

[37] R. Dinu, D. Jin, G. Yu, B. Chen, D. Huang, H. Chen, A. Barklund, E. Miller, C. Wei, and J. Vemagiri, “Environmental stress testing of electro–optic polymer modulators,” *Journal of Lightwave Technology*, vol. 27, no. 11, pp. 1527–1532, 2009.

[38] J. Wu, C. Peng, H. Xiao, S. Bo, L. Qiu, Z. Zhen, and X. Liu, “Donor modification of nonlinear optical chromophores: Synthesis, characterization, and fine-tuning of chromophores’ mobility and steric hindrance to achieve ultra large electro-optic

coefficients in guest–host electro-optic materials," *Dyes and Pigments*, vol. 104, pp. 15–23, 2014.

[39] J. D. Reis, A. Chiuchiarelli, S. Rossi, G. J. Suzigan, S. M. Ranzini, V. N. Rozental, E. S. Rosa, V. R. Cruz, L. H. Carvalho, J. C. Oliveira, *et al.*, "System validation of polymer-based transmitter optical sub-assembly for 100g/200g modules," in *Optical Fiber Communication Conference*, pp. Th1B–5, Optical Society of America, 2016.

[40] A. Chiuchiarelli, R. Gandhi, S. Rossi, S. Behtash, L. H. Carvalho, F. Caggioni, J. C. Oliveira, and J. Reis, "Single wavelength 100g real-time transmission for high-speed data center communications," in *Optical Fiber Communication Conference*, pp. W4I–2, Optical Society of America, 2017.

[41] G. Raybon, J. Cho, A. Adamiecki, P. Winzer, L. Carvalho, J. Oliveira, A. Konczykowska, J.-Y. Dupuy, and F. Jorge, "180-gb/s (90-gbd qpsk) single carrier transmitter using a thin film polymer on silicon i/q modulator," in *ECOC 2016; 42nd European Conference on Optical Communication; Proceedings of*, pp. 1–3, VDE, 2016.

[42] G. Yu, J. Mallari, H. Shen, E. Miller, C. Wei, V. Shofman, D. Jin, B. Chen, H. Chen, and R. Dinu, "40ghz zero chirp single-ended eo polymer modulators with low half-wave voltage," in *CLEO: Science and Innovations*, p. CTuN5, Optical Society of America, 2011.

[43] G. Yu, E. Miller, J. Mallari, C. Wei, B. Chen, H. Chen, V. Shofman, and R. Dinu, "Small form factor thin film polymer modulators for telecom applications," in *Optical Fiber Communication Conference and Exposition (OFC/NFOEC), 2012 and the National Fiber Optic Engineers Conference*, pp. 1–3, IEEE, 2012.

[44] OIF, "Implementation agreement for integrated polarization multiplexed quadrature modulated transmitters," *http://www.oiforum.com/wp-content/uploads*.

[45] A. E. W. Ivan P. Kaminow, Tingye Li, *Optical Fiber Telecommunications VI-A: Components and Subsystems*. Academic Press, 2013.

[46] Gigoptix, "100Gbps EO Polymer Modulator," website, Gigoptix, December 2010. http://www.gigoptix.com.

[47] R. Dar, M. Shtaif, and M. Feder, "New bounds on the capacity of the nonlinear fiber-optic channel," *Optics letters*, vol. 39, no. 2, pp. 398–401, 2014.

[48] K. P. Zhong, W. Chen, Q. Sui, J. Man, A. P. Lau, C. Lu, and L. Zeng, "Experimental demonstration of 500gbit/s short reach transmission employing pam4

signal and direct detection with 25gbps device," in *Optical Fiber Communication Conference*, pp. Th3A–3, Optical Society of America, 2015.

[49] E. Temprana, E. Myslivets, B.-P. Kuo, L. Liu, V. Ataie, N. Alic, and S. Radic, "Overcoming kerr-induced capacity limit in optical fiber transmission," *Science*, vol. 348, no. 6242, pp. 1445–1448, 2015.

[50] F. Poletti, N. Wheeler, M. Petrovich, N. Baddela, E. N. Fokoua, J. Hayes, D. Gray, Z. Li, R. Slavík, and D. Richardson, "Towards high-capacity fibre-optic communications at the speed of light in vacuum," *Nature Photonics*, vol. 7, no. 4, pp. 279–284, 2013.

[51] M. Azadeh, *Fiber Optics Engineering.* Optical Networks, Springer US, 2009.

[52] D. Sadot, G. Dorman, A. Gorshtein, E. Sonkin, and O. Vidal, "Single channel 112gbit/sec pam4 at 56gbaud with digital signal processing for data centers applications," *Optics express*, vol. 23, no. 2, pp. 991–997, 2015.

[53] Br photonics, "Br photonics to demonstrate a 100gbps Integrated TOSA reference platform for CFP2 Trasnceivers at OFC NFOEC," website, Gigoptix, January 2014. http://www.reuters.com/article/2014/03/06/brphotonics-idUSnBw065367a+100+BSW20140306.

[54] C. Soos, M. B. Marin, S. Détraz, L. Olanterä, C. Sigaud, S. Storey, J. Troska, F. Vasey, and P. Vichoudis, "The versatile transceiver: towards production readiness," *Journal of Instrumentation*, vol. 8, no. 03, p. C03004, 2013.

[55] F. Ulaby, E. Michielssen, and U. Ravaioli, *Fundamentals of Applied Electromagnetics, Global Edition.* Pearson Education Limited, 2015.

[56] R. Lasky and S. Johnson, "Low cost, mode-field matched, high performance laser transmitter optical subassembly," May 20 1997. US Patent 5,631,987.

[57] J. Eldring, B. Mynatt, K. Malone, and R. Adams, "Hermetically sealed transmitter optical subassembly," June 29 2004. US Patent 6,757,308.

[58] H. Zhang, S. Fu, J. Man, W. Chen, X. Song, and L. Zeng, "30km downstream transmission using 4× 25gb/s 4-pam modulation with commercial 10gbps tosa and rosa for 100gb/s-pon," in *Optical Fiber Communications Conference and Exhibition (OFC), 2014*, pp. 1–3, IEEE, 2014.

[59] T. Fujisawa, T. Itoh, S. Kanazawa, K. Takahata, Y. Ueda, R. Iga, H. Sanjo, T. Yamanaka, M. Kotoku, and H. Ishii, "Ultracompact, 160-gbit/s transmitter optical subassembly based on 40-gbit/s× 4 monolithically integrated light source," *Optics express*, vol. 21, no. 1, pp. 182–189, 2013.

[60] T. Ohyama, Y. Doi, W. Kobayashi, S. Kanazawa, T. Tanaka, K. Takahata, A. Kanda, T. Kurosaki, T. Ohno, H. Sanjoh, *et al.*, “Compact hybrid-integrated 100-gb/s tosa using eadfb laser array and awg multiplexer,” *IEEE Photonics Technology Letters*, vol. 28, no. 7, pp. 802–805, 2016.

[61] H.-S. Lee, J.-Y. Park, S.-M. Cha, S.-S. Lee, G.-S. Hwang, and Y.-S. Son, “Ribbon plastic optical fiber linked optical transmitter and receiver modules featuring a high alignment tolerance,” *Optics express*, vol. 19, no. 5, pp. 4301–4309, 2011.

[62] H. J. Unold, S. W. Mahmoud, R. Jager, M. Grabherr, R. Michalzik, and K. J. Ebeling, “Large-area single-mode vcsels and the self-aligned surface relief,” *IEEE Journal of Selected Topics in Quantum Electronics*, vol. 7, no. 2, pp. 386–392, 2001.

[63] K. Ishikawa, J. Zhang, A. Tuantranont, V. M. Bright, and Y.-C. Lee, “An integrated micro-optical system for vcsel-to-fiber active alignment,” *Sensors and Actuators A: Physical*, vol. 103, no. 1, pp. 109–115, 2003.

[64] L. Marigo-Lombart, J.-B. Doucet, A. Lecestre, B. Reig, B. Rousset, H. Thienpont, K. Panajotov, and G. Almuneau, “Self-aligned bcb planarization method for high-frequency signal injection in a vcsel with an integrated modulator,” in *SPIE Photonics Europe*, pp. 98921R–98921R, International Society for Optics and Photonics, 2016.

[65] Y. Zhao, Y. Sun, Y. He, S. Yu, Y. Song, and J. Dong, “Surface and edge electroluminescence study of as-grown vcsel structures,” *Applied Surface Science*, 2016.

[66] D. Brunner and I. Fischer, “Reconfigurable semiconductor laser networks based on diffractive coupling,” *Optics letters*, vol. 40, no. 16, pp. 3854–3857, 2015.

[67] M. Karppinen, N. Salminen, T. Korhonen, T. Alajoki, J. Petäjä, E. Bosman, G. Van Steenberge, J. Justice, U. Khan, B. Corbett, *et al.*, “Optical coupling structure made by imprinting between single-mode polymer waveguide and embedded vcsel,” in *SPIE OPTO*, pp. 93680H–93680H, International Society for Optics and Photonics, 2015.

[68] G. Roelkens, L. Liu, D. Liang, R. Jones, A. Fang, B. Koch, and J. Bowers, “Iii-v/silicon photonics for on-chip and intra-chip optical interconnects,” *Laser & Photonics Reviews*, vol. 4, no. 6, pp. 751–779, 2010.

[69] S. Tanaka, S.-H. Jeong, S. Sekiguchi, T. Kurahashi, Y. Tanaka, and K. Morito, “High-output-power, single-wavelength silicon hybrid laser using precise flip-chip bonding technology,” *Optics express*, vol. 20, no. 27, pp. 28057–28069, 2012.

[70] M. R. Billah, T. Hoose, T. Onanuga, N. Lindenmann, P. Dietrich, T. Wingert, M. L. Goedecke, A. Hofmann, U. Troppenz, A. Sigmund, *et al.*, “Multi-chip integration of lasers and silicon photonics by photonic wire bonding,” in *CLEO: Science and Innovations*, pp. STu2F–2, Optical Society of America, 2015.

[71] D. Dai, J. Bauters, and J. E. Bowers, “Passive technologies for future large-scale photonic integrated circuits on silicon: polarization handling, light non-reciprocity and loss reduction,” *Light: Science & Applications*, vol. 1, no. 3, p. e1, 2012.

[72] D. Vermeulen, P. Verheyen, P. Absil, W. Bogaerts, D. Van Thourhout, G. Roelkens, *et al.*, “Silicon-on-insulator polarization rotator based on a symmetry breaking silicon overlay,” *IEEE Photonics Technology Letters*, vol. 24, no. 6, pp. 482–484, 2012.

[73] D. Dai and J. E. Bowers, “Novel concept for ultracompact polarization splitter-rotator based on silicon nanowires,” *Optics express*, vol. 19, no. 11, pp. 10940–10949, 2011.

[74] F. Balestra, “Silicon-on-insulator devices,” *Wiley Encyclopedia of Electrical and Electronics Engineering*, 2014.

[75] C. Kazmierski, A. Konczykowska, F. Jorge, F. Balache, M. Riet, C. Janet, and A. Scavennec, “100 Gb/s operation of an AlGaInAs semi-insulating buried heterojunction EML,” in *Proc of Opt. Fiber Commun. Conf. (OFC)*, 2009.

[76] T. Kawanishi, T. Sakamoto, and M. Izutsu, “High-speed control of lightwave amplitude and phase and frequency by use of electrooptic effect,” *IEEE J. Select. Topics in Quantum Electron.*, vol. 13, pp. 79–97, 2007.

[77] K. Ho, *Phase-Modulated Optical Communication Systems*. Springer US, 2005.

[78] J. Fage-Pedersen, L. H. Frandsen, A. V. Lavrinenko, and P. I. Borel, “A linear electrooptic efrfect in Silicon, induced by use of strain,” in *Proc. WC 3*, 2009.

[79] I. Kaminow, *An Introduction to Electrooptic Devices: Selected Reprints and Introductory Text By*. Elsevier Science, 2013.

[80] P. J. Winzer, G. Raybon, C. Doerr, M. Duelk, and C. Dorrer, “107 gb/s optical signal generation using electronic time-division multiplexing,” *J. Lightwave Technology*, vol. 24, pp. 3107–3113, 2006.

[81] K. Tsuzuki, T. Ishibashi, T. Ito, N. Kikuchi, and F. Kano, “80gb/s inp mach-zehnder modulator module using liquid crystal polymer (lcp) transmission line,” in *Proc. European Conf. in Opt. Commun. (ECOC)*, 2009.

[82] G. T. Reed, G. Z. Mashanovich, F. Y. Gardes, M. Nedeljkovic, Y. Hu, D. J. Thomson, K. Li, P. R. Wilson, S.-W. Chen, and S. S. Hsu, "Recent breakthroughs in carrier depletion based silicon optical modulators," *Nanophotonics*, vol. 3, no. 4-5, pp. 229–245, 2014.

[83] D. J. Thomson, F. Y. Gardes, S. Liu, H. Porte, L. Zimmermann, J.-M. Fedeli, Y. Hu, M. Nedeljkovic, X. Yang, P. Petropoulos, *et al.*, "High performance mach–zehnder-based silicon optical modulators," *IEEE Journal of Selected Topics in Quantum Electronics*, vol. 19, no. 6, pp. 85–94, 2013.

[84] X. Tu, T.-Y. Liow, J. Song, X. Luo, Q. Fang, M. Yu, and G.-Q. Lo, "50-gb/s silicon optical modulator with traveling-wave electrodes," *Optics express*, vol. 21, no. 10, pp. 12776–12782, 2013.

[85] J. T. Kim, "Silicon optical modulators based on tunable plasmonic directional couplers," *IEEE Journal of Selected Topics in Quantum Electronics*, vol. 21, no. 4, pp. 184–191, 2015.

[86] J.-S. Kim and J. T. Kim, "Silicon electro-optic modulator based on an ito-integrated tunable directional coupler," *Journal of Physics D: Applied Physics*, vol. 49, no. 7, p. 075101, 2016.

[87] J. Witzens, T. Baehr-Jones, and M. Hochberg, "Design of transmission line driven slot waveguide mach-zehnder interferometers and application to analog optical links," *Optics express*, vol. 18, no. 16, pp. 16902–16928, 2010.

[88] L. Dalton, A. Harper, A. Ren, F. Wang, G. Todorova, J. Chen, C. Zhang, and M. Lee, "Polymeric electro-optic modulators: From chromophore design to integration with semiconductor very large scale integration electronics and silica fiber optics," *Industrial & engineering chemistry research*, vol. 38, no. 1, pp. 8–33, 1999.

[89] T.-D. Kim, J. Luo, J.-W. Ka, S. Hau, Y. Tian, Z. Shi, N. M. Tucker, S.-H. Jang, J.-W. Kang, and A.-Y. Jen, "Ultralarge and thermally stable electro-optic activities from diels–alder crosslinkable polymers containing binary chromophore systems," *Advanced Materials*, vol. 18, no. 22, pp. 3038–3042, 2006.

[90] A. Chen and E. Murphy, *Broadband optical modulators: science, technology, and applications.* CRC press, 2011.

[91] J. Mallari, C. Wei, D. Jin, G. Yu, A. Barklund, E. Miller, P. O'Mathuna, R. Dinu, A. Motafakker-Fard, and B. Jalali, "100gbps eo polymer modulator product and its characterization using a real-time digitizer," in *Optical Fiber Communication Conference*, p. OThU2, Optical Society of America, 2010.

[92] G. Yu, M. E., M. J., C. Wei, B. Chen, H. Chen, S. V., and D. R., "Small form factor thin film polymer modulators for telecom applications," in *Optical Fiber Communication Conference and Exposition (OFC/NFOEC), 2012 and the National Fiber Optic Engineers Conference*, pp. 1–3, March 2012.

[93] A. Willner and S. R. Nuccio, "Electro-optic polymer modulators," in *Optical Fiber Communication Conference*, p. OW4F.1, Optical Society of America, 2012.

[94] H. Huang, J.-Y. Yang, Y. Yue, Y. Ren, S. R. Nuccio, R. Dinu, D. Parekh, C. J. Chang-Hasnain, and A. Willner, "100-gbit/s amplitude and phase modulation characterization of a single-drive, low-vπ polymer mach-zehnder modulator," in *Optical Fiber Communication Conference*, p. OW4F.5, Optical Society of America, 2012.

[95] S.-K. Kim, H. Zhang, D. Chang, C. Zhang, C. Wang, W. Steier, and H. Fetterman, "Electrooptic polymer modulators with an inverted-rib waveguide structure," *IEEE Photonics Technology Letters*, vol. 15, no. 2, pp. 218–220, 2003.

[96] Y. Kuo and U. of Southern California, *Optical Trimming of Electro-optical Polymer Devices Using Photo-bleaching*. University of Southern California, 2006.

[97] R. Dinu, E. Miller, G. Yu, B. Chen, A. Scarpaci, H. Chen, and C. Pilgrim, *Optical Fiber Telecommunications VIA: Chapter 5. High-Speed Polymer Optical Modulators*. Optics and Photonics, Elsevier Science, 2013.

[98] C. Harper and E. Petrie, *Plastics Materials and Processes: A Concise Encyclopedia*. Wiley, 2003.

[99] F. Liu, H. Xiao, H. Xu, S. Bo, C. Hu, Y. He, J. Liu, Z. Zhen, X. Liu, and L. Qiu, "Synthesis of chromophores with ultrahigh electro-optic activity: Rational combination of the bridge, donor and acceptor groups," *Dyes and Pigments*, vol. 136, pp. 182–190, 2017.

[100] C. Multiphysics, "5.2, 2015," *COMSOL Multiphysics: a finite element analysis, solver and simulation software for various physics and engineering application, especially coupled phenomena, or multiphysics. URL http://www. comsol. com.*

[101] D. M. Pozar, *Microwave engineering*. John Wiley & Sons, 2009.

[102] J. Toney, *Lithium Niobate Photonics:*. Artech House Publishers, 2015.

[103] R. Yaakop and F. K. Elektrik, *Thermo Optic - Effect on Polymer Waveguide*. Universiti Teknologi Malaysia, 2008.

[104] H. Dai, J. An, L. Wang, Y. Wang, L. Zhang, J. Zhang, H. Wang, P. Pan, X. Zhang, R. Liu, *et al.*, "Design of thermo-optic variable optical attenuator based on quartz substrate," *Optics and Photonics Journal*, vol. 3, no. 02, p. 158, 2013.

[105] "Standard dimensions and tolerances."

[106] M. Studio, "Cst-computer simulation technology," *Bad Nuheimer Str*, vol. 19, p. 64289, 2008.

[107] T. Ohyama, A. Ohki, K. Takahata, T. Ito, N. Nunoya, H. Mawatari, T. Fujisawa, S. Kanazawa, R. Iga, and H. Sanjoh, "Transmitter optical subassembly using a polarization beam combiner for 100 gbit/s ethernet over 40-km transmission," *Journal of Lightwave Technology*, vol. 10, no. 33, pp. 1985–1992, 2015.

[108] I. Std, "P802.3bs 200gb/s and 400gb/s ethernet task force url, 16th may 2016," *IEEE P802.3bs 200Gb/s and 400Gb/s Ethernet Task Force URL http://www.ieee802.org/3/bs/*.

[109] N. Eiselt, J. Wei, H. Griesser, A. Dochhan, M. H. Eiselt, J.-P. Elbers, J. J. V. Olmos, and I. T. Monroy, "Evaluation of real-time 8× 56.25 gb/s (400g) pam-4 for inter-data center application over 80 km of ssmf at 1550 nm," *Journal of Lightwave Technology*, vol. 35, no. 4, pp. 955–962, 2017.

[110] I. Lyubomirsky and W. Ling, "Advanced modulation for datacenter interconnect," in *Optical Fiber Communication Conference*, pp. W4J–3, Optical Society of America, 2016.

[111] ATP, "Applied thin-film products catalog and specifications," *http://www.thinfilm.com/*.

[112] K. Z. Rajab, M. Naftaly, E. H. Linfield, J. C. Nino, D. Arenas, D. Tanner, R. Mittra, and M. Lanagan, "Broadband dielectric characterization of aluminum oxide (al2o3)," *Journal of Microelectronics and Electronic Packaging*, vol. 5, no. 1, pp. 2–7, 2008.

[113] R. Goulding, "Loss tangent measurements on unirradiated alumina-sj zinkle and,"

[114] Kyocera, "Ceramic packages," *http://global.kyocera.com/prdct/semicon/material/index.html*.

[115] E. Hammerstad and F. Bekkadal, *Microstrip Handbook.* ELAB report, Norwegian Institute of Technology, 1975.

[116] X. C.-B. A. T. L. Braunisch, Henning; Gu, "[ieee 2007 proceedings 57th electronic components and technology conference - sparks, nv, usa (2007.05.29-2007.06.1)] 2007 proceedings 57th electronic components and technology conference - off-chip

rough-metal-surface propagation loss modeling and correlation with measurements," 2007.

[117] I. R. Christie and B. P. Cameron, "Gold electrodeposition within the electronics industry," *Gold Bulletin*, vol. 27, no. 1, pp. 12–20, 1994.

[118] O. Rezvanian, M. Zikry, C. Brown, and J. Krim, "Surface roughness, asperity contact and gold rf mems switch behavior," *Journal of Micromechanics and Microengineering*, vol. 17, no. 10, p. 2006, 2007.

[119] L. Melo, A. Vaz, M. Salvadori, and M. Cattani, "Grain sizes and surface roughness in platinum and gold thin films," in *Journal of Metastable and Nanocrystalline Materials*, vol. 20, pp. 623–628, Trans Tech Publ, 2004.

[120] G. Baumann, H. Richter, A. Baumgartner, D. Ferling, R. Heilig, D. Hollmann, H. Muller, H. Nechansky, and M. Schlechtweg, "51 ghz frontend with flip chip and wire bond interconnections from gaas mmics to a planar patch antenna," in *Microwave Symposium Digest, 1995., IEEE MTT-S International*, pp. 1639–1642, IEEE, 1995.

[121] T. Krems, W. Haydl, H. Massler, and J. Rudiger, "Millimeter-wave performance of chip interconnections using wire bonding and flip chip," in *Microwave Symposium Digest, 1996., IEEE MTT-S International*, vol. 1, pp. 247–250, IEEE, 1996.

[122] C. Atalan and T. Eker, "Performance evaluation of gold wire and ribbon interconnects in high frequency circuits," in *International Symposium on Microelectronics*, vol. 2016, pp. 000450–000455, International Microelectronics Assembly and Packaging Society, 2016.

[123] D. J. Beck, K. V. Hillman, H. Deju, G. A. Rief, T. K. Buschor, J. B. Nichols, B. A. Pigon, W. M. Whybrew, and S. E. Wilson, "High frequency, low temperature thermosonic ribbon bonding process for system-level applications," Apr. 20 1999. US Patent 5,894,983.

[124] C. B. Luechinger, "Ribbon bonding in an electronic package," June 29 2010. US Patent 7,745,253.

[125] J. Lim, D. Kwon, J.-S. Rieh, S.-W. Kim, and S. Hwang, "Rf characterization and modeling of various wire bond transitions," *IEEE Transactions on Advanced Packaging*, vol. 28, no. 4, pp. 772–778, 2005.

[126] Anritsu, "Components," *https://www.anritsu.com/en-US/components-accessories/products*.

[127] D. E. Kumar, G. Giaretta, S. Schiaffino, and D. A. Ice, “Flexible circuit for establishing electrical connectivity with optical subassembly,” Oct. 21 2008. US Patent 7,439,449.

[128] T. Uesugi, N. Okada, T. Saito, T. Yamatoya, Y. Morita, and A. Sugitatsu, “1.3 μm eml tosa for serial 40 gbps ethernet solution,” in *Optical Fiber Communication Conference*, p. OThC2, Optical Society of America, 2010.

[129] J.-J. Jou, T.-T. Shih, C.-Y. Wu, and Z.-X. Su, “Low-cost to-can package combined with flexible and hard printed circuit boards for 25-gb/s optical subassembly modules,” *Optical Engineering*, vol. 56, no. 2, pp. 026108–026108, 2017.

[130] M. C. Hargis, D. P. Gaio, R. T. Lindquist, W. K. Hogan, J. Walling, S. Nangalia, P. Deane, M. F. Swain, and C. M. Gabel, “Compact optical sub-assembly with integrated flexible circuit,” Jan. 9 2007. US Patent 7,160,039.

[131] H. Sone, “Optical transceiver using optical sub-assembly having multiple lead pins connected to the substrate by a flexible printed circuit,” Sept. 11 2007. US Patent 7,267,553.

[132] L. Chen, C. R. Doerr, and Y.-K. Chen, “Compact polarization rotator on silicon for polarization-diversified circuits,” *Optics letters*, vol. 36, no. 4, pp. 469–471, 2011.

[133] Y. Ma, Y. Zhang, S. Yang, A. Novack, R. Ding, A. E.-J. Lim, G.-Q. Lo, T. Baehr-Jones, and M. Hochberg, “Ultralow loss single layer submicron silicon waveguide crossing for soi optical interconnect,” *Optics express*, vol. 21, no. 24, pp. 29374–29382, 2013.

[134] P. Sanchis, P. Villalba, F. Cuesta, A. Håkansson, A. Griol, J. V. Galán, A. Brimont, and J. Martí, “Highly efficient crossing structure for silicon-on-insulator waveguides,” *Optics letters*, vol. 34, no. 18, pp. 2760–2762, 2009.

[135] T. Murao, N. Yasui, K. Mochizuki, M. Shimono, H. Kodera, D. Morita, T. Yamatoya, and H. Aruga, “Lens alignment technique using high-power laser for hybrid integrated multi-channel transmitter optical sub-assemblies,” *IEEE Photonics Technology Letters*, vol. 25, no. 20, pp. 1958–1960, 2013.

[136] K. Adachi, A. Nakanishi, T. Suzuki, H. Irie, H. Sasaki, T. Aoki, M. Shishikura, K. Naoe, and S. Tanaka, “A passive optical alignment technique for single-mode fibers and light-source arrays,” in *Optical Fiber Communication Conference*, pp. W2A–5, Optical Society of America, 2017.

[137] D. K. T. Ng, Q. Wang, J. Pu, K. P. Lim, Y. Wei, Y. Wang, Y. Lai, and S. T. Ho, "Demonstration of heterogeneous iii–v/si integration with a compact optical vertical interconnect access," *Optics letters*, vol. 38, no. 24, pp. 5353–5356, 2013.

[138] D. Liang and J. E. Bowers, "Recent progress in lasers on silicon," *Nature photonics*, vol. 4, no. 8, pp. 511–517, 2010.

[139] Y. Ding, C. Peucheret, H. Ou, and K. Yvind, "Fully etched apodized grating coupler on the soi platform with- 0.58 db coupling efficiency," *Optics letters*, vol. 39, no. 18, pp. 5348–5350, 2014.

[140] H.-L. Tseng, E. Chen, H. Rong, and N. Na, "High-performance silicon-on-insulator grating coupler with completely vertical emission," *Optics Express*, vol. 23, no. 19, pp. 24433–24439, 2015.

[141] L. Liu, J. Zhang, C. Zhang, S. Wang, C. Jin, Y. Chen, K. Chen, T. Xiang, and Y. Shi, "Silicon waveguide grating coupler for perfectly vertical fiber based on a tilted membrane structure," *Optics letters*, vol. 41, no. 4, pp. 820–823, 2016.

[142] J. Cardenas, C. B. Poitras, K. Luke, L.-W. Luo, P. A. Morton, and M. Lipson, "High coupling efficiency etched facet tapers in silicon waveguides," *IEEE Photon. Technol. Lett.*, vol. 26, no. 23, pp. 2380–2382, 2014.

[143] M. Pu, L. Liu, H. Ou, K. Yvind, and J. M. Hvam, "Ultra-low-loss inverted taper coupler for silicon-on-insulator ridge waveguide," *Optics Communications*, vol. 283, no. 19, pp. 3678–3682, 2010.

[144] H. Huang, S. Nuccio, Y. Yue, J.-Y. Yang, Y. Ren, C. Wei, G. Yu, R. Dinu, D. Parekh, C. Chang-Hasnain, *et al.*, "Broadband modulation performance of 100-ghz eo polymer mzms," *Journal of Lightwave Technology*, vol. 30, no. 23, pp. 3647–3652, 2012.

[145] D. Chen, H. R. Fetterman, A. Chen, W. H. Steier, L. R. Dalton, W. Wang, and Y. Shi, "Demonstration of 110 ghz electro-optic polymer modulators," *Applied Physics Letters*, vol. 70, no. 25, pp. 3335–3337, 1997.

[146] L. M. Machado, G. Delrosso, F. Borin, J. R. F. de Oliveira, V. Corso, L. H. H. de Carvalho, and J. C. R. F. de Oliveira, "Advanced optical communication systems and devices," in *Electronics System-Integration Technology Conference (ESTC), 2014*, pp. 1–4, IEEE, 2014.

[147] V. Katopodis, Z. Zhang, P. Groumas, A. Konczykowska, J.-Y. Dupuy, A. Beretta, A. Dede, E. Miller, J. H. Choi, P. Harati, *et al.*, "Tunable transmitter for serial 100 gb/s connectivity inside flexible data centers using hybrid polymer integration," in

Optical Fiber Communication Conference, pp. Tu2A–3, Optical Society of America, 2015.

[148] Z. Zhang, N. Mettbach, C. Zawadzki, J. Wang, D. Schmidt, W. Brinker, N. Grote, M. Schell, and N. Keil, "Polymer-based photonic toolbox: passive components, hybrid integration and polarisation control," *IET optoelectronics*, vol. 5, no. 5, pp. 226–232, 2011.

[149] L. Liu, Y. Ding, K. Yvind, and J. M. Hvam, "Silicon-on-insulator polarization splitting and rotating device for polarization diversity circuits," *Optics express*, vol. 19, no. 13, pp. 12646–12651, 2011.

[150] J. Shu, C. Qiu, X. Zhang, and Q. Xu, "Efficient coupler between chip-level and board-level optical waveguides," *Optics letters*, vol. 36, no. 18, pp. 3614–3616, 2011.

[151] T. Mitze, M. Schnarrenberger, L. Zimmermann, J. Bruns, F. Fidorra, J. Kreissl, K. Janiak, S. Fidorra, H. Heidrich, and K. Petermann, "Hybrid integration of iii/v lasers on a silicon-on-insulator (soi) optical board," in *IEEE International Conference on Group IV Photonics, 2005. 2nd*, pp. 210–212, IEEE, 2005.

[152] B. Mersali, H. Bruckner, M. Feuillade, S. Sainson, A. Ougazzaden, and A. Carenco, "Theoretical and experimental studies of a spot-size transformer with integrated waveguide for polarization insensitive optical amplifiers," *Journal of lightwave technology*, vol. 13, no. 9, pp. 1865–1872, 1995.

[153] A. Yariv, "Coupled-mode theory for guided-wave optics," *IEEE Journal of Quantum Electronics*, vol. 9, no. 9, pp. 919–933, 1973.

[154] C. Rubio-Mercedes, V. Rodríguez-Esquerre, I. T. Lima Jr, and H. E. Hernandez-Figueroa, "Analysis of straight periodic segmented waveguide using the 2-d finite element method," *Journal of Lightwave Technology*, vol. 32, no. 11, pp. 2163–2169, 2014.

[155] Lumerical, "Mode solutions," 2016.

[156] C. Balanis, *Advanced Engineering Electromagnetics, 2nd Edition.* Wiley, 2012.

Appendix 1

Coupling Mode Theory

Consider two waveguides with different propagation constants ($k_{zA,B}$), permittivities $\varepsilon_{2,3}$ enclosed in an ε_1 material (as shown in Fig. 6.1).

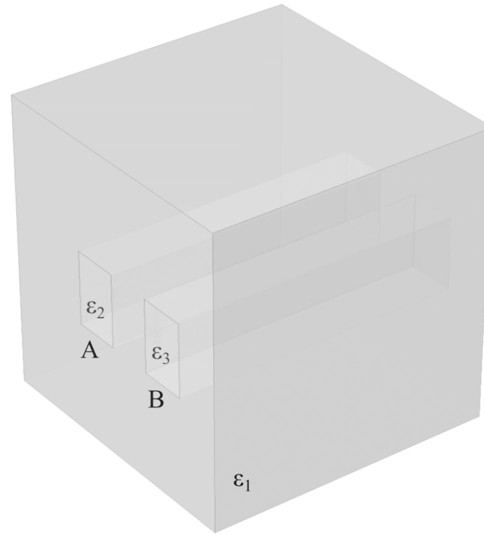

Figure 6.1: Geometry of a simple directional coupler.

The set of equations for directional coupling are [156]:

$$\begin{aligned}\frac{da_A}{dz} &= -jC_{BA}e^{j\Delta k_z}a_B(z)\\ \frac{da_B}{dz} &= -jC_{AB}e^{j\Delta k_z}a_A(z)\end{aligned} \tag{6.1}$$

where

$$\Delta k = k_{zA} - k_{zB};$$

and

$$C_{AB} = \frac{\omega}{2} \int\int_{s_A} (\varepsilon_2 - \varepsilon_1) \left(\overrightarrow{E}_A \cdot \overrightarrow{E}_B^*\right) ds$$
$$C_{BA} = \frac{\omega}{2} \int\int_{s_B} (\varepsilon_3 - \varepsilon_1) \left(\overrightarrow{E}_B \cdot \overrightarrow{E}_A^*\right) ds$$

are the coupling coefficients, defined as the integrations over the region of waveguides A and B, respectively. The two solutions for this set of equations start by assuming that $a_{A,B}$ have wave behavior of the form $a_{A,B}^0 e^{-j\gamma_{A,B} z}$, where $\gamma_{A,B}$ are the new unknown and $a_{A,B}^0$ is constant. When going back to (6.1), we find that the algebraic equation system:

$$\begin{aligned} a_A^0 &= \frac{C_{BA}}{\gamma_A} e^{j(\Delta k + \gamma_A - \gamma_B) z} a_B^0 \\ a_B^0 &= \frac{C_{AB}}{\gamma_B} e^{j(\Delta k + \gamma_B - \gamma_A) z} a_A^0 \end{aligned} \tag{6.2}$$

For (6.2) to be true for all z, $\gamma_B = \Delta k + \gamma_A$, thus

$$\gamma_A = -\frac{\Delta k}{2} \pm \sqrt{\left(\frac{\Delta k}{2}\right)^2 + C_{AB} C_{BA}}$$

$$\gamma_B = \frac{\Delta k}{2} \pm \sqrt{\left(\frac{\Delta k}{2}\right)^2 + C_{AB} C_{BA}}$$

Defining $S = \sqrt{\left(\frac{\Delta k}{2}\right)^2 + C_{AB} C_{BA}}$ we can write the solution for equation system (6.1) as:

$$a_A(z) = e^{j(\Delta k/2) z} \left(A_1 e^{jSz} + A_2 e^{-jSz}\right) \tag{6.3}$$

where we can determine the constants A_1 and A_2 by imposing boundary conditions along z. If we excite waveguide B mode and intend to transfer that power to waveguide A; at $z = 0$, all the system's energy is in mode B, from eq. 6.3 we got $A_2 = -A_1$ and we can simplify $a_A(z) = 2jA_1 e^{j(\Delta k/2) z} sin(Sz)$. To obtain $a_B(z)$ let us replace $a_A(z)$ value into equation 6.1.

$$a_B(z) = \frac{2jA_1}{C_{BA}} e^{-j(\Delta k/2) z} \left[-\frac{\Delta k}{2} \sin(Sz) + jScos(Sz)\right]$$

In terms of power, let us define P_0 as the input power in waveguide B at $z = 0$, then the power in each waveguide is a sinusoidal function of z as shown in (6.4).

$$\begin{aligned} P_A(z) &= |a_A(z)|^2 = P_0 \frac{|C_{BA}|^2}{S^2} \sin^2(Sz) \\ P_B(z) &= |a_B(z)|^2 = P_0 \left[\left(\frac{\Delta k}{2S}\right)^2 \sin^2(Sz) + \cos^2(Sz)\right] \end{aligned} \tag{6.4}$$

When A and B waveguides are identical, as seen in Figure 6.1, they fall into the phase matched condition ($\Delta k = 0$), and we can simplify the solution by making $C_{AB} = C_{BA} = C$ and thus the power in the two waveguides interchanges according to (6.5). When there is P_0 in one waveguide, there is 0 power in the other at a π phase distance called $L_{coup} = \frac{\pi}{2C}$.

$$\begin{aligned} P_A(z) &= P_0 \sin^2(C_z) \\ P_B(z) &= P_0 \cos^2(C_z) \end{aligned} \tag{6.5}$$

When both waveguides are different ($\Delta k \neq 0$) the maximum power transferred to the other guide happens when $S_z = \pi/2$ and is not P_0 as it was with the phase matched condition. It is actually inversely proportional to Δk:

$$\max\left(\frac{P_A}{P_0}\right) = \frac{|C_{BA}|^2}{C_{AB}C_{BA} + \Delta k^2/4} \tag{6.6}$$

Assuming that A and B waveguides from Figure 6.1 are identical, but considering now an infinite perfect electric conductor plane (YZ) at a distance d_C from waveguide A, when d_C is small enough to interfere with the evanescent field region of waveguide A, we no longer hold $\Delta k = 0$, but if we consider (6.6), we can conclude that good power transfer will require

$$|\Delta k| < 2\sqrt{C_{AB}C_{BA}}.$$

If A and B are further apart, $C_{AB,BA}$ will be small and thus coupling will be achieved if we strongly approach the phase matched condition, but if the waveguides are close together, it gives us a wider range for k_{Az} and k_{zB}.